Summer 2011

Characterization of shielding effectiveness for metallic enclosures

Nicholas Bennett Mentesana

Department:

CHARACTERIZATION OF SHIELDING EFFECTIVENESS FOR METALLIC ENCLOSURES

by

NICHOLAS BENNETT MENTESANA

A THESIS

Presented to the Faculty of the Graduate School of the

MISSOURI UNIVERSITY OF SCIENCE AND TECHNOLOGY

In Partial Fulfillment of the Requirements for the Degree

MASTER OF SCIENCE IN ELECTRICAL ENGINEERING

2011

Approved by

David Pommerenke, Advisor
James L. Drewniak
Jun Fan

ABSTRACT

This topic discusses and verifies an equation for estimating the shielding effectiveness of metallic enclosures through the use of numerical simulations. Using ideas from Bethe's "Theory of Diffraction by Small Holes" [5], a previous student from the Missouri S&T Electromagnetic Compatibility Laboratory developed an equation that would yield an envelope prediction for the worst-case EMI from an aperture array backed by an over-moded cavity. In [1-4], Min Li (PhDEE '99) used results from measurements, simulations, and physics-based equations to formulate a simple equation that would predict these EMI levels. The main purpose of this thesis is to revisit this work and determine when and why this prediction fails, if at all. Broadband FDTD simulations are used to first evaluate several simple models of aperture arrays in an infinite PEC sheet. With a sound understanding of this scenario, the simulations are then extended to the more realistic PEC enclosures. In the end, the shielding effectiveness of aperture arrays excited by both uniform plane waves at normal incidence and over-moded cavities can be predicted to within 3dB, so long as the dimensions of the apertures remain less than $\lambda/6$.

ACKNOWLEDGMENTS

I would like to express my gratitude to Dr. David Pommerenke, my graduate advisor, for his help and teachings throughout the course of my M.S. degree. I would like to thank Dr. James L. Drewniak for his guidance and motivation while conducting the work necessary to write this thesis. I would also like to thank Dr. Jun Fan, Dr. Richard DuBroff, and every other faculty and staff member of the Electromagnetic Compatibility Laboratory for their help during the pursuit of my M.S. degree.

I would to thank Dr. Bruce Archambeault and Samuel Connor of IBM for providing this research topic, funding, and insight throughout my research. I would also like to thank Dr. Genda Chen for providing me with support for working on the Smart Rock. I would also like to extend a large thank you to the Office of Graduate Studies for awarding me the Chancellor's Fellowship, making life while being a full-time student much more bearable and manageable through their generous financial aid.

Most of all, I would like thank my parents, Salvatore and Debra, and my brother, Anthony, for their love and support while completing my M.S. degree. Ultimately, I would like to dedicate this thesis to Dr. Leroy Alt and Professor Bob Wilson. Both instructors were very interesting, very knowledgeable men who helped peak my interest in Electrical Engineering. Sadly, neither of these gentlemen are around today for me to thank personally, but this thesis shall be my way of showing my gratitude to their pursuit of education.

TABLE OF CONTENTS

Page

LIST OF ILLUSTRATIONS

LIST OF TABLES

1 INTRODUCTION

System level shielding design is not a trivial science. To precisely predict how well a metallic enclosure will prevent the emission of electromagnetic waves would require a combination of antenna theory, over-moded cavity analysis, and knowledge of the noise sources within the enclosure. For most practical system designs, a closed-form equation predicting the fields radiated by every opening in the enclosure does not exist. As for the internal modes of the enclosure, the field structures can be easily determined for the case of an empty cavity, but once one or more additional conductors are introduced, such as PCB ground planes, along with lossy dielectric materials, it becomes very difficult to predict exactly what the fields will look like inside the enclosure, making it even more challenging to precisely determine the excitation of each aperture in the enclosure. Noise sources within the system can be potentially identified through tests and measurements, but also need to be identified and properly modelled in order to predict which modes will become excited within the enclosure. With so much complexity, it seems that it would be very beneficial to the EMC engineer to be able to use basic system parameters in a simple equation in order to accurately predict the shielding effectiveness of an enclosure during preliminary design stages.

To meet this challenge, Min Li (PhDEE ’99 UMR) developed an estimation of the worst-case far electric field intensity that is based upon parameters unique to the system at hand. Li’s early work [1-2] was focused on finding simple relationships between the data gathered through simulations and measurements in order to determine a correlation between field strength and system attributes, such as aperture size, the number of

apertures, etc. Li's later publications [3-4] then took the simple relationships and combined them with integral equation formulations and Bethe's Small Hole Theory [5] in order to develop a stand-alone estimation that did not have to be normalized to any measured data. In [4], this stand-alone estimation for the worst-case EMI from an aperture array backed by an over-moded cavity was found to be

$$\left|E_{far}\right| = N\frac{\left(3.9\times10^{-15}\right)L^3 f^{3/2}}{\ln\left(1+0.66\alpha\right)R}\sqrt{\frac{P_o Q}{n_g \mu V\left(\frac{k_x^2}{k_y^2}+1\right)}} \tag{1.1}$$

where N is the number of apertures, L is the length of the apertures, f is the frequency, α is the ratio of the aperture width to height, Q is the Q-factor of the enclosure, V is the volume of the enclosure, P_o is the power delivered to the enclosure from the source, R is the distance from the center of the aperture array to the observation point, n_g is a coefficient equal to $\frac{1}{2}$, and k_x and k_y are the wave numbers in the x- and y-directions. The full derivation of (1.1) shall be shown in Section 2, which will provide insight to the physical meaning of each term. An example of the application of this estimation can be seen in Figure 1.1.

To take the estimation in (1.1) one step further, Min Li also showed that for a well-known dipole source within the enclosure, where P_o is the radiated power from the dipole, (1.1) can be used to predict the shielding effectiveness (SE) of the enclosure. By defining SE as the ratio of the field intensity from the source with no shielding enclosure to the field intensity from the source/shielding enclosure system at the same observation point, a worst-case SE approximation is found to be

$$SE = 1.2 \times 10^{12} \frac{\sqrt{\frac{V}{Q}} \ln(1 + 0.66\alpha)}{NL^3 f^{3/2}} \tag{1.2}$$

Within this paper, the derivation of both (1.1) and (1.2) will be revisited and tested with numerical simulations.

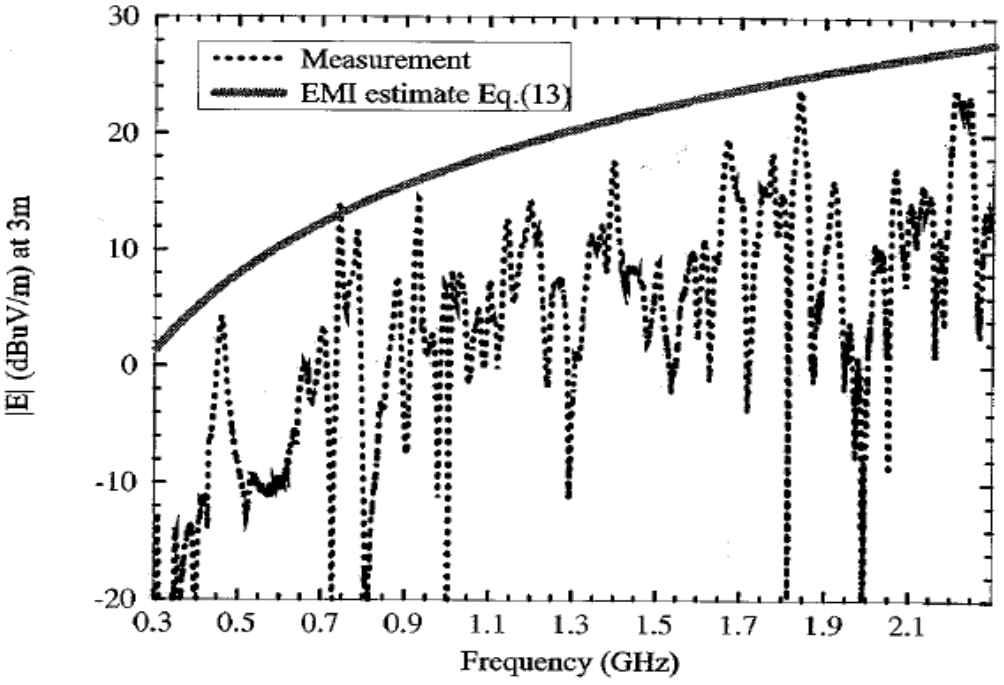

Figure 1.1. Comparison of measured data and Min Li's estimation for a test enclosure [4].

2 BETHE'S THEORY AND MODELING

The foundation for (1.1) and (1.2) is in Bethe's "Theory of Diffraction by Small Holes" [5]. In [5], Bethe was able to show that the fields that couple through a single electrically small aperture and radiate are predominately due to the normal E- and tangential H-fields at the aperture. To simplify the problem, the aperture can be replaced with PEC, and equivalent electric and magnetic polarization currents are introduced on both sides of the former aperture to approximate the perturbed fields. Cohn [6] and McDonald [7] expanded Bethe's theoretical work and conducted experiments and mathematical modeling to broaden the practical applicability of Bethe's work. This section borrows concepts from all three of these sources to derive the radiated fields from the apertures.

2.1 POLARIZATION AND MAXWELL'S EQUATIONS

Ampere's Law states that in free-space, an electric current and/or a time-varying electric flux density will induce a curling magnetic field, as shown in (2.1a). Faraday's Law states a similar behavior for a curling electric field induced by a time-varying magnetic flux density or magnetic current in (2.1b), both shown below.

$$\nabla \times \overline{H} = j\omega \overline{D} + \overline{J} = j\omega \varepsilon_o \overline{E} + \overline{J} \tag{2.1a}$$

$$\nabla \times \overline{E} = -j\omega \overline{B} - \overline{M} = -j\omega \mu_o \overline{H} - \overline{M} \tag{2.1b}$$

When in the presence of matter, (2.1) must be altered to account for the polarization of the material. The net electric and magnetic flux densities become a combination of the fields in free-space and the fields from the molecular polarizations of matter, shown in (2.2) and (2.3), where $\overline{P}_e$ and $\overline{P}_m$ are electric and magnetic polarizations, respectively.

$$\overline{D} = \varepsilon_o \overline{E} + \overline{P}_e \tag{2.2a}$$

$$\overline{B} = \mu_o \left(\overline{H} + \overline{P}_m \right) \tag{2.2b}$$

$$\overline{P}_e = \varepsilon_o \chi_e \overline{E} \tag{2.3a}$$

$$\overline{P}_m = \chi_m \overline{H} \tag{2.3b}$$

The χ_e and χ_m terms are the electric and magnetic susceptibility of the material, respectively. Substituting (2.2) and (2.3) back into (2.1) yields Ampere's and Faraday's Laws when in the presence of matter, shown in (2.4).

$$\nabla \times \overline{H} = j\omega\varepsilon_o \overline{E} + j\omega \overline{P}_e + \overline{J} \tag{2.4a}$$

$$\nabla \times \overline{E} = -j\omega\mu_o \overline{H} - j\omega\mu_o \overline{P}_m - \overline{M} \tag{2.4b}$$

In order to keep the terminology and variables as close to common practice as possible, a minor alteration to (2.3) will be made in order to substitute the χ_e and χ_m terms for α_e and α_m, the electric and magnetic polarizability of the aperture, respectively. Again, this change in terms is merely conventional, as the physics of

susceptibility and polarizability are essentially the same; both terms describe how the presence of an object perturb the electric and magnetic fields from those in free-space. For the sake of completeness, (2.5) shows the substitution of α_e and α_m into (2.3). The inclusion of a negative sign in (2.5b) is done to account for the correct phase when the equivalent polarization currents are used to replace the aperture. Shown in Section 2, Figure 2.1 supplies visual evidence as to why this correction is needed, and will be described more in that section.

$$\overline{P}_e = \varepsilon_o \alpha_e \overline{E} \tag{2.5a}$$

$$\overline{P}_m = -\alpha_m \overline{H} \tag{2.5b}$$

2.2 EQUIVALENT APERTURE REPRESENTATION: BETHE'S THEORY

In [5], Bethe's work in describing the fields through diffraction of small holes is achieved by maintaining continuity of the fields through the aperture. For the special cases of circularly and elliptically shaped apertures, exact solutions were found where the non-zero tangential E-field is preserved through the aperture. After these rigorous derivations, Bethe rationalized that a simpler approach could be made towards electrically small holes, while still maintaining an acceptable representation of the fields radiated from the aperture. For electrically small apertures, Bethe stated that the fields significantly contributing to radiation can be assumed to be uniform over the aperture. The consequence of this assumption, along with simplified PEC boundary conditions for the enclosure walls, is that the only fields that are present in the aperture are tangential magnetic fields and normal electric fields.

Under this assumption that only tangential magnetic fields and normal electric fields are present at the aperture, consider again what is shown in (2.4). In the presence of some polarizable object, such as an aperture, the curling magnetic field in (2.4a) is due to the net effect of a time-varying electric field, a time-varying electric polarization current, and an electric current. Assuming that these apertures are not filled with any object other than vacuum, there is no matter to be polarized and no free electrons to cause conduction current. However, as the curling magnetic field is again due to the net effect of these three distinctly different physical phenomena, it would be possible to interpret and treat the time-varying electric field at the aperture as one of the other two terms, such as an equivalent time-varying electric polarization current, $j\omega\overline{P}_e$. In fact, (2.5a) has already shown that the electric polarization current is proportional to the electric field in the aperture by a factor of $\varepsilon_o\alpha_e$, where α_e accounts for the physical dimensions of the aperture. In doing this, the only difference in the interpretation of the physics of both scenarios is that the normal electric field would be considered to be evenly distributed over the entire aperture area when solving the radiation integrals, whereas the polarization current would be considered to be an infinitesimal current at the center of the aperture in the normal direction, $\hat{n}$. A similar argument can be made for (2.4b) and (2.5b), but would be redundant to describe in detail. Figure 2.1 gives a visual depiction of how the normal electric fields and tangential magnetic fields behave near an aperture, along with their equivalent electric and magnetic polarization current representations. Visually, one can see that when the normal electric field points out from the aperture in Figure 2.1a, an equivalent electric polarization current in the same

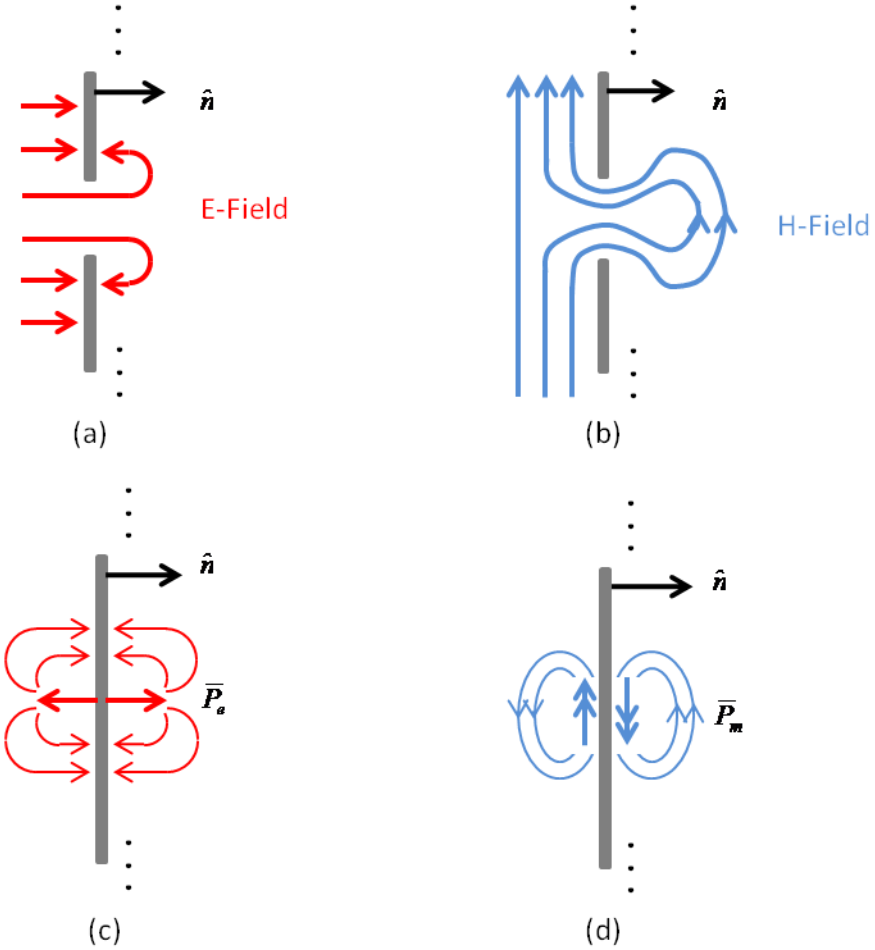

Figure 2.1. Visualization of the distorted electric and magnetic fields and equivalent electric and magnetic polarization currents near an aperture: (a) Electric field, (b) Magnetic field, (c) Electric polarization current, and (d) Magnetic polarization current. Reference: D. Pozar [8]

direction will induce an electric field in a similar manner in the radiating half-space of the aperture, shown in Figure 2.1c. However, when the tangential magnetic field is pointing towards the top of the page, as in Figure 2.1b, the equivalent magnetic polarization current in the radiating half-space must point down, 180^{o} out of phase from the incident

tangential magnetic field, in order to produce an H-field that corresponds to the original problem, shown in Figure 2.1d. Due to the replacement of the aperture with PEC in Figures 2.1c and 2.1d, the tangential electric field at the aperture is automatically forced to be zero.

By replacing the normal electric field and tangential magnetic field with polarization currents, (2.4) can be rewritten as:

$$\nabla \times \overline{H} = j\omega\varepsilon_o\alpha_e\overline{E}_n + \overline{J} \tag{2.6a}$$

$$\nabla \times \overline{E} = +j\omega\mu_o\alpha_m\overline{H}_{\tan} - \overline{M} \tag{2.6b}$$

As was already discussed, there is no electric conduction current, $\overline{J}$, or magnetic conduction current, $\overline{M}$, inside the aperture when it is filled with vacuum. However, since the equivalent time-varying polarization currents are interpreted as infinitesimal currents pointing in their respective directions, it would be feasible and convenient to consider these currents as electric and magnetic conduction currents, as there are well-known solutions to the inhomogeneous Helmholtz equation for line currents to describe the radiated fields from such sources. This leads to the final aperture equivalence, where it can be stated that the electric and magnetic polarization currents can be thought of as electric and magnetic conduction currents for easy substitution into the known radiation equations. This is summed up in (2.7).

$$\overline{J} = j\omega\varepsilon_o\alpha_e\overline{E}_n \tag{2.7a}$$

$$\overline{M} = -j\omega\mu_o\alpha_m\overline{H}_{\tan} \tag{2.7b}$$

2.3 RADIATION FROM EQUIVALENT POLARIZATION CURRENTS

With the electric and magnetic polarization currents being related to electric and magnetic conduction currents in (2.7), it is possible to use these relations to solve the inhomogeneous Helmholtz equation in (2.8) to find the radiated fields from the electric and magnetic equivalent aperture currents.

$$\nabla^2 \overline{A} + k^2 \overline{A} = -\mu \overline{J} \tag{2.8a}$$

$$\nabla^2 \overline{F} + k^2 \overline{F} = -\varepsilon \overline{M} \tag{2.8b}$$

Figure 2.2 shows the standard rectangular and spherical unit vectors that will be used throughout this section.

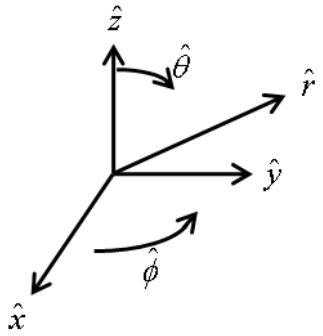

Figure 2.2. Rectangular and spherical coordinates used in the derivation of the radiated fields.

2.3.1 Radiation from the Electric Polarization Current. For aperture excitation by a normal electric field, Figure 2.3 depicts an E-field in the z-direction with the aperture in the x-y plane of an infinite PEC sheet, centered about the coordinate system origin. As Figure 2.1 and (2.7) suggest, E_{norm} can be replaced by an equivalent

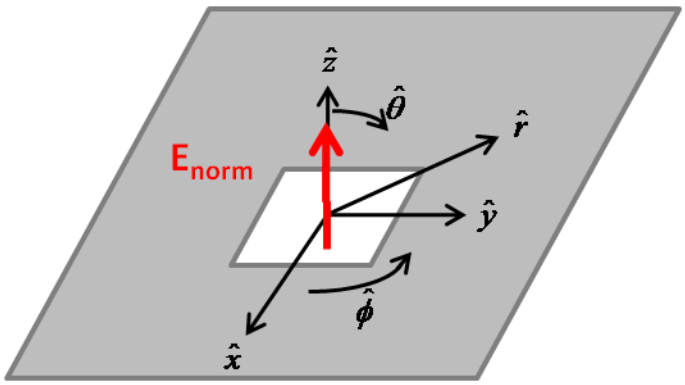

Figure 2.3. Aperture excited by an electric field normal to the plane of the aperture.

electric current, and the aperture can be replaced by PEC, shown below in Figure 2.4. In Figure 2.4, $J_{z,eq,z>0}$ is the equivalent electric current on the radiation side of the aperture, $J_{z,eq,z<0}$ is the equivalent electric current on the excitation side of the aperture, and $\left|J_{z,eq,z>0}\right| = \left|J_{z,eq,z<0}\right| = \left|J_{z,eq}\right|$. As the purpose of this section is to find the radiated fields from the equivalent electric current, only the current in the radiation half-space is of current concern. From image theory, it is possible to remove the PEC sheet, double the strength of the electric current, and solve for the radiated fields from the free-space

radiation equations, where the solution will only be valid in the region z > 0. This new scenario is shown in Figure 2.5.

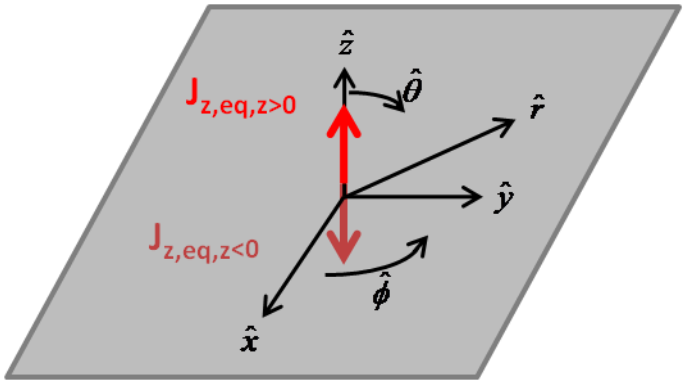

Figure 2.4. Equivalent electric currents and PEC for an aperture under electric field excitation.

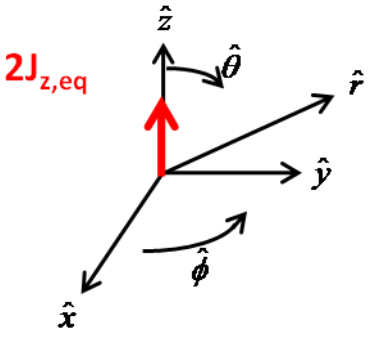

Figure 2.5. Equivalent electric current problem after applying image theory.

With the equivalent current in the radiation half-space only having a $\hat{z}$ component, (2.8a) reduces to

$$\nabla^2 A_z + k^2 A_z = -\mu 2 J_{z,eq} \tag{2.9}$$

where (2.9) can be solved for A_z to yield

$$A_z = \frac{2\mu}{4\pi} \int_{-l/2}^{+l/2} J_{z,eq} \frac{e^{-jkr}}{r} dl \tag{2.10}$$

The limits of integration from $-l/2$ to $+l/2$ represent a contour of infinitesimal length, l, that is along the $\hat{z}$ direction, located at the origin. Evaluation of this integral then gives (2.11).

$$E_\theta = j\eta \frac{k 2 J_{z,eq} l \sin\theta}{4\pi r} \left[1 + \frac{1}{jkr} - \frac{1}{(kr)^2} \right] e^{-jkr} \tag{2.11}$$

Converting (2.11) to rectangular coordinates and assuming that the point of interest is in the far-field, where $kr >> 1$, then

$$E_x = j\eta \frac{k 2 J_{z,eq} \sin\theta \cos\theta \cos\phi}{4\pi r} e^{-jkr} \tag{2.12a}$$

$$E_y = j\eta \frac{k 2 J_{z,eq} \sin\theta \cos\theta \sin\phi}{4\pi r} e^{-jkr} \tag{2.12b}$$

$$E_z = -j\eta \frac{k 2 J_{z,eq} \sin^2\theta}{4\pi r} e^{-jkr} \tag{2.12c}$$

As the point of interest also lies on the z-axis, where $\theta = 0^o$, (2.12) reduces to

$$E_x = E_y = E_z = 0 \tag{2.13}$$

The result in (2.13) shows that for an electrically small aperture that is excited by a normal electric field, the radiated far-fields at a point normal to the aperture from an equivalent electric polarization current are zero. In other words, the equivalent electric polarization current does not contribute to the far-fields at an observation point normal to the aperture.

2.3.2 Radiation from the Magnetic Polarization Current. For aperture excitation by a tangential magnetic field, Figure 2.6 shows a magnetic field directed in the $-\hat{y}$ direction that is at the aperture in the x-y plane of an infinite PEC sheet, centered about the coordinate system origin. Again using Figure 2.1 and (2.7), it can be seen that $H_{\tan}$ can be replaced by an equivalent magnetic current, and the aperture with PEC, shown in Figure 2.7. The same nomenclature as was used in Figure 2.4 is again used in Figure 2.7 to denote the equivalent magnetic currents on both sides of the former aperture. For the time being, only the magnetic current in the z > 0 half-space is of concern, so image theory can again be utilized to remove the PEC, double the magnetic

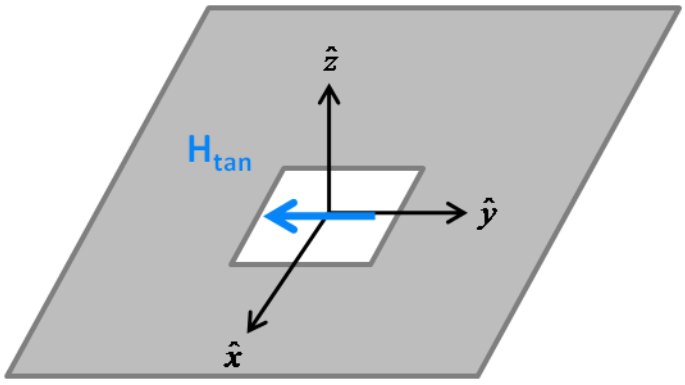

Figure 2.6. Aperture excited by a magnetic field tangential to the plane of the aperture.

current intensity, and solve for the radiated fields. This is depicted in Figure 2.8, where $\hat{r}^m = \hat{r}$, but $\hat{\theta}^m$ and $\hat{\phi}^m$ are now with respect to the y-axis. This choice of coordinates will make the following math much simpler.

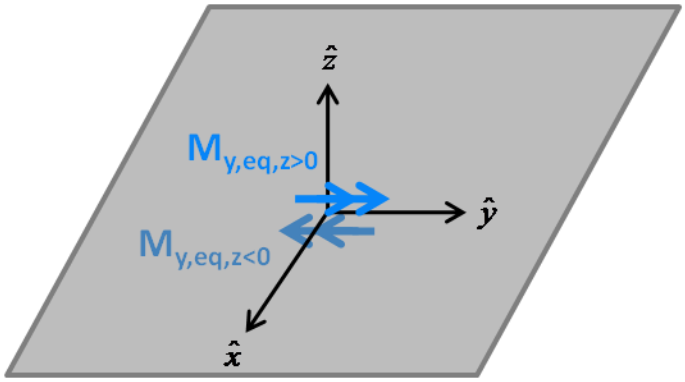

Figure 2.7. Equivalent magnetic currents and PEC for an aperture under magnetic field excitation.

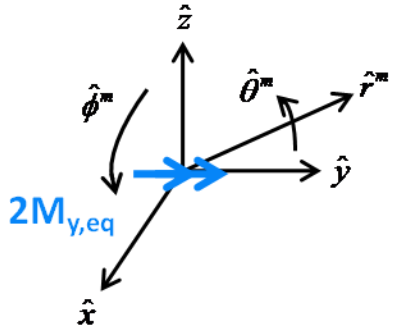

Figure 2.8. Equivalent magnetic current problem after applying image theory.

Using duality, (2.11) and (2.12) can be modified for use with a magnetic dipole without the redundancy of performing the above derivation a second time. For a magnetic dipole, the radiated magnetic field is

$$H_x = j\frac{k2M_{y,eq}\sin\theta^m\cos\theta^m\sin\phi^m}{4\pi\eta r}e^{-jkr} \tag{2.14a}$$

$$H_y = -j\frac{k2M_{y,eq}\sin^2\theta^m}{4\pi\eta r}e^{-jkr} \tag{2.14b}$$

$$H_z = j\frac{k2M_{y,eq}\sin\theta^m\cos\theta^m\cos\phi^m}{4\pi\eta r}e^{-jkr} \tag{2.14c}$$

Just as in the previous section, the assumption will be made that the point of interest is at a point along the z-axis, meaning that $\hat{\theta}^m = 90^o$ and $\hat{\phi}^m = 0^o$. This reduces (2.14) to

$$H_y = -j\frac{k2M_{y,eq}}{4\pi\eta r}e^{-jkr} \tag{2.15a}$$

$$H_x = H_z = 0 \tag{2.15b}$$

Note that the magnetic field is oriented in the $-\hat{y}$ direction, just as the incident magnetic field was, as shown in Figure 2.6. With the assumption that the observation point is in the far-field, the E-field can be related to the H-field by

$$\overline{E} = \eta\left(\overline{H}\times\hat{r}\right) \tag{2.16}$$

where $\hat{r}$ is the in the direction of the observation point (direction of propagation). Since $\overline{H}$ only has a $\hat{y}$ component, (2.16) becomes

$$\overline{E} = \eta H_y\left(\hat{y}\times\hat{z}\right) = E_x\hat{x} \tag{2.17a}$$

E_x can then be solved as

$$E_x = -j\frac{k2M_{y,eq}}{4\pi r}e^{-jkr} \tag{2.17b}$$

Substituting (2.7b) into (2.17b), the far-field radiation at a point normal to an electrically small aperture becomes

$$E_x = -\frac{k2\omega\mu_o\alpha_m H_y}{4\pi r}e^{-jkr} \tag{2.18}$$

$$|E| = \frac{k2\omega\mu_o\alpha_m|H_{\tan}|}{4\pi r} = \eta\frac{\omega^2\alpha_m|H_{\tan}|}{2\pi c^2 r} \tag{2.19}$$

where (2.19) is the general form of the far-field radiation intensity in the normal direction of a single, electrically small aperture. To solve for the intensity of the radiated fields, the only unknowns in (2.19) are the magnetic polarizability, α_m, which is a function of the physical dimensions of the aperture, and the intensity of the magnetic field that excites the aperture, $|H_{\tan}|$.

2.4 DETERMINING THE MAGNETIC POLARIZABILITY OF AN ELECTRICALLY SMALL APERTURE

As Cohn points out in [6], Bethe only solves the small hole problem for the cases of circularly and elliptically shaped apertures. Since exact analytical solutions for other geometries would be very useful but difficult to calculate, Cohn decided to use an experimental approach to determine the magnetic polarizability of different aperture shapes. While Cohn argued that making actual microwave measurements would result in about 10% experimental error, Cohn settled on creating an analog experiment within an electrolytic tank where the polarizabilities for apertures of rectangular, rounded-slot, cross rosette, dumbbell, and H-shaped cross sections were found.

While the experimental results of Cohn are original and very useful, they were presented in a graphical form that was not as convenient as they could be. In [7], McDonald started with the general form of magnetic polarizability, given as

$$\alpha_m = f\left(W/L\right)L^3 \tag{2.20}$$

where the polarizability is shown as the product of the largest aperture edge cubed, and a function that is dependent on the ratio of aperture width over length. From here, McDonald made a few observations about the properties of the magnetic polarizability of an aperture, namely that the function $f\left(W/L\right)$ should possess three distinct characteristics:

$$f\left(W/L\right) \to 0 \text{ as } \left(W/L\right) \to 0 \tag{2.21a}$$

$$f'\left(W/L\right) \to \infty \text{ as } \left(W/L\right) \to 0 \tag{2.21b}$$

$$f\left(W/L\right) \to \text{constant} \times \left(W/L\right) \text{ as } \left(W/L\right) \to \infty \tag{2.21c}$$

Using these characteristics, McDonald then found that $f\left(W/L\right)$ should be of the form

$$f\left(\alpha\right) = \frac{a}{\ln\left(1+\frac{b}{\alpha}\right)} \tag{2.22}$$

where α is the ratio W/L, and a and b are constants that are unique to every different aperture geometry.

To determine the coefficients a and b, McDonald used the experimental data from Cohn, and was able to determine that for a rectangular aperture,

$$f\left(\alpha\right) = \frac{0.132}{\ln\left(1+\frac{0.66}{\alpha}\right)} \tag{2.23}$$

where the values of α may range from 0 to 1. For this study, the geometry of interest is a square aperture, where $\alpha = 1$. This reduces (2.23) to

$$f(\alpha) = \frac{0.132}{\ln(1+0.66)} = 0.2604 \tag{2.24}$$

This ultimately leads to a magnetic polarizability of

$$\alpha_m = 0.2604L^3 \tag{2.25}$$

where L is the length of one side of the square aperture.

2.5 SOLVING FOR THE EXCITATION OF AN ELECTRICALLY SMALL APERTURE

With the magnetic polarizability of the electrically small square aperture having been solved for in the previous section, the only term left to determine in (2.19) is the intensity of the magnetic field that excites the aperture. Before examining the validity of (2.19) in the realistic scenario of apertures that are excited by an over-moded cavity, simulations were first done on aperture arrays placed in an infinite sheet of PEC, excited by a uniform plane wave (UPW) normal to the aperture array. The purpose of this was to study the radiated fields from a simple geometry and excitation in order to gain a sound understanding of the physics before attempting more complex simulations.

2.5.1 Excitation by Uniform Plane Wave. The first round of simulations that were conducted consisted of aperture arrays in an infinite sheet of PEC, illuminated by a UPW normal to the aperture array. To follow the same convention that was used in previous sections for finding the general form of the radiated fields from an aperture,

assume that the aperture array is excited by a UPW with $-\hat{x}$ polarization, and direction of propagation in the $\hat{z}$ direction. This is illustrated in Figure 2.9.

Referring back to Bethe's small hole theory, one of the assumptions made for determining the fields at an electrically small aperture was that the excitation fields are uniform over the aperture. Another way of interpreting this statement is to say that in the excitation half-space of the aperture, the perturbed fields due to the aperture, or the fields radiated by $J_{z,eq,z<0}$ and $M_{y,eq,z<0}$, are minimal and can be disregarded. With that being said, the reflection of the UPW at the PEC sheet, located at z = 0 and extending to infinity in the x- and y-directions, can be considered to be a complete reflection. Therefore, in the excitation half-space of z < 0, the superposition of the traveling waves are

$$E_{x,total} = E_x^i e^{-jkz} + E_x^r e^{jkz} \tag{2.26a}$$

$$H_{y,total} = H_y^i e^{-jkz} + H_y^r e^{jkz} \tag{2.26b}$$

where $E_x^r = \Gamma E_x^i$, $H_y^r = -\Gamma H_y^i$, and $\Gamma = -1$ for PEC boundary conditions. This leads to

$$E_{x,total} = E_x^i \left(e^{-jkz} - e^{jkz}\right) \tag{2.27a}$$

$$H_{y,total} = H_y^i \left(e^{-jkz} + e^{jkz}\right) \tag{2.27b}$$

$$E_{x,total} = -j2E_x^i \sin(kz) \tag{2.27c}$$

$$H_{y,total} = 2H_y^i \cos(kz) \tag{2.27d}$$

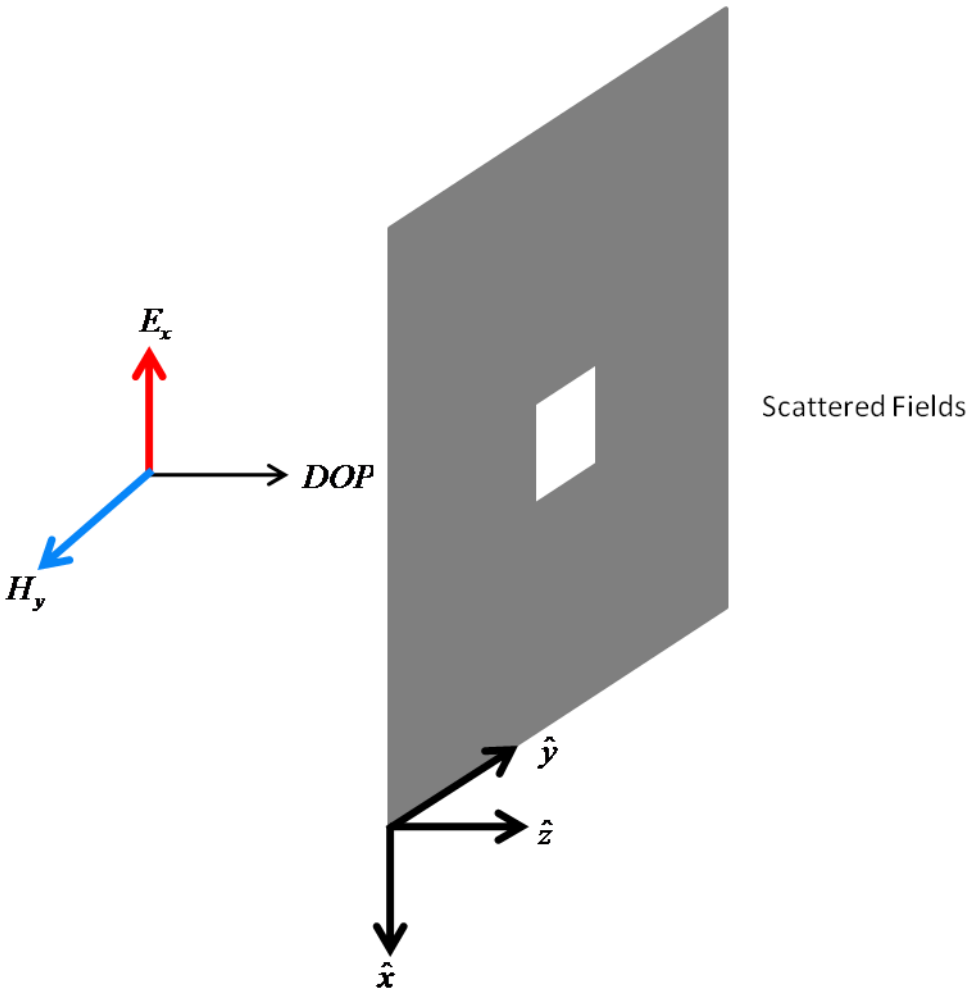

Figure 2.9. Graphical depiction of the illumination of a single square aperture by uniform plane wave.

where (2.27c-d) show that the fields in the excitation half-space for z < 0 are entirely composed of standing waves. (2.27c) shows that the tangential electric field at the PEC/aperture interface is zero, which is to be expected, while (2.27d) shows that the tangential magnetic field that excites the aperture is double the intensity of the incident tangential magnetic field, H_y^i. This can be summarized in (2.28) by stating

$$\left|H_{\tan}\right| = 2\left|H_y^i\right| \tag{2.28a}$$

$$\left|H_{\tan}\right| = \frac{2}{\eta}\left|E_x^i\right| \tag{2.28b}$$

The result in (2.28b) and (2.25) can then be plugged back into (2.19) to complete the solution for the radiated fields under UPW excitation as

$$\left|E\right| = \frac{0.2604\omega^2 L^3 \left|E_x^i\right|}{\pi c^2 r} \tag{2.29}$$

where (2.29) is a theoretical approximation of the far-field radiation intensity normal to a single, electrically small, square aperture that is illuminated by a UPW at normal incidence.

One of the unique and convenient qualities of a UPW is that when propagating in free-space, the magnitude of the wave does not decay by any factor of $\frac{1}{r^n}$, suggesting that the UPW extends to infinity in the directions traverse to the direction of propagation (DOP). For example, if no PEC sheet were present in Figure 2.9, then the intensity of the electric field at a point (x,y,z) = (0,0,1) would be the same at the point (x,y,z) = (0,0,-1), with the only discrepancy in the fields at these two points being be a phase difference, or a delay in the time-domain.

As the main concern for shielding effectiveness (SE) is magnitude, this allows for an easy definition of SE for UPW excitation. The general definition of SE is given as

$$SE_{linear} = \frac{Electric\_Field\_Intensity\_with\_No\_Shielding\_Mechanism}{Electric\_Field\_Intensity\_with\_Shielding\_Mechanism} \tag{2.30}$$

The result in (2.29) describes the electric field intensity when an aperture in an infinite PEC sheet is used as the shielding mechanism, while the previous paragraph described

how the electric field intensity at the point of interest is simply the magnitude of the incident wave. Combining this information together gives

$$SE_{linear} = \frac{\left|E_x^i\right|}{0.2604\omega^2 L^3 \left|E_x^i\right| / \pi c^2 r} = \frac{\pi c^2 r}{0.2604\omega^2 L^3} \tag{2.31a}$$

$$SE_{dB} = 20\log_{10}\left(\frac{\pi c^2 r}{0.2604\omega^2 L^3}\right) \tag{2.31b}$$

Knowing that the observation point will be at r = 3m, (2.31b) can be further reduced to

$$SE_{dB} = 338.3 - 20\log_{10}\left(f^2 L^3\right) \tag{2.32}$$

where (2.32) is a valid prediction of SE at a point 3m normal to a single, electrically small, square aperture that is illuminated by a UPW at normal incidence.

Thus far, the derivations and equations for this topic have been with respect to a single aperture. In reality, the application of the work summarized in this thesis will be towards arrays of hundreds, even thousands of apertures. To account for the number of apertures in the total radiation, two simple assumptions can be made. The first is that the array is excited uniformly, meaning that the fields at each aperture are of the same magnitude and phase. The second assumption is that the difference in distance from each aperture to the observation point is minimal, meaning that the area of the array is small with respect to the distance to the observation point at 3m. The impact of this assumption is that the $\frac{1}{r}$ decay of the field magnitude is the same for each aperture, and that the phase of all the radiated fields from the e^{-jkr} term is the same, so that the fields may sum constructively to produce the largest field intensity at the observation point. If both of these assumptions are made, then each additional aperture in the array will linearly

increase the estimated field strength at the observation point by a factor N, where N is the number of elements in the array. This alters (2.32) to ultimately yield a prediction of shielding effectiveness for an array of N number of electrically small, square apertures in an infinite PEC sheet, illuminated by a UPW at normal incidence, that is given by

$$SE_{UPW,dB} = 338.3 - 20\log_{10}\left(Nf^2L^3\right) \tag{2.33}$$

where the linear dependence on the N term is a valid assumption, so long as the area of the array is much smaller than the distance to the observation point at 3m normal to the center of the array. The N term can also be added to (2.19) to update the general expression to be

$$|E| = \eta \frac{N\omega^2 \alpha_m |H_{\tan}|}{2\pi c^2 r} \tag{2.34}$$

2.5.2 Excitation by Over-Moded Cavity. The process of solving for the fields at the apertures for an array backed by an over-moded cavity is much more involved than for illumination by a UPW. The first step is to find the energy stored at one of the cavity resonant frequencies, as these will be the frequencies where the largest spikes in EMI are expected to occur. Figure 2.10 shows the geometry of the enclosure and source, along with the coordinate system that will be used in this derivation. Assuming that the source for exciting the enclosure is a small line current with only a $\hat{y}$ component, such as a short dipole, the magnetic vector potential, $\bar{A}$, can be found by applying the electric boundary conditions to the enclosure walls. Doing so yields the expression shown in

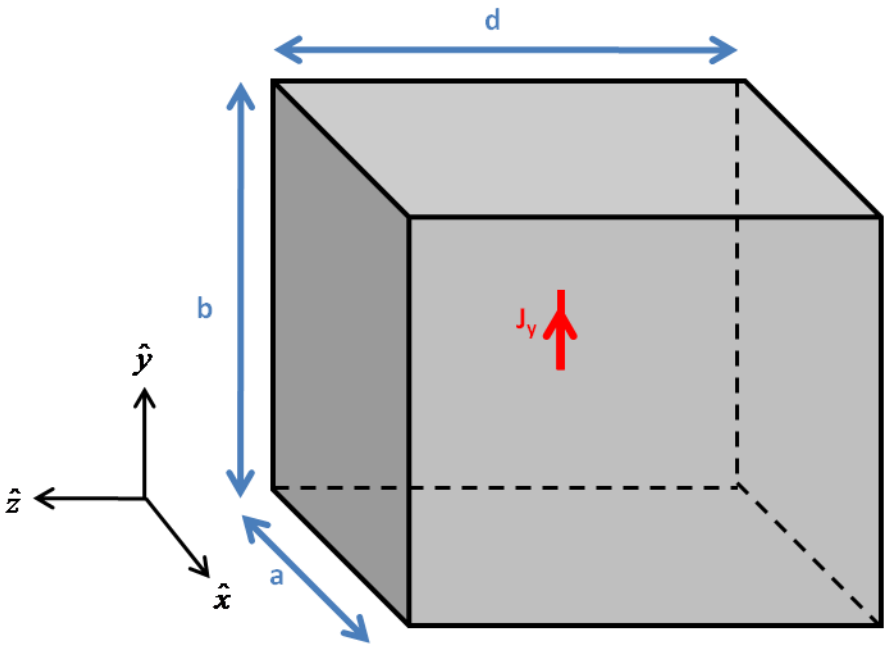

Figure 2.10. Visualization of the enclosure geometry and source used to derive the radiated field intensity from an array backed by an over-moded enclosure.

(2.35), where the coefficient B_{mnp} is a dependent on the intensity of J_y, the location of the source, and the modal structure inside the enclosure. The terms k_x, k_y, and k_z are the wave numbers in the x-, y-, and z-directions, respectively.

$$A_y(x,y,z) = B_{mnp}\sin(k_x x)\sin(k_y y)\cos(k_z z) \tag{2.35}$$

Due to the geometry of the source, it can be shown that only TE modes will be excited within the enclosure, as there will be no spatial field variation in the y-direction. As only electric sources as present inside the enclosure, the magnetic field can be found using

$$\overline{H} = \frac{1}{\mu} \nabla \times \overline{A} \tag{2.36}$$

With only a y-component for $\overline{A}$, the H-field is found to be

$$H_x = \frac{1}{\mu} \frac{\partial A_z}{\partial y} = \frac{-k_z}{\mu} B_{mnp} \sin(k_x x) \cos(k_y y) \cos(k_z z) \tag{2.37a}$$

$$H_z = \frac{1}{\mu} \frac{\partial A_z}{\partial x} = \frac{k_x}{\mu} B_{mnp} \cos(k_x x) \cos(k_y y) \sin(k_z z) \tag{2.37b}$$

By integrating the magnetic field over the entire enclosure, the total magnetic field energy can be doubled to yield the total energy stored in a TE mode at resonance by

$$W_{TE,total} = 2W_m = 2\frac{\mu}{4} \int_V \left|\vec{H}\right|^2 dV \tag{2.38a}$$

$$W_{TE,total} = \frac{\mu}{2} \int_0^a \int_0^b \int_0^d \left(H_x H_x^* + H_z H_z^*\right) dz dy dx \tag{2.38b}$$

$$W_{TE,total} = \frac{\mu}{2} \int_0^a \int_0^b \int_0^d \left(\begin{array}{l} \frac{k_z^2}{\mu^2} B_{mnp}^2 \sin^2(k_x x) \cos^2(k_y y) \cos^2(k_z z) + \\ \frac{k_x^2}{\mu^2} B_{mnp}^2 \cos^2(k_x x) \sin^2(k_y y) \cos^2(k_z z) \end{array} \right) dz dy dx \tag{2.38c}$$

$$W_{TE,total} = \frac{\mu}{2} \left(\left(\frac{k_z}{\mu} B_{mnp} \right)^2 \frac{a}{2} \frac{b}{2} \frac{d}{2} + \left(\frac{k_x}{\mu} B_{mnp} \right)^2 \frac{a}{2} \frac{b}{2} \frac{d}{2} \right) \tag{2.38d}$$

$$W_{TE,total} = \frac{B_{mnp}^2}{2\mu} \left(\frac{abd}{8} \right) \left(k_x^2 + k_z^2\right) \tag{2.38e}$$

Assuming that the aperture array will be located along the enclosure face on the $+\hat{x}$ side of the box, the z-component of the H-field will serve as the $\left|H_{\tan}\right|$ term in (2.34) Referring back to (2.37b), the magnitude of H_z is

$$|H_z| = \frac{k_x}{\mu}|B_{mnp}|$$

Relating the total energy stored in the cavity to the input power by the Q-factor of the enclosure, using $W = \frac{QP_o}{\omega}$, $|H_z|$ can be solved for in terms of characteristics of the enclosure and the power delivered to the enclosure by the source, as shown in (2.39).

$$W_{TE,total} = \frac{B_{mnp}^2}{2\mu}\left(\frac{abd}{8}\right)\left(k_x^2 + k_z^2\right) = \frac{QP_o}{\omega} \tag{2.39a}$$

$$\frac{k_x^2 B_{mnp}^2}{2\mu}\left(\frac{abd}{8}\right)\left(\frac{k_z^2}{k_x^2} + 1\right) = \frac{QP_o}{\omega} \tag{2.39b}$$

$$\frac{k_x^2 B_{mnp}^2}{2\mu^2}\left(\frac{abd}{8}\right)\left(\frac{k_z^2}{k_x^2} + 1\right) = \frac{QP_o}{\omega\mu} \tag{2.39c}$$

$$\frac{k_x^2 B_{mnp}^2}{\mu^2} = \frac{QP_o}{\omega\mu}(2)\left(\frac{8}{abd}\right)\left(\frac{1}{\frac{k_z^2}{k_x^2} + 1}\right) \tag{2.39d}$$

$$|H_z| = \frac{k_x B_{mnp}}{\mu} = \sqrt{\frac{16QP_o}{\omega\mu V\left(\frac{k_z^2}{k_x^2} + 1\right)}} \tag{2.39e}$$

Substituting (2.39e) into (2.34) yields

$$|E| = \eta\frac{N\omega^2\alpha_m}{2\pi c^2 r}\sqrt{\frac{16QP_o}{\omega\mu V\left(\frac{k_x^2}{k_z^2} + 1\right)}}$$

$$|E| = N\frac{\left(3.9\times10^{-15}\right)L^3 f^{3/2}}{\ln\left(1 + \frac{0.66}{\alpha}\right)r}\sqrt{\frac{QP_o}{\frac{1}{2}\mu V\left(\frac{k_x^2}{k_z^2} + 1\right)}} \tag{2.40}$$

where (2.40) is the same expression as (1.1). In (1.1), $\alpha = \frac{L}{W}$, whereas in (2.40), $\alpha = \frac{W}{L}$, which leads to the same result. Also, the difference in wave number notation of using $\frac{k_x^2}{k_z^2}$ in (2.40) as opposed to $\frac{k_x^2}{k_y^2}$ in (1.1) is merely a difference in coordinates. Both ratios bear the same physical significance.

Examining (2.40), it should be noted that the ratio $\frac{k_x^2}{k_z^2}$ is not only frequency dependent, but is also dependent on the enclosure dimensions. As the entire denominator underneath the square root of (2.40) appears as $\frac{1}{2}\mu V\left(\frac{k_x^2}{k_z^2}+1\right)$, it can be argued that the worst-case EMI intensity from the aperture will occur when the ratio of wave numbers is small, such that $k_z >> k_x$, and the denominator is as small as possible. Making this assumption, (2.40) reduces to

$$|E| = N\frac{\left(3.9\times10^{-15}\right)L^3 f^{3/2}}{\ln\left(1+\frac{0.66}{\alpha}\right)r}\sqrt{\frac{QP_o}{\frac{1}{2}\mu V}} \tag{2.41}$$

Remembering that this study is focused on square apertures, where $\alpha = 1$, (2.41) can be reduced again to

$$|E| = N\frac{\left(7.7\times10^{-15}\right)L^3 f^{3/2}}{r}\sqrt{\frac{QP_o}{\frac{1}{2}\mu V}}$$

$$|E| = N\frac{\left(9.7\times10^{-12}\right)L^3 f^{3/2}}{r}\sqrt{\frac{QP_o}{V}} \tag{2.42}$$

For reasons that will be discussed in Section 4, a dipole was chosen as the source for the enclosure simulations. For a small dipole, the radiated power into free-space is

$$P_{rad} = \eta \frac{\pi}{3} \left| \frac{I_o l}{\lambda} \right|^2 \tag{2.43}$$

where I_o is the current on the dipole (assumed to be uniform), and l is the length of the dipole. Assuming that the presence of the enclosure does not severely disrupt the current on the antenna, the radiated power from the small dipole inside the enclosure can be assumed to be the same as the power radiated into free-space, as shown in (2.44).

$$P_o = P_{rad} \tag{2.44}$$

Using (2.43) and (2.44), (2.42) can be rewritten as

$$|E| = N \frac{\left(9.7 \times 10^{-12}\right) L^3 f^{3/2}}{r} \sqrt{\frac{Q \eta \pi |I_o l|^2}{3V\lambda^2}}$$

$$|E| = \left(6.4 \times 10^{-19}\right) \frac{N L^3 f^{5/2} |I_o| l}{r} \sqrt{\frac{Q}{V}} \tag{2.45}$$

where (2.45) is an envelope approximation of the worst-case EMI to radiate from an aperture array backed by an over-moded cavity.

To recap, the assumptions made over which (2.45) is valid are that the apertures are square and electrically small, that the observation point is located in the far-field at a point 3m from the center of the aperture array, the apertures are uniformly illuminated, and the difference in distance from each aperture to the observation point is the same, such that all $\frac{1}{r}$ decay terms and all e^{-jkr} phase terms are the same and constructively combine at the observation point.

Referring back to (2.30), where SE was defined as the ratio of the "Electric Field Intensity with No Shielding Mechanism" divided by the "Electric Field Intensity with Shielding Mechanism", the reader can see that (2.45) can be used as the denominator in (2.30), while the far-field radiated intensity from a small dipole can be used as the numerator, given as

$$|E|_{dipole} = \eta \frac{2\pi f |I_o| l \sin\theta}{4\pi r c} \tag{2.46}$$

By using (2.45) and (2.46) in (2.30), the worst-case SE for an aperture array backed by an over-moded cavity is found to be

$$SE = \left(9.8 \times 10^{11}\right) \frac{1}{N f^{3/2} L^3} \sqrt{\frac{V}{Q}} \tag{2.47}$$

$$SE_{Enc,dB} = 240 - 20\log_{10}\left(N f^{3/2} L^3\right) + 10\log_{10}\left(\frac{V}{Q}\right) \tag{2.48}$$

where the observation point is 3m normal from the center of the enclosure wall with the aperture array. The same assumptions that apply to (2.45) also apply to (2.48).

Certain limitations do apply to (2.48). For example, if the number of apertures, N, were to approach infinity, then (2.48) suggests that the SE of the array would reduce to -∞. However, if the volume, V, were allowed to approach infinity along with N, while Q and L remained constant, then the area of the array needed to accommodate an infinite number of apertures would need to increase to an infinite size, which would severely violate the assumption that the array size is much less than the distance from the apertures to the observation point at 3m. In such a scenario, the $\frac{1}{r}$ decay term and e^{-jkr}

phase term of each individual aperture would become important and need to be considered, which is a problem that has been solved by Kaden.

Conversely, if N is allowed to approach infinity, but the enclosure dimensions and Q are fixed, such that L must approach zero in order to make room for all the apertures, (2.48) would yield an infinite value of SE. With the array face of the enclosure completely filled with apertures, the limited size of the enclosure wall relates to the size and number of apertures by $Area = NL^2$, where the spacing between apertures is also allowed to decrease to zero, for simplicity. As N increases by some factor A, L would be forced to decrease by $A^{-1/2}$. Putting these trends back into (2.48) and assuming that the area of the wall is $1m^2$, such that N = 1 and L = 1m initially for simplicity, for a fixed frequency, (2.48) would become

$$SE_{Enc,dB} = 240 - 20\log_{10}\left(C_1 A\left(A^{-1/2}\right)^3\right) + 10\log_{10}\left(C_2\right)$$

$$SE_{Enc,dB} = 240 - 20\log_{10}\left(C_1 A^{-1/2}\right) + 10\log_{10}\left(C_2\right)$$

$$SE_{Enc,dB} = 240 + 10\log_{10}\left(A\right) - 20\log_{10}\left(C_1\right) + 10\log_{10}\left(C_2\right) \qquad (2.49)$$

where C_1 and C_2 are constants, and as the number of apertures, in this case A, increases to infinity, (2.49) shows that the SE of the array also increases to infinity. This result reflects the trend that for a fixed amount of open aperture area, it is better to use many apertures with small dimensions, rather than few apertures with large dimensions.

2.6 THE EFFECT OF MUTUAL COUPLING ON RADIATED FIELD INTENSITY

The general expression in (2.19) is a good approximation for the far-field radiation intensity in the normal direction from a single electrically small aperture in an infinite PEC sheet. In Section 2.5.1, a logical and accurate means of accounting for radiation by multiple apertures is presented and incorporated into the approximations of (2.33), (2.34), and (2.48), but these approximations are still based on the radiation from a single aperture in an infinite PEC sheet. When multiple apertures are positioned in electrically close proximity to one another, the apertures will interact, changing their impedance, and ultimately impacting the radiated electric field intensity.

In [2], Min Li looked at the effect of mutual coupling between closely spaced apertures. To examine this numerically, Li created a 3x3 aperture array in an infinite PEC sheet of zero thickness, aperture dimensions of 2cm on each side, a spacing of 1cm between each aperture, and used the Method of Moments (MoM) to determine the magnetic current density for the center aperture of the array at 1GHz. Though it may seem contradictory to examine the magnetic current density in an electrically small aperture after arguing that the tangential electric field inside such an aperture is assumed to be zero according to Bethe, since $\overline{M} = \overline{E} \times \hat{n}$, the truth is that this tangential E-field is always present and can be used in this way to characterize the mutual coupling between apertures. By finding $\overline{M}$ in this equivalent problem, the E-field could then be determined by solving the inhomogeneous Helmholtz Equation of (2.8b) to solve for $\overline{F}$, and then assuming that the observation point is in the far-field to yield

$$\overline{E} = j\omega\overline{F} \tag{2.50}$$

The mutual coupling between apertures and increased radiated field intensity are related by

$$E_{mutual} = (1 + C_m) E_{single} \tag{2.51}$$

where E_{single} is the radiated electric field intensity from a single aperture, E_{mutual} is the contribution to the total radiated electric field intensity from a single aperture when interacting with nearby apertures, and C_m is the mutual coupling coefficient. Since $\overline{E}$ and $\overline{F}$ are related by (2.50), and $\overline{M}$ and $\overline{F}$ are related by (2.8b), then it can be roughly assumed that $\overline{E} \propto \overline{M}$, so that (2.51) can be rewritten as

$$M_{mutual} = (1 + C_m) M_{single} \tag{2.52}$$

Lastly, noting again that $\overline{M} = \overline{E} \times \hat{n}$, (2.52) can again be simplified to

$$E_{\tan, aperture, mutual} = (1 + C_m) E_{\tan, aperture, single} \tag{2.53}$$

where $E_{\tan, aperture, multual}$ is the tangential component of the electric field inside of centermost aperture in an array, and $E_{\tan, aperture, single}$ is the tangential component of the electric field inside of a single aperture.

To reexamine the impact of mutual coupling on increased radiated field intensity, a similar series of experiments were conducted as those done by Min Li. Each of the experiments utilized a 9x9 array in an infinite PEC sheet of zero thickness, a constant aperture size of 3mm, and varying spacing between apertures from 1mm to 5mm, as shown in Figure 2.11. Using the time-domain solver in CST, the aperture array was illuminated by a UPW propagating normal to the aperture array, and the electric field was sampled by an E-field probe in the middle of the centermost aperture with the same

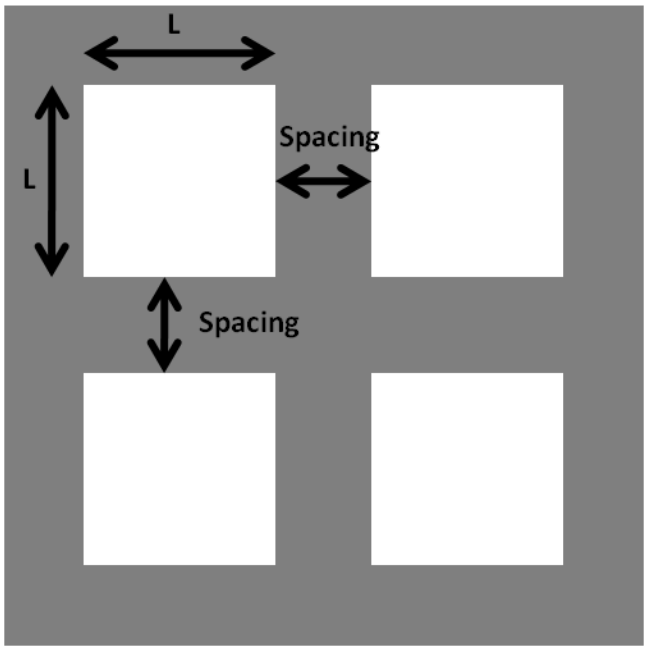

Figure 2.11. Visual aid in the definition of aperture size, L, and aperture spacing.

polarization as the incident wave. This is the same experimental setup used in the UPW models of Section 3, and the figures provided there will give a better description of the geometry used. The results of these simulations, along with Min Li's original results, are shown in Figures 2.12, 2.13, and 2.14.

Figure 2.10 shows the coupling coefficient, C_m, for different aperture spacing over the frequency band of 1GHz to 20GHz. The data provided shows that the mutual coupling between apertures is not a simple relation, but instead varies drastically over frequency. As the concern of this paper is to predict the worst-case radiated intensity from these aperture arrays, it would seem logical to approximate C_m over all frequencies for each individual aperture spacing as the maximum value from Figure 2.12 for each

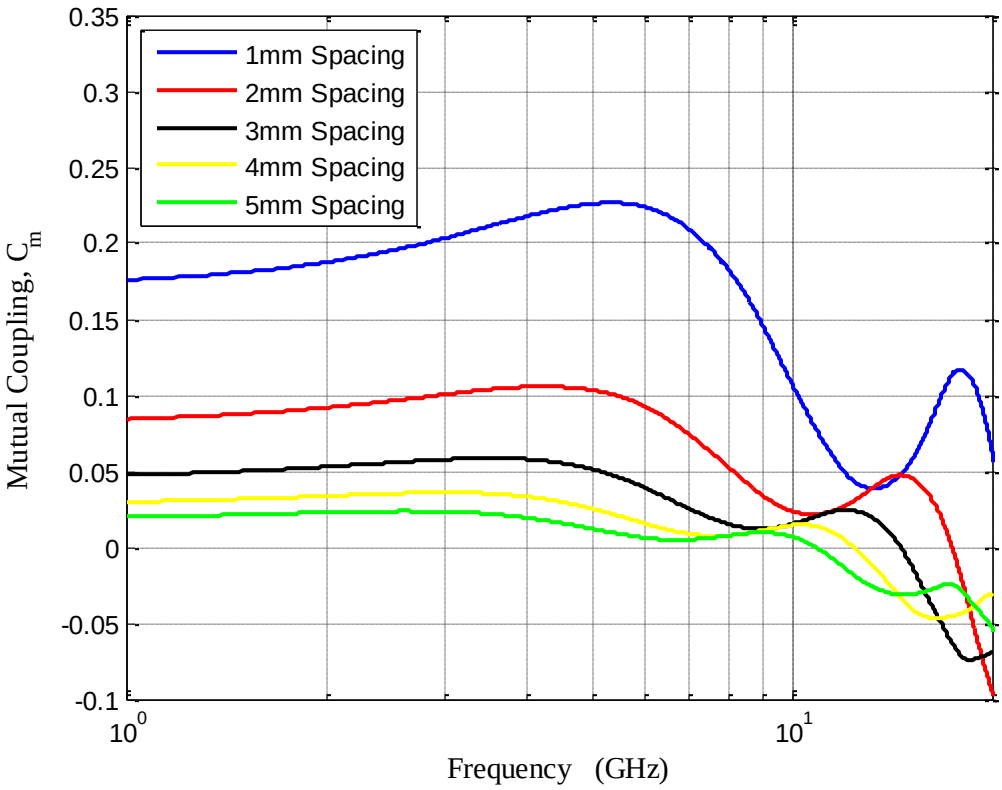

Figure 2.12. Coupling coefficient for different aperture spacing from 1GHz to 10GHz.

size to spacing ratio. For this reason, Figure 2.13 is a plot of the worst-case value of C_m per ratio of aperture spacing over aperture size. For the sake of comparison, the results from Min Li's MoM simulations are also included on the plot.

Aside from when the ratio of aperture spacing over aperture size becomes very small, the new simulation results yield larger values of C_m compared to those produced by Min Li. This trend was expected, as Min Li's simulations only consisted of a 3x3 array, while the new simulations consisted of a 9x9 array, so all the apertures

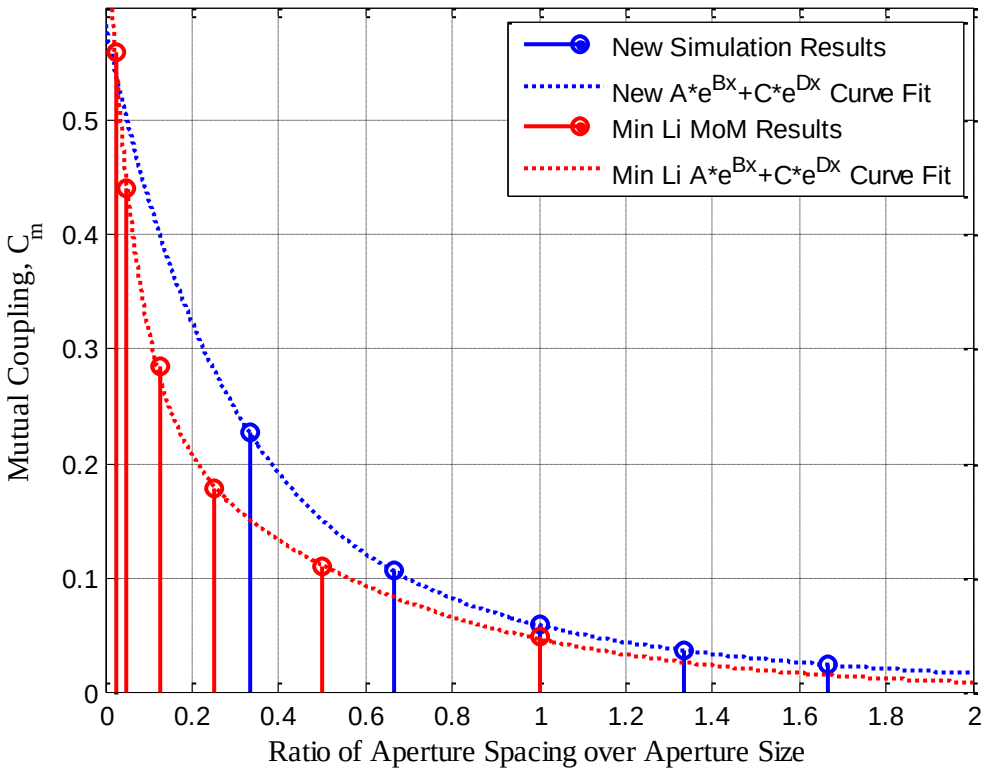

Figure 2.13. Worst-case mutual coupling coefficient per ratio of aperture spacing over aperture size.

immediately adjacent to the centermost aperture also experienced an enhanced excitation due to mutual coupling with neighboring apertures. Also, as actual aperture arrays in shielding enclosures generally consist of a large number of apertures on the order of millimeters in size, the basic model used in the new simulations is more realistic.

As for the curve-fitted data in Figure 2.13, the double exponential function, of the form $Ae^{Bx}+Ce^{Dx}$, was chosen as the general form of the fit because this function tended to yield the least amount of error in the least complicated form. In other words, there is

no mathematical or physics-based reason for choosing this function, other than it produced the smallest least-squared error in the least complicated function. For the new simulations, the coefficients for the curve-fitting are given as A = 0.4345, B = -3.773, C = 0.1502, and D = -1.132.

Using the new fitted-curve from Figure 2.13 to predict the coupling coefficient, or increase in field intensity, over a wide range of relevant aperture spacing to size ratios, Figure 2.14 shows the predicted impact that aperture spacing will have on the overall shielding effectiveness of aperture arrays. As (2.53) suggests, a positive value for C_m results in an increased electric field intensity at the observation point, which lowers the shielding effectiveness of the array. To arrive at the curve in Figure 2.14, (2.54) is used to convert the linear coupling coefficient to decibels.

$$MC_{dB} = 20\log_{10}\left(1 + 0.4345e^{-3.773x} + 0.1502e^{-1.132x}\right) \tag{2.54}$$

where $x = \dfrac{Aperture\_Spacing}{L}$. Using (2.54) as a corrective term for the predicted SE and field intensities derived in this section, the approximations can now be finalized as

$$E_{dB,General} = 20\log_{10}\left(\eta\frac{N\omega^2\alpha_m\left|H_{\tan}\right|}{2\pi c^2 r}\right) + MC_{dB} \tag{2.55}$$

$$E_{dB,UPW} = -338 + 20\log_{10}\left(Nf^2L^3\left|E^i\right|\right) + MC_{dB} \tag{2.56}$$

$$E_{dB,Enc} = -373 + 20\log_{10}\left(NL^3f^{5/2}\left|I_o\right|l\right) + 10\log_{10}\left(\frac{Q}{V}\right) + MC_{dB} \tag{2.57}$$

$$SE_{dB,UPW} = 338 - 20\log_{10}\left(Nf^2L^3\right) - MC_{dB} \tag{2.58}$$

$$SE_{dB,Enc} = 240 - 20\log_{10}\left(Nf^{3/2}L^3\right) + 10\log_{10}\left(\frac{V}{Q}\right) - MC_{dB} \tag{2.59}$$

where (2.55) through (2.59) are worst-case envelope approximations for the radiated field intensity and SE of aperture arrays in an infinite PEC sheet and for aperture arrays backed by over-moded cavities. One last time, the assumptions made over which these equations are based are that the apertures are square and electrically small, that the observation point is located in the far-field at a point 3m from the center of the aperture array, the apertures are uniformly illuminated, and that the difference in distance from each aperture to the observation point is the same, such that all $\frac{1}{r}$ decay terms and all e^{-jkr} phase terms are the same, so that fields constructively combine at the observation point.

Even though the effect of mutual coupling appears to increase the radiated field intensity by only 4dB in the most extreme aperture size to spacing ratio, accounting for MC helps in reducing the error between the simulation results of Sections 3 and 4 and the approximations given in (2.58) and (2.59). Because of the small reduction in error and the simplicity in calculating MC, the MC terms shall be used throughout.

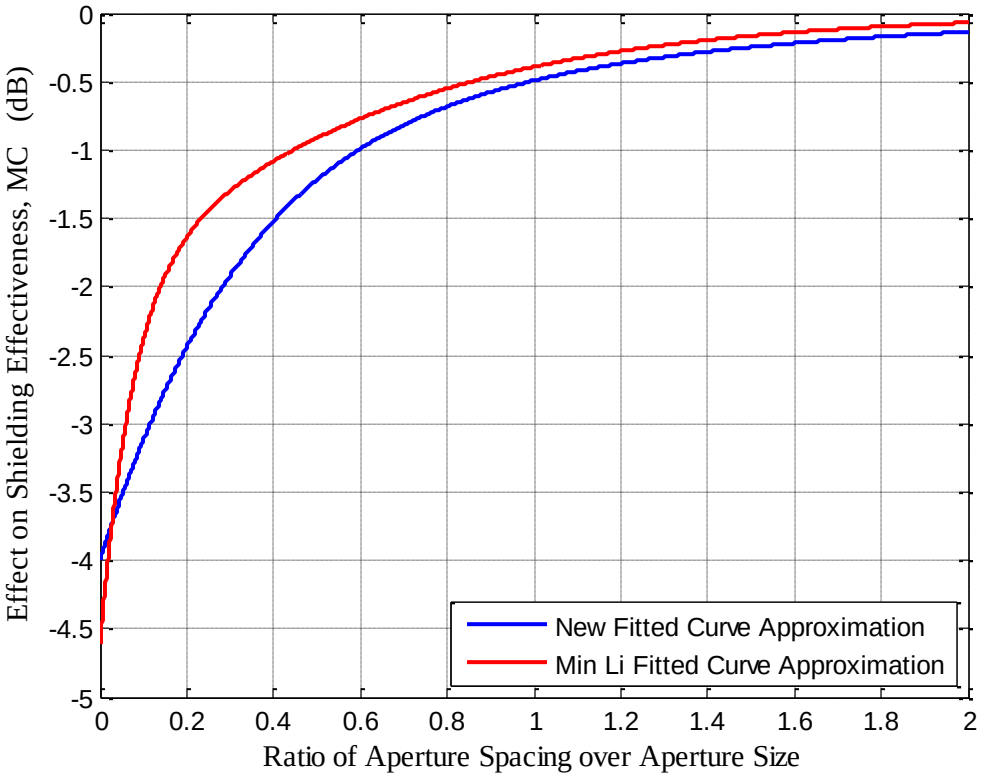

Figure 2.14. Estimated impact of mutual coupling of shielding effectiveness.

3 UNIFORM PLANE WAVE SIMULATIONS AND RESULTS

Before jumping in and performing simulations on aperture arrays backed by over-moded cavities, where the physics of the problem are not quite straightforward, the first set of simulations to verify (2.55) will consist of aperture arrays in an infinite PEC sheet of zero thickness using the time-domain solver in CST Microwave Studio. To achieve uniform excitation over all apertures, the array will be excited by a uniform plane wave (UPW) propagating at normal incidence to the array. By setting up the simulations in this manner, many of the complications of the cavity-backed models will be avoided, so as to gain a better understanding of the physics with more basic models first.

3.1 PROPOSED SIMULATION PLAN

Observing (2.56) and (2.58), which are extensions of (2.55), one will notice that the approximations are only a function of five variables: excitation amplitude ($\left|E^i\right|$), aperture size (L), aperture spacing (MC), number of apertures (N), and frequency (f). As each simulation will be conducted using the time-domain solver in CST Microwave Studio, the nature of this solver will allow for broadband results, which takes care of testing the frequency dependence. The excitation amplitude, $\left|E^i\right|$, is only a factor for predicting the envelope of the E-field, which is not of primary concern in this study, but can easily be set so that $\left|E^i\right| = 1$. For testing the number of apertures, N, several models were run that have the same sized apertures with the same spacing between each one, but with varying array sizes. For testing the aperture spacing, several models were run that

have the same sized apertures, the same number of apertures, but with varying distances between the apertures in each model. The length of the aperture side, L, was tested by running multiple models with the same number of apertures, the same spacing to aperture size ratio, but with varying aperture lengths. A list of all the models that were run and will be discussed in this section is provided in Table 3.1.

Table 3.1. Summary of Uniform Plane Wave Simulations.

	Array Size	**Aperture Size**	**Aperture Spacing**
N	05x05	3mm	1mm
	09x09	3mm	1mm
	13x13	3mm	1mm
	17x17	3mm	1mm
	21x21	3mm	1mm
L	Single	3mm	N/A
	Single	6mm	N/A
	Single	9mm	N/A
	07x07	3mm	1mm
	07x07	6mm	2mm
	07x07	9mm	3mm
MC	09x09	3mm	1mm
	09x09	3mm	2mm
	09x09	3mm	3mm
	09x09	3mm	4mm
	09x09	3mm	5mm

3.2 GENERIC CST MODEL FOR UNIFORM PLANE WAVE SIMULATIONS

For all the UPW models discussed in this section, a variant of a single generic model was used for each simulation that was conducted. A view of the full three-dimensional computational domain is shown in Figure 3.1. In each model, a sheet of zero thickness PEC was placed at x = 0 and extended to the edges of the domain in the y- and z-directions. By doing, this tells the solver that the PEC sheet should extend to infinity when computing the far-field during post-processing, creating a decoupling plane. The aperture arrays were centered on this sheet, and given enough space from the edge of the array to the edge of the domain, so as to not cause any strange behavior from the perfectly matched layer (PML) absorbing boundary condition (ABC). This minimum space between the edge of the array and the PML boundary was chosen at the author's discretion. The distance of 400mm from the aperture array to the edge of the domain in

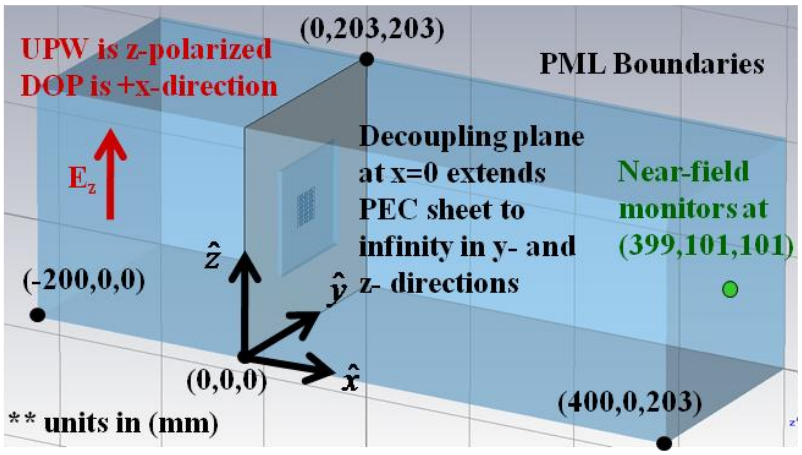

Figure 3.1. Generic CST model used for the uniform plane wave simulations with units of millimeters (mm).

the +x-direction was chosen through experimentation to yield confident results over more than a decade in the gigahertz range. The space of 200mm from the PEC sheet to the edge of the domain in the –x-direction was again chosen at the author's discretion to minimize potential problems with the PML ABC that may have occurred when scattered fields were incident upon the boundaries after reflecting off the array and PEC sheet.

Localized meshing was utilized in the cross-section of the apertures in order to ensure that a good representation of the coupled fields was achieved. Figure 3.2 shows the meshing cross-section across a selected few apertures from an array. The mesh cells shown in Figure 3.2 are 0.25mm x 0.25mm in the x-y plane. For the smallest studied aperture size of 3mm x 3mm, this is a total of 144 mesh cells per aperture, which is more than enough cells to get an accurate representation of the coupled fields. This meshing scheme is done over the entire aperture array and extends at least 5mm beyond the

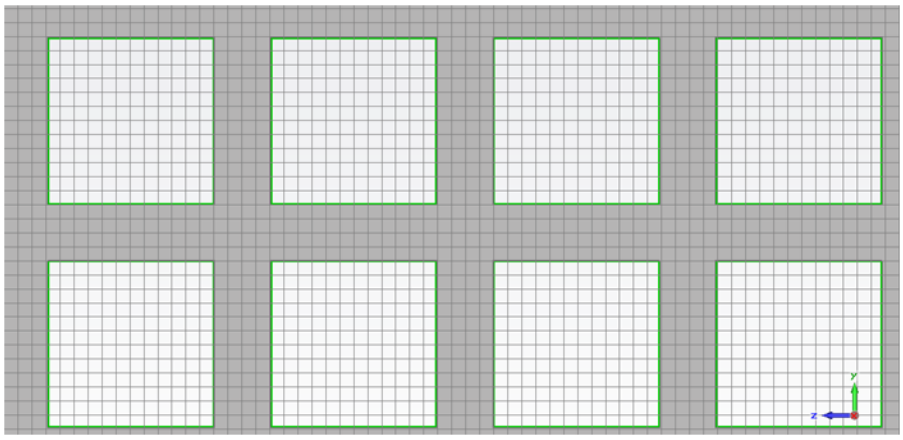

Figure 3.2. Cross-section of aperture meshing in uniform plane wave generic model.

largest array. Aside from this local meshing, the solver was allowed to choose the cell sizes for the rest of the domain. Figure 3.3 shows the meshing of the apertures in the x-y plane, which is also the same as is the x-z plane. Near the array, the x-component of the mesh cells was 1mm in length, and then automatically selected by the solver for the rest of the domain. The total number of mesh cells for each model was approximately 44 million.

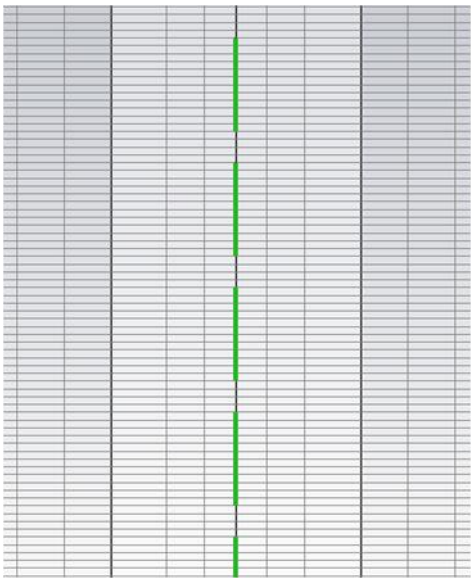

Figure 3.3. Meshing of the apertures in the x-y plane for the uniform plane wave generic model.

As the name of this section suggests, the excitation for each model studied in this section was a UPW. These UPWs were polarized in the +y-direction, and were generated

at the edge of the domain on the –x face, and propagated in the +x-direction, striking the array at normal incidence and causing maximum coupling through the arrays.

Figure 3.4 shows the first 200ps of the excitation signal in the time-domain, while Figure 3.5 shows the normalized magnitude spectrum in the frequency-domain. Each model was set up for a maximum frequency of 20GHz, and Figure 3.5 clearly shows that by 20GHz, the excitation signal has already rolled-off by 20dB. The frequency content in Figure 3.5 begins at 281MHz, which coincides with the total simulation time of 3.55nsec.

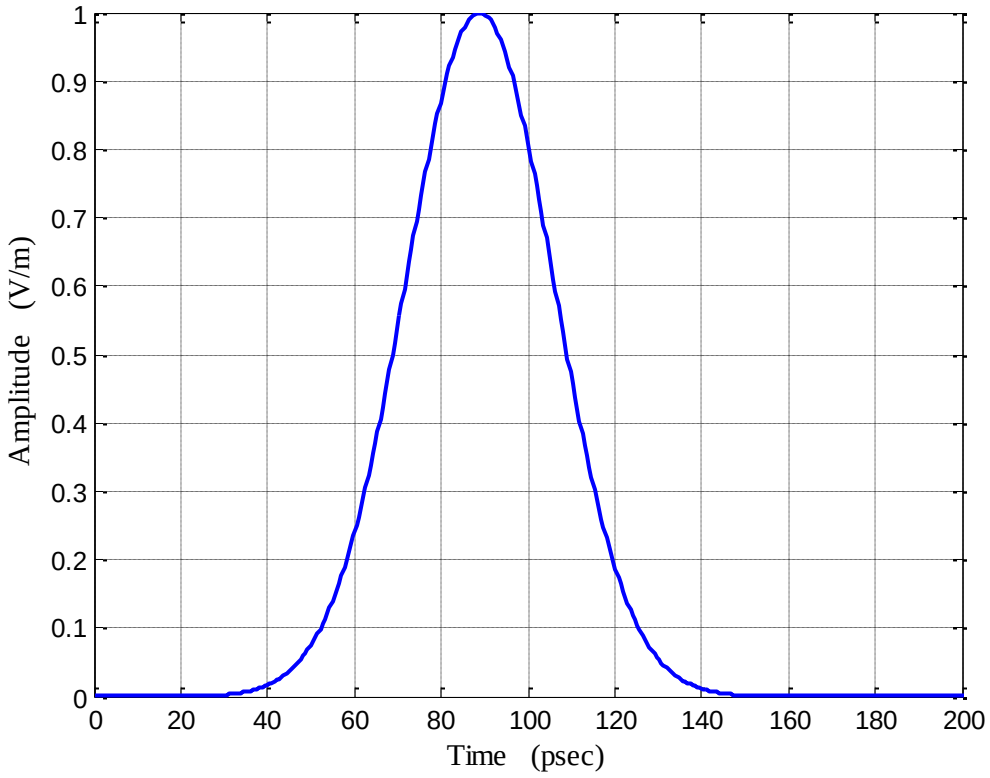

Figure 3.4. Time-domain of the Gaussian pulse used for the excitation of the uniform plane wave models.

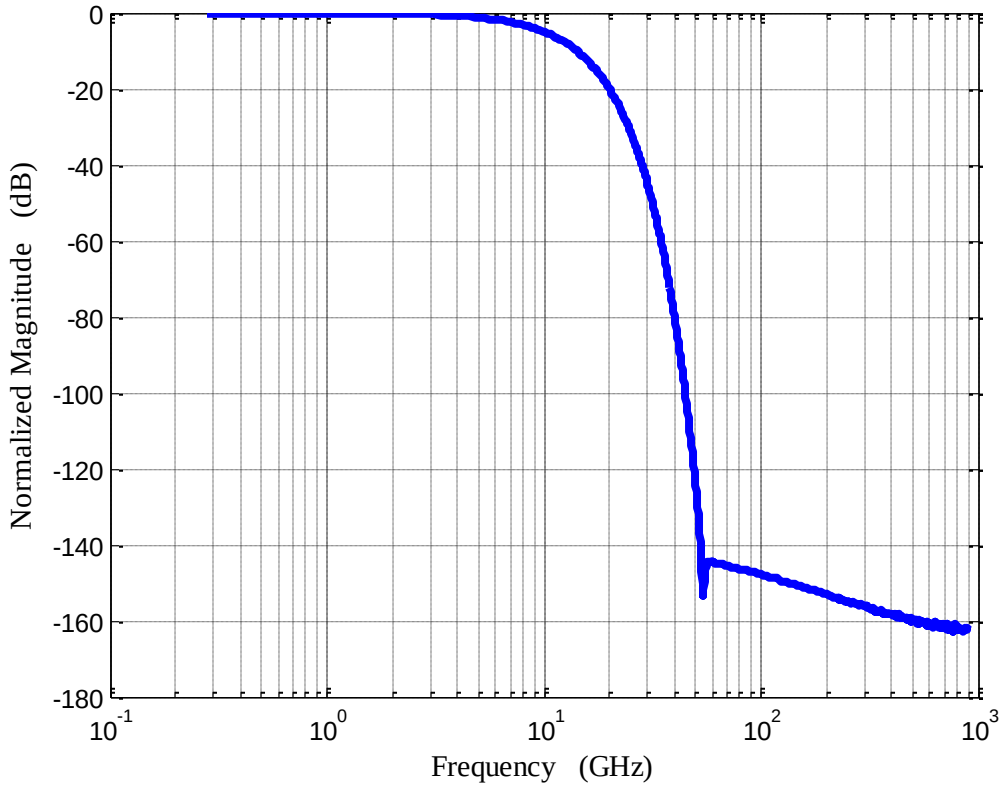

Figure 3.5. Normalized excitation spectrum for uniform plane wave models.

Figure 3.5 also shows frequency content up to approximately 900GHz, which is due to a time-step of 0.554psec, using $f_{\max} = \frac{1}{2T_s}$. Despite this large excitation band, the results from CST are generally only reliable up to the maximum frequency set forth by the user. For this reason, the maximum frequency of to be studied in the section will be 20GHz.

Field probes were also placed throughout the models for the purpose of obtaining the necessary data for comparison with (2.56) and (2.58), and also for checking that

certain criteria were met to ensure reliable results. On the scattering side of the arrays, where $x > 0$, field probes were placed for E_x, E_y, E_z, H_x, H_y, and H_z at (399mm,101mm,101mm), which is approximately the center of the y-z cross-section of the array at the edge of the computational domain, shown in Figure 3.1. The information from these probes was used to ensure that the scattered waves reaching the PML ABC were approximately plane waves, which generally coincides with the proper behavior from the ABC. Far-field probes for E_y and H_z were also placed at 3m from the center of the aperture arrays at (3000mm,101mm,101mm). The data from the E_y far-field probe was the source of data used for comparison with (2.56) and (2.58).

3.3 COMPLETE RESULTS FOR A SINGLE UPW SIMULATION

Before going forth and presenting all of the results for the UPW models, this subsection will step the reader through the complete set of results for a single UPW model. The intent of this action is to aid the reader in understanding how certain results were obtained, along with why the soon to be specified frequency band was chosen. To show this same set of work for each individual simulation would be very cumbersome and tedious. For this subsection, the model to be explored has an array of 07x07 elements, L = 3mm, and 1mm spacing between each aperture, where L and aperture spacing were displayed back in Figure 2.11.

The first piece to ensuring that the model functioned correctly is ensuring that the total energy in the system decayed to an acceptable level. Figure 3.6 shows the system energy for the model as a function of time. The first large dip in energy at 1400ps is due to the reflection of the incident wave on the PEC sheet exiting the model from the domain

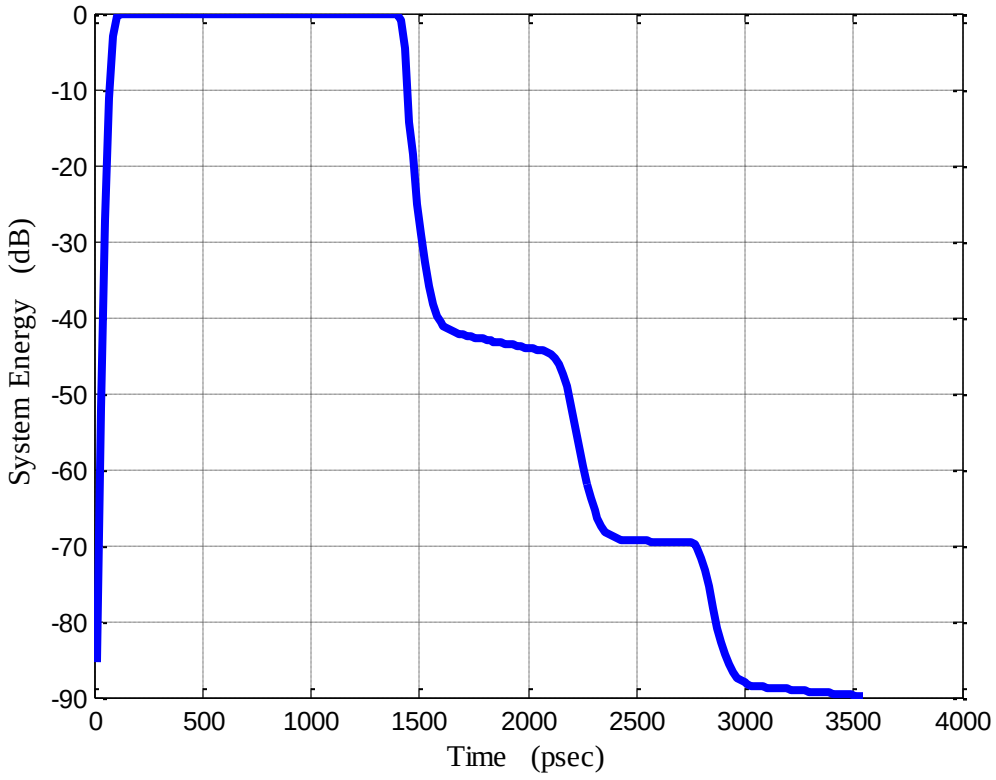

Figure 3.6. System energy for a 7x7 array, L = 3mm, aperture spacing = 1mm.

edge at x = -200mm. The dip at 2100ps is caused by fields that coupled through the array exiting the model at x = 400mm. At this point, the only energy left in the system is from "ringing" in the apertures and from reflections at the domain boundaries due to non-ideal ABCs. A system energy decay of -70dB by 2100ps should yield excellent results from the standpoint of stability and for performing fast Fourier transforms (FFTs), but the total energy decay of -90dB by the end of the simulation is even better.

Knowing that the system energy had decayed sufficiently, the next step is to check the near-field probes at (399,101,101), shown in Figure 3.1, to ensure that the

recorded signals seem feasible. In Figure 3.7, it can be seen in all three plots that the scattered fields do not reach the monitor point until approximately 2000ps, which is consistent with the explanation given for the second energy dip in Figure 3.6, where a large dip in system energy comes just after 2000ps when these scattered fields exit the domain. Figure 3.7 also shows that E_z is the dominant component of the E-field, which is expected, since the incident UPW was polarized in the +z-direction. Similar observations can be made about the plots of the magnetic field at (399,101,101), shown in Figure 3.8. Here, the signal again reaches the monitor points just after 2000ps, and the dominant component of the H-field is H_y, which complies with the definition of the Poynting Vector, $\bar{S} = \bar{E} \times \bar{H}$, where if $\frac{\bar{S}}{|\bar{S}|} = \hat{x}$, and $\frac{\bar{E}}{|\bar{E}|} = \hat{z}$, then $\frac{\bar{H}}{|\bar{H}|} = -\hat{y}$. The 180^o phase shift of the H_y component is seen in Figure 3.8 as the slope of H_y is negative when the slope of E_z in Figure 3.7 is positive.

Another important piece of information to be gathered from the data displayed in Figure 3.7 and 3.8 is the ratio of $\frac{|E_z|}{|H_y|}$. Different ABCs for numerical solvers are similar in the sense that their purpose is to allow electromagnetic waves to "pass" outside of the computational domain uninhibited, as though there were no actual boundaries to the model. Where many types of ABCs will differ is in the algorithm that is used to "pass" these fields without reflection at the boundaries. Some algorithms only work if the incident fields on the boundary are plane waves at normal incidence, while other varieties may claim that any form of wave at any angle of incidence is acceptable, but the algorithm for such claims may be very complex and resource consuming. To ensure that

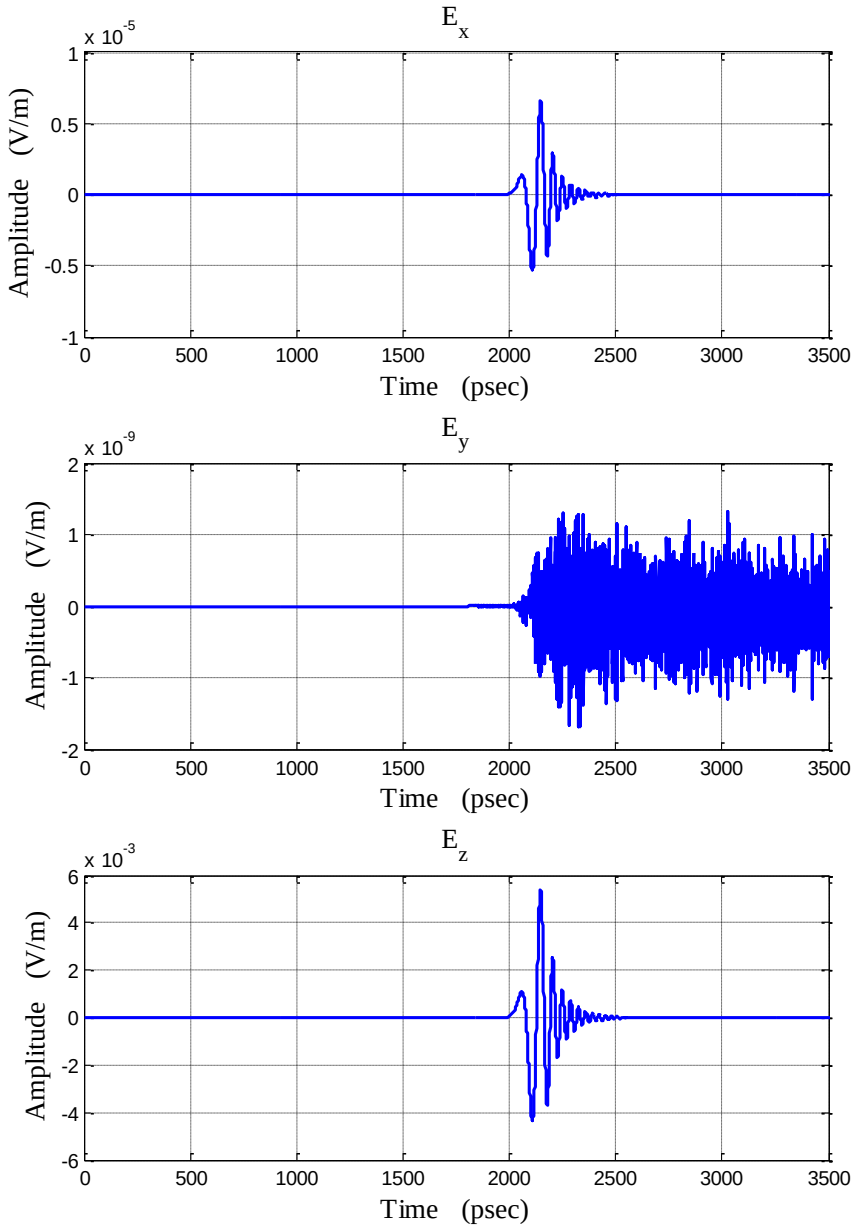

Figure 3.7. Electric near-field probes at the edge of the domain at (399,101,101).

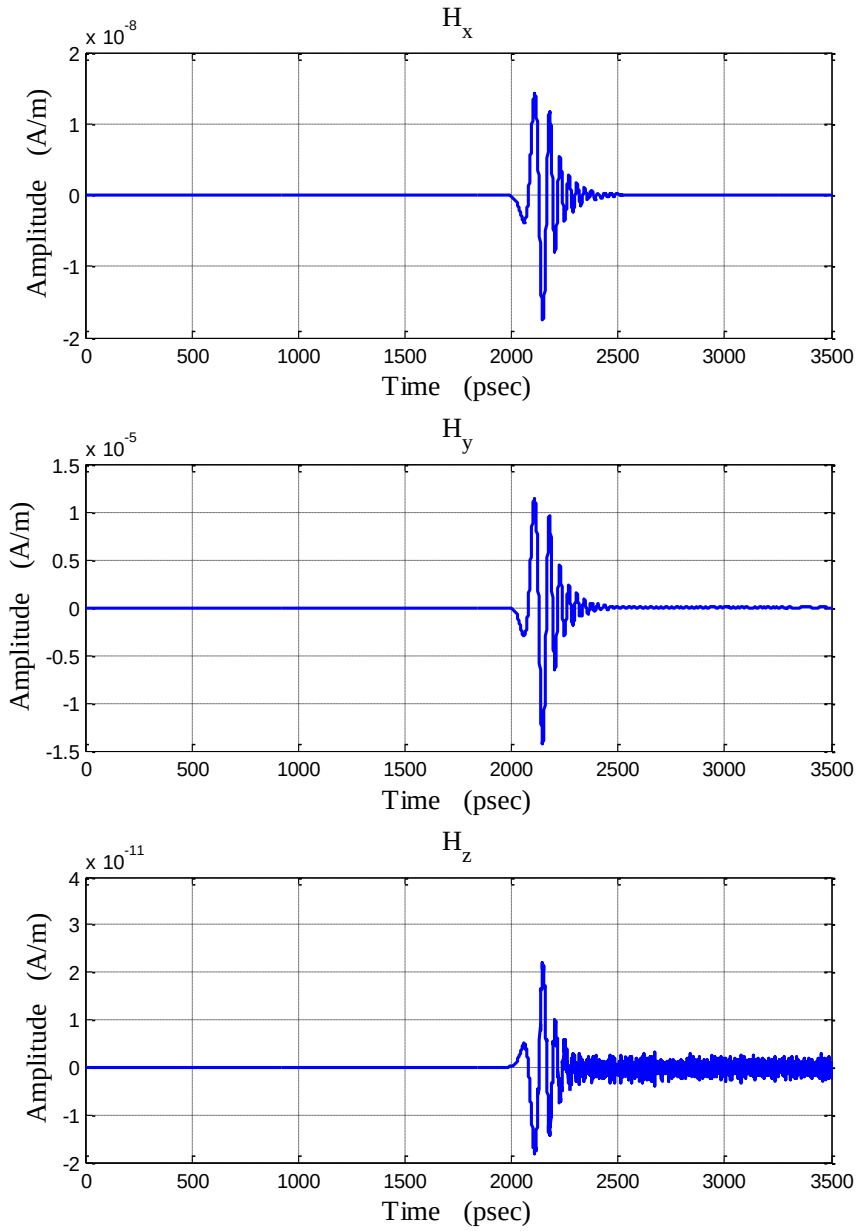

Figure 3.8. Magnetic near-field probes at the edge of the domain at (399,101,101).

minimal reflections occur at the boundary on the scattering side of the array, where x > 0, and that the data used during post-processing by CST to calculate the far-fields at 3m is reliable, the fields at (399,101,101) need to be checked to make sure they are meeting the criteria of plane waves.

One characteristic of plane waves is that the ratio between the E-field and the H-field is 120π. Figure 3.9 shows the dominant E-field magnitude, $|E_z|$, divided by the dominant H-field magnitude, $|H_y|$. From visual inspection, the reader can see that from

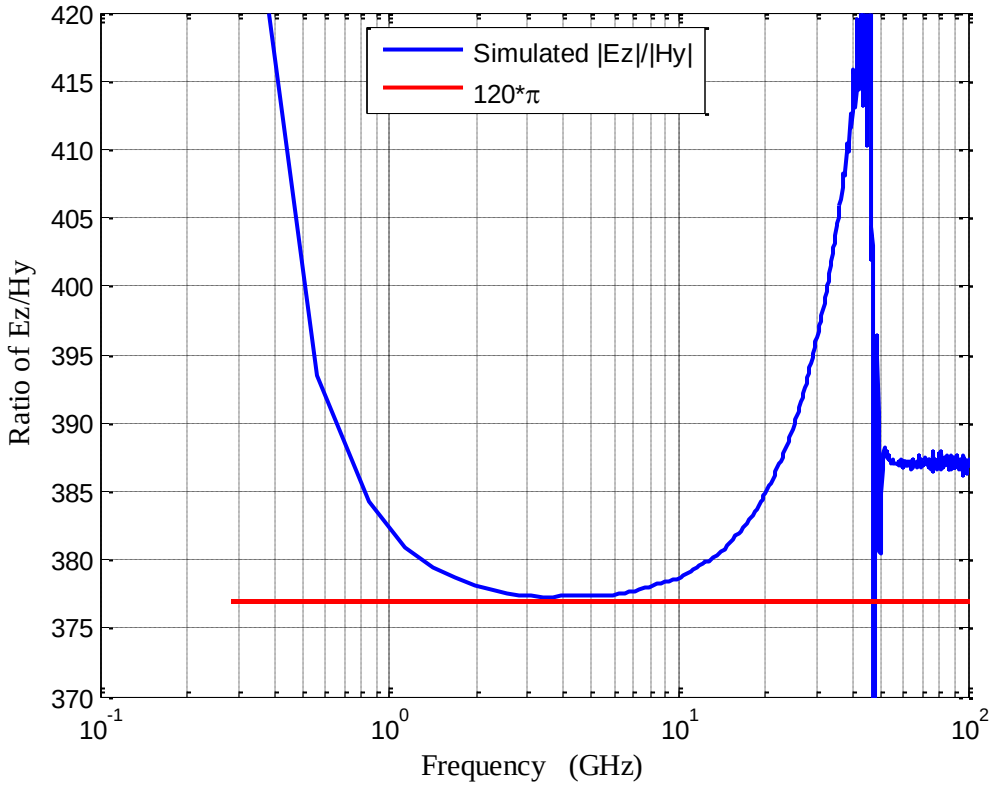

Figure 3.9. Ratio of $|E_z|/|H_y|$ from the field probe at (399,101,101).

1GHz to 20GHz, the ratio the fields is between 377 and 385, which is an acceptable amount of error in having confidence in the far-fields computed from these results. Figure 3.10 shows the corresponding phase of E_z and H_y, with an extra 180^o being added to H_y to aid in the comparison. This shows that E_z and H_y are 180^o out of phase, with the 180^o shift being accounted for in the Poynting Vector discussion above.

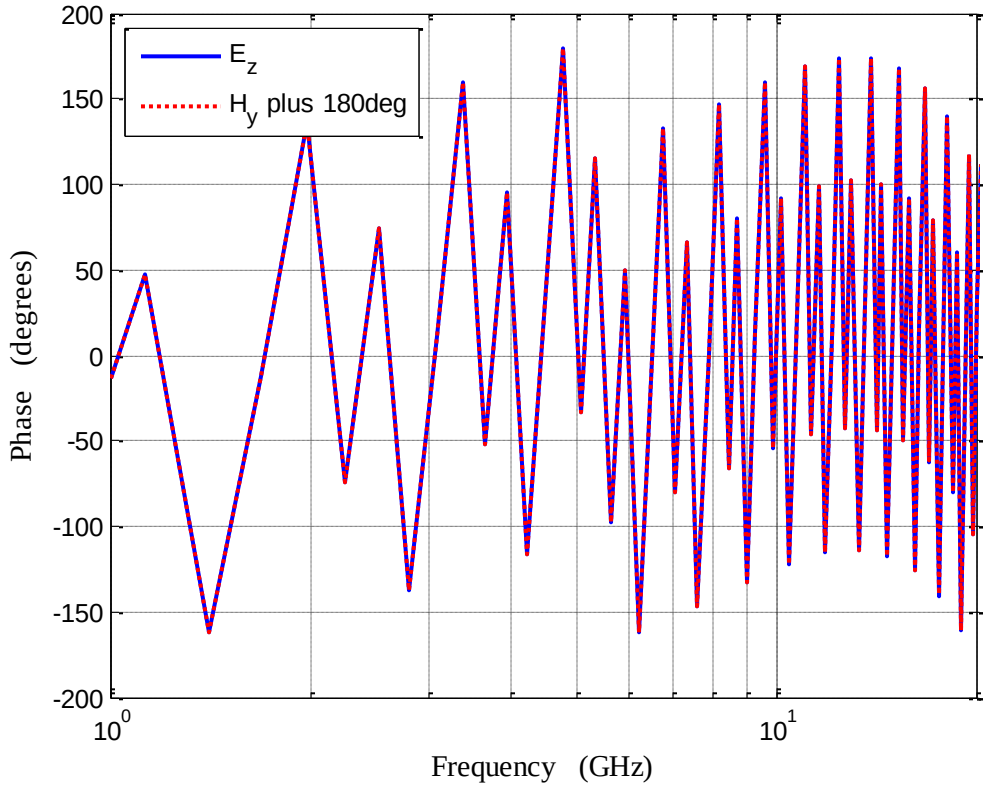

Figure 3.10. Phase of E_z and H_y at (399,101,101).

With all important factors inside the computational domain having been discussed and verified to be acceptable, the next thing to look at is the far-field data computed by CST during post-processing. Figure 3.11 shows the time-domain signals of E_z and H_y, the dominant components of the E- and H-fields, from the far-field monitor at

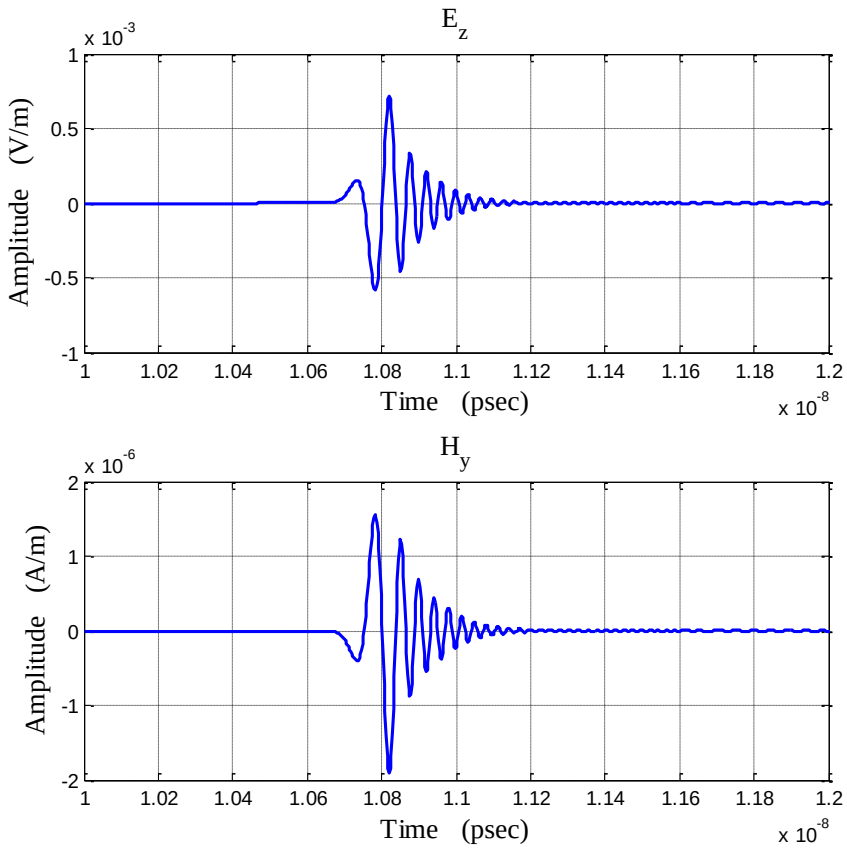

Figure 3.11. E_z and H_y time-domain signals from the far-field probes at (3000,101,101).

(3000,101,101). As these field probes were 3m from the aperture array, and the excitation is at x=-0.2m, the anticipated time-delay is $\frac{3.2m}{3e8\,{}^{m}/_{s}} = 10.67ns$, which corresponds with the time-delay from the simulation results in Figure 3.11. Taking the FFT of both E_z and H_y, shown in Figure 3.12, the reader can see that there is constant 51.5dB difference between both components. This is expected, as these components should represent an approximate plane wave, and the ratio between the electric and magnetic field components for a plane

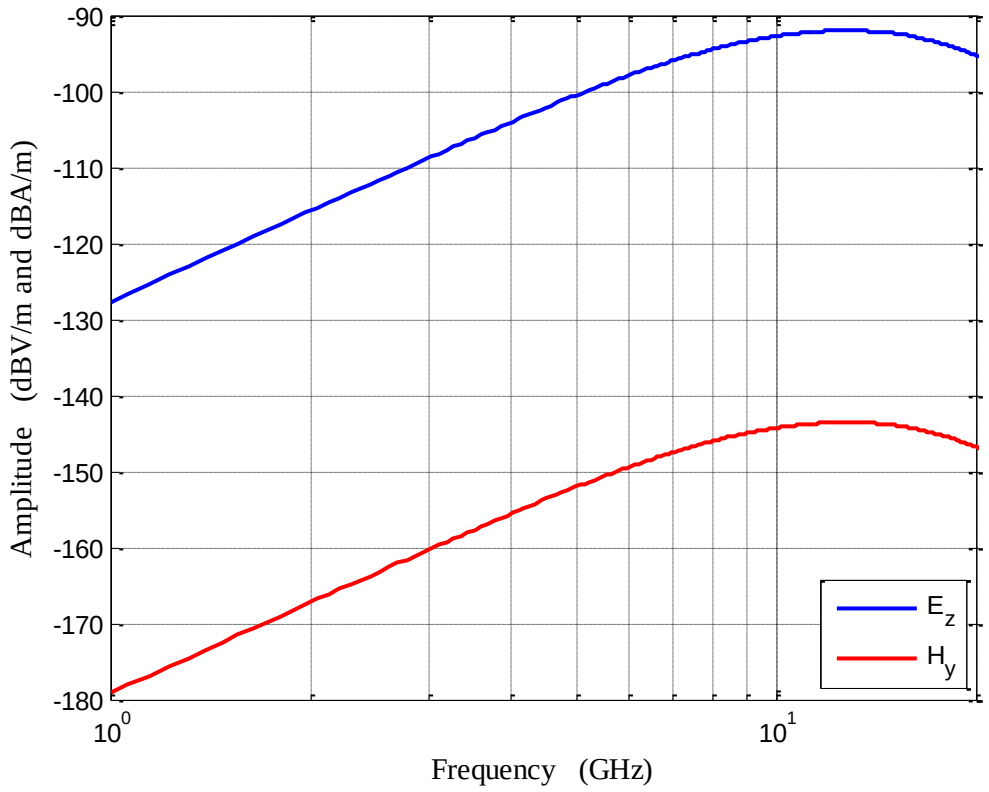

Figure 3.12. Un-normalized magnitude spectra of E_z and H_y at (3000,101,101).

wave is 120π, or 51.5dB. The phase spectra of E_z and H_y at this monitor point are shown in Figure 3.13, where an extra 180^o has again been added to H_y to aid in the comparison.

Figure 3.14 again shows the magnitude spectra of E_z and H_y, but this time normalized to the excitation spectrum, along with the E-field approximation from (2.56). As one of the unique traits of a UPW is that the wave does not suffer from any sort of $\frac{1}{r^n}$ decay factor, the magnitude spectrum at the far-field monitor point at (3000,101,101), in the absence of the PEC sheet, would be the same as the excitation/incident magnitude

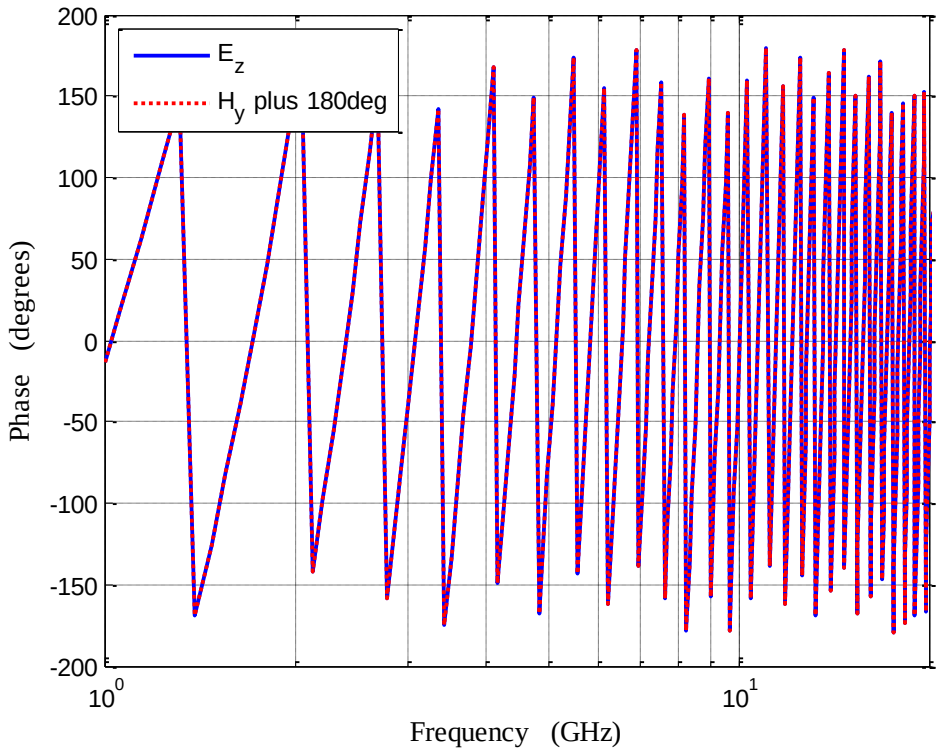

Figure 3.13. Phase Spectra of E_z and H_y at (3000,101,101).

spectrum. For this reason, the excitation magnitude spectrum can be used as the "Electric Field Intensity with No Shielding Mechanism" term in the SE definition from (2.30). Similarly, the E_z data from the far-field probe that is scattered by the aperture array can be used as the "Electric Field Intensity with Shielding Mechanism" term in (2.30). With the terms of (2.30) identified, the simulated shielding effectiveness can be found, which is shown in Figure 3.15. The error between the simulation result and (2.58) is shown in Figure 3.16, where the positive error indicates that (2.58) has under-estimated the SE of

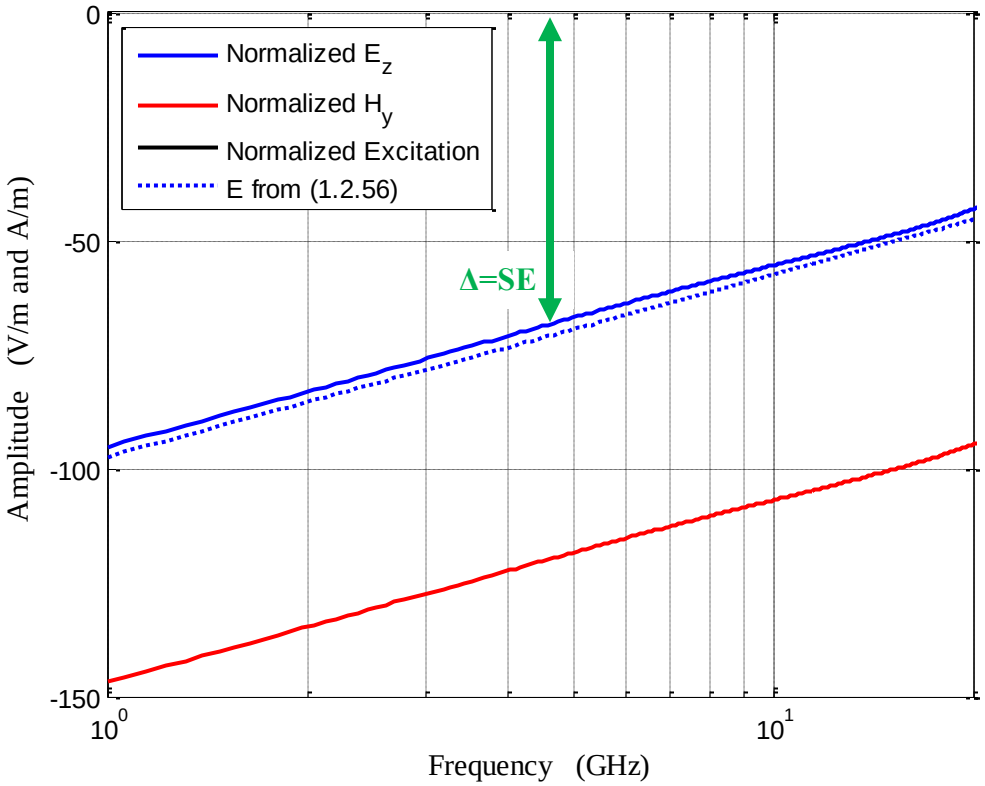

Figure 3.14. Normalized excitation, E_z, H_y, and visual definition of shielding effectiveness.

the aperture array. Two definite contributing sources to the error shown in Figure 3.16 are the mutual coupling factor and the differing distance between each aperture and the observation point at (3000,101,101).

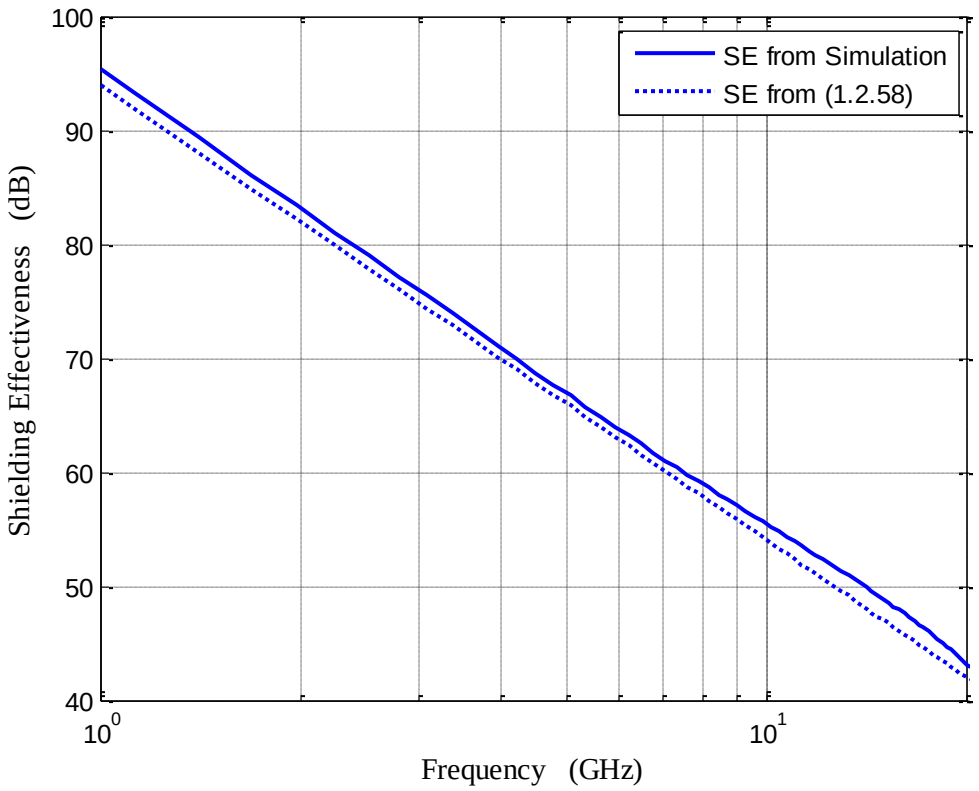

Figure 3.15. Shielding effectiveness results from both CST simulation and (2.58).

The mutual coupling, which was explained in Section 2.6, is a worst-case estimate of how the radiated field intensity changes when multiple apertures are in close proximity to one another. By adding the mutual coupling term, MC_{dB}, into (2.58), the assumption is

made that the radiation intensity from every aperture in the array is affected the same way, which is not the case.

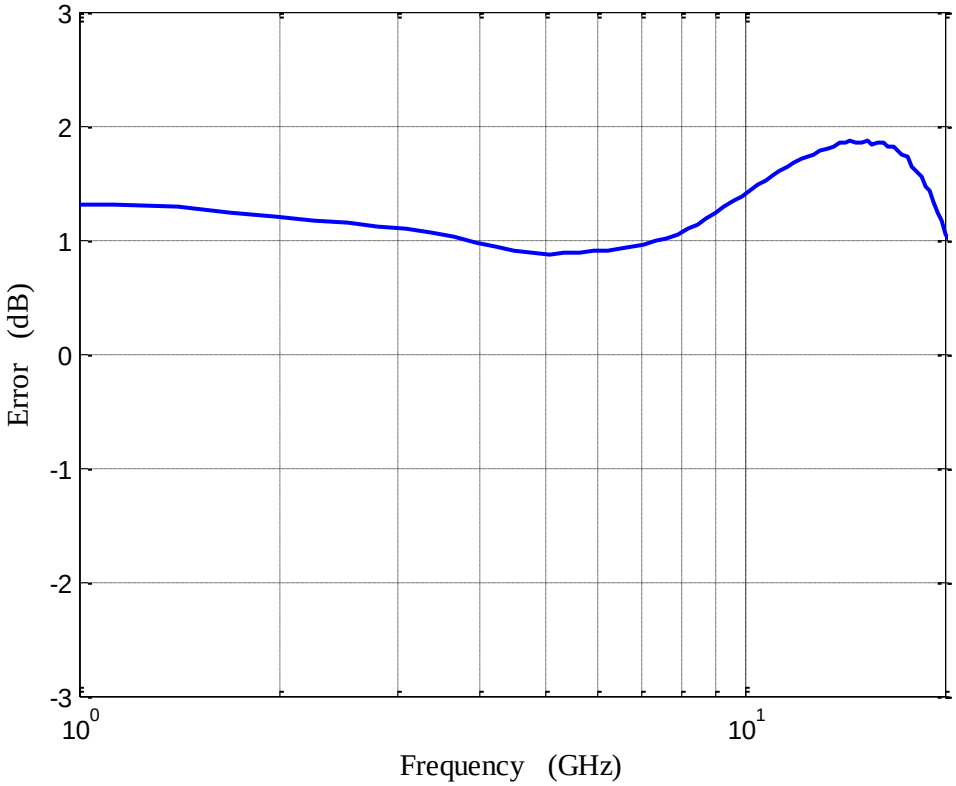

Figure 3.16. Difference between simulation SE result and (2.58).

As for the differing distance from each aperture to the monitor point, the largest error from any model studied in this section, as shown in Table 3.1, would be from the 21x21 array, and would yield a magnitude difference of

$$\frac{3}{\sqrt{\left[\sqrt{2}\left(10\left(0.003\right)+10\left(0.001\right)\right)\right]^2+3^2}}=\frac{3}{3.000533}=0.9998$$

and a maximum phase difference of

$$\frac{e^{-j\frac{2\pi(20e9)}{3e8}(3)}}{e^{-j\frac{2\pi(20e9)}{3e8}(3.000533)}}=1256.63-1256.86=-0.23rad=-13.2^o$$

The results above show that the error introduced by differing distances between each aperture and the monitor point at (3000,101,101) is minimal, and will be ignored for the rest of this section.

With the full analysis of a single simulation complete, the reader should now understand the process used by the author to arrive at the results in this section, and also for the rest of the section. From this point, this only results to be discussed from each simulation will be SE, as this tedious procedure of processing numerous signals for a single simulation will not be shown again.

3.4 RESULTS FOR ALL UPW SIMULATIONS

Unless otherwise noted, all solid curves shown in the plots for the following section represent results from numerical simulations, while the dotted curves of the same color represent the SE prediction from (2.58).

3.4.1 Results for Testing N. As shown back in Table 3.1, the simulations for testing the N term in (2.58) involve several models with identical aperture sizes and aperture spacing, but varying numbers of apertures in each array. Figure 3.17 shows the SE results for the aforementioned models, along with the SE predictions for each array

from (2.58). Note that the slope of both the approximations and simulation results are -40dB/dec, indicating that the f^2 term from (2.58) seems to fit.

There is a small amount of error of approximately 1dB between each simulation result and the corresponding prediction at lower frequencies, with the error increasing past 10GHz. Figure 3.18 shows a plot of the difference between each simulation result and the prediction for SE by (2.58). Figure 3.18 clearly shows that below 10GHz,

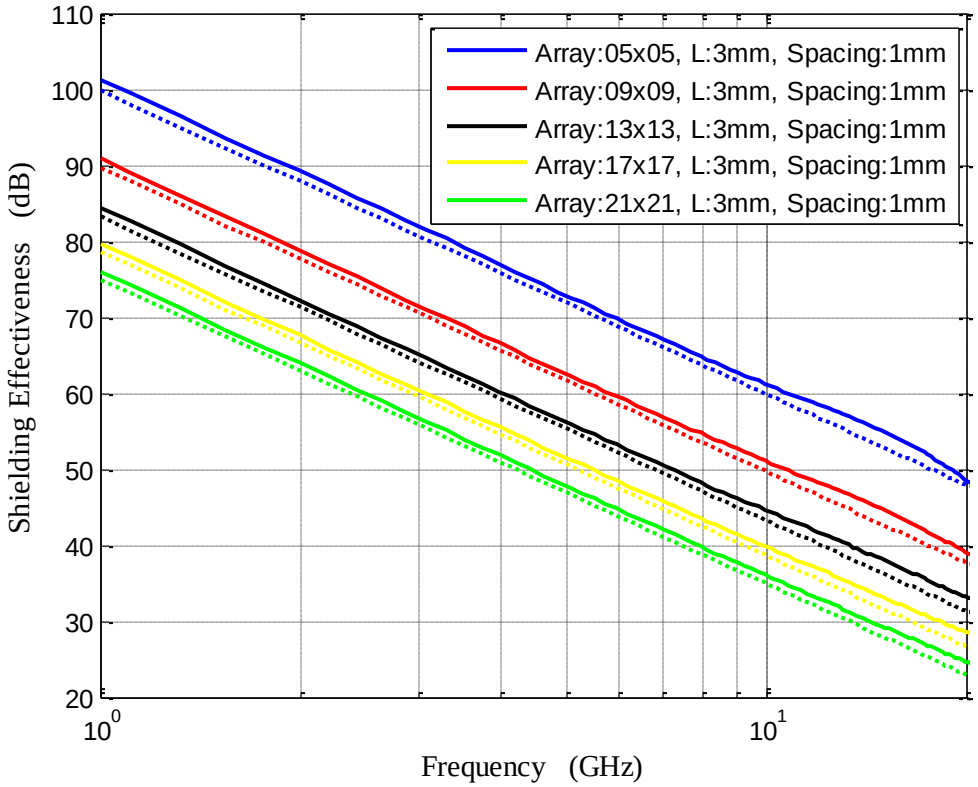

Figure 3.17. Shielding effectiveness results from simulations for testing the N term in (2.58).

the error between the simulation and (2.58) is less than 1.5dB, with a peak error of about 2.1dB at 15GHz, which is just shy of when the aperture dimension, L, is λ/6. An interesting observation is that the peak in error around 15GHz for the 5x5 model is delayed further up the spectrum as the number of apertures in the array increases. This could potentially be caused by the interaction between adjacent apertures, and will be investigated and discussed more in the mutual coupling section. As 2dB is an acceptable amount of error, these simulation results show that (2.58) is indeed dependent on the

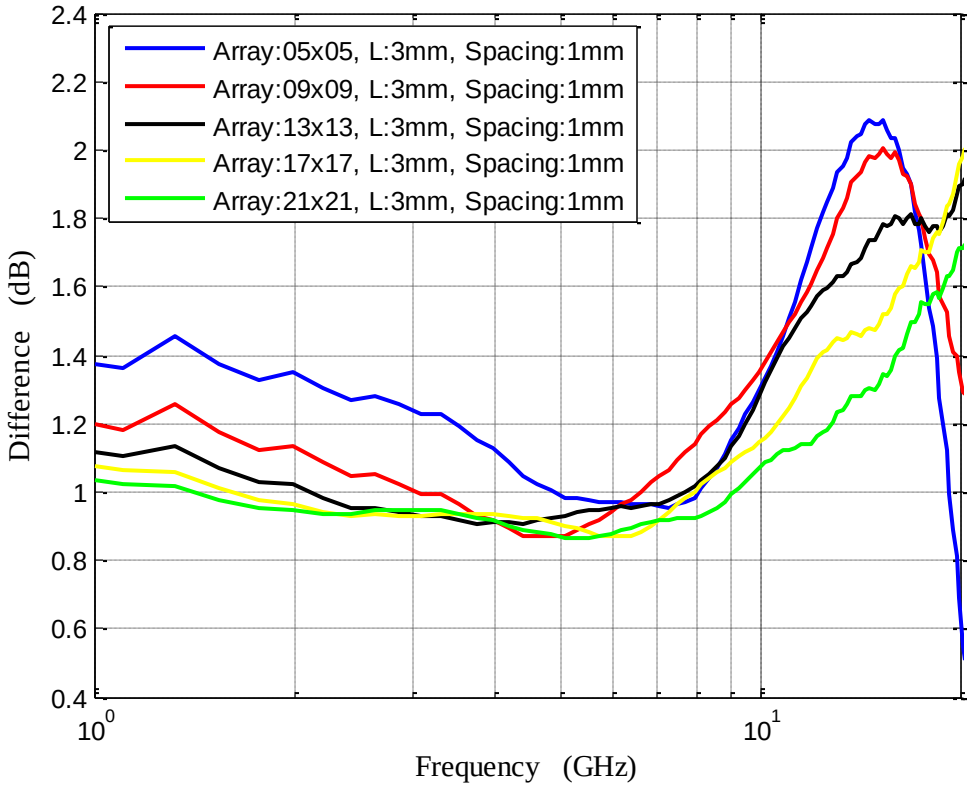

Figure 3.18. Simulation SE results less the prediction from (2.58) for testing N.

number of apertures, N, by $20\log_{10}(N)$. The only potential limitation to this dependence on N could be while the aperture dimension, L, remains less than λ/6, but the results seen here do not provide enough evidence to support this claim.

3.4.2 Results for Testing MC. Back in Section 2.6, the mutual coupling (MC) between closely spaced apertures was examined, but the results that were taken from these simulations were based on the tangential component of the electric field in the middle of the centermost aperture, rather than the radiated field intensity. The results for MC in this subsection are instead derived from the observed far-field intensity for each model, which are based on the radiation from all apertures in the arrays, rather than the fields inside a single aperture.

Figure 3.19 displays the simulation SE results from all models, along with the predicted SE from (2.58). As shown in Table 3.1, all five of the MC simulations consist of a 09x09 array with 3mm apertures, but with different spacing between apertures for each model. Observing (2.58), the reader can see that for a consistent number of apertures and aperture dimensions between models, the only difference in the radiated field intensity should be due to MC between apertures, where (2.54) predicts the increase in radiated field intensity due to the effect of MC. Noting that the ratio of aperture spacing to L in these models ranges from $1/3$ to $5/3$, the largest difference in mutual coupling between simulations should be approximately 2dB, which explains why the results in Figure 3.19 are grouped so closely together, making it difficult to view the results.

Figure 3.20 is a clearer plot than Figure 3.19, as it shows the difference between the simulation SE results and the predicted SE from (2.58). Again, the error is less than

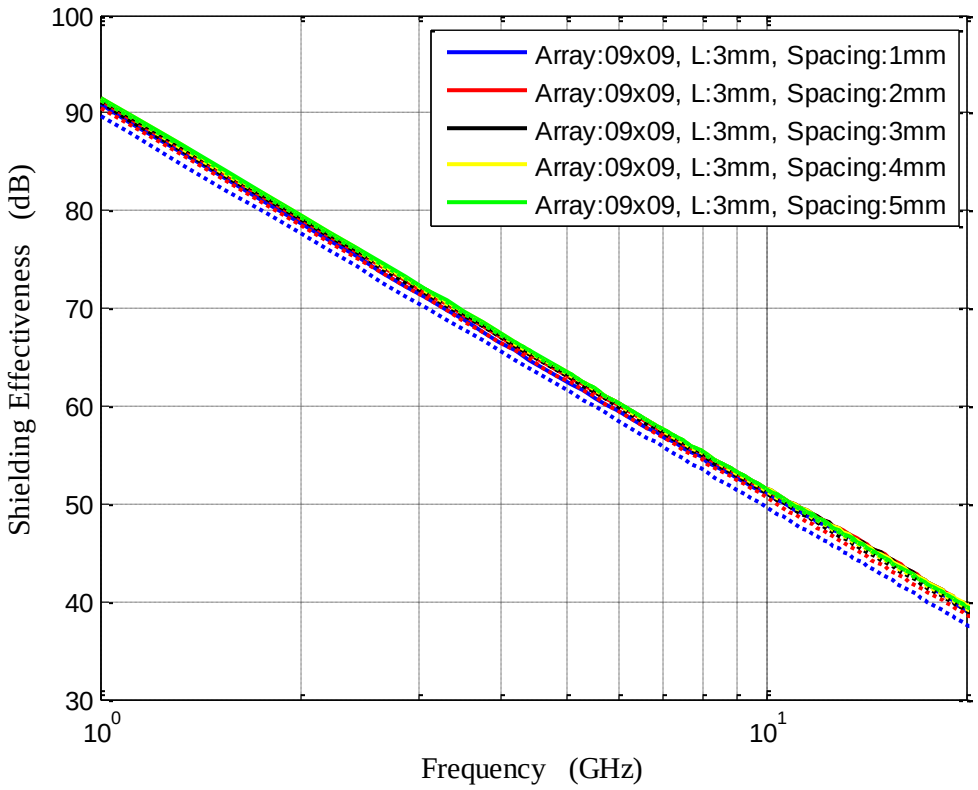

Figure 3.19. Shielding effectiveness results for testing MC.

1.5dB below 10GHz, with the maximum error of 2dB occurring near 16GHz, coinciding with an aperture dimension, L, nearly equal to λ/6.

Another noteworthy observation is that the error shown in Figure 3.20 increases as the spacing between apertures decreases, causing the MC between apertures to increase. Again, when the MC term was found back in Section 2.6 from the tangential electric field in the middle of the centermost aperture in a 09x09 array, that MC term was assumed to be same for every aperture, which is a valid argument for large arrays. Realistically, the impact of MC is strongest on the apertures located in the center of an

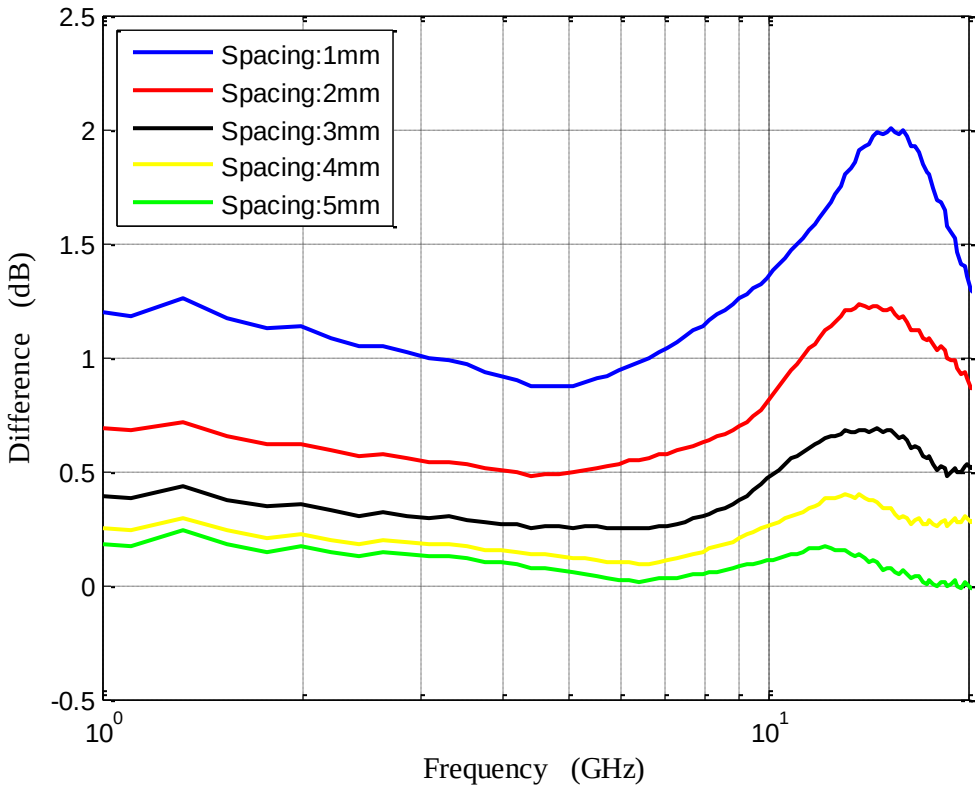

Figure 3.20. Simulation SE results less the prediction from (2.58) for testing MC.

array that have many adjacent neighbors that are also strongly affected by MC, whereas those apertures along the perimeter, having less adjacent neighbors that are strongly affected by MC, are ultimately less impacted by MC. This argument is the most plausible explanation for why the error in Figure 3.18 for the N simulations decreases as the number of apertures increases.

As the spacing between apertures increases, decreasing MC, the error in Figure 3.20 also decreases. For a fixed number of apertures with varying spacing, such as the simulations conducted in this section, the distribution of aperture susceptibility to MC,

described in the previous paragraph, is still a valid argument. However, as the severity of the impact that MC has on aperture radiation lessens with increasing space, so does the relative difference between individual aperture contributions to the far-fields, which decreases the overall error between the simulations and (2.58).

In summary, the MC simulations again show that the error between simulation results and (2.58) is less than 2dB, with a noticeable amount of increased error occurring as the aperture dimension, L, approaches λ/6.

3.4.3 Results for Testing L. Before performing simulations with a fixed number of apertures and aperture spacing, but with different aperture sizes, three models were simulated with a single aperture of L = 3mm, 6mm, and 9mm in each model. By running simulations with only a single aperture, the influence of the number of apertures and mutual coupling can be removed, and the results should ideally reflect only the influence of the aperture size.

Figure 3.21 shows the results from the single aperture simulations, along with the corresponding approximations using (2.58), while Figure 3.22 displays the difference between the simulation results and (2.58). From Figure 3.22, it can be seen that the error between the 3mm simulation and the corresponding prediction is nearly 0dB at low frequencies, while when the aperture dimension, L, becomes greater than λ/6, the error begins to rapidly increase. For both the 6mm and 9mm apertures, the low frequency error is about -1.5dB, but rapidly changes as the aperture dimensions increase to λ/6 at 8.3GHz for the 6mm aperture and 5.6GHz for the 9mm aperture. Noting that the error between the simulation results and the corresponding SE predictions from (2.58) is a worst-case of

3dB as L approaches λ/6 for all three models, increasing rapidly thereafter, these simulations suggest that a limitation of L < λ/6 be placed on (2.58).

To test the L term in models with multiple apertures, Table 3.1 shows that three more simulations were run, each consisting of a 07x07 array, with a spacing of 1mm for L = 3mm, a spacing of 2mm for L = 6mm, and a spacing of 3mm for L = 9mm. The

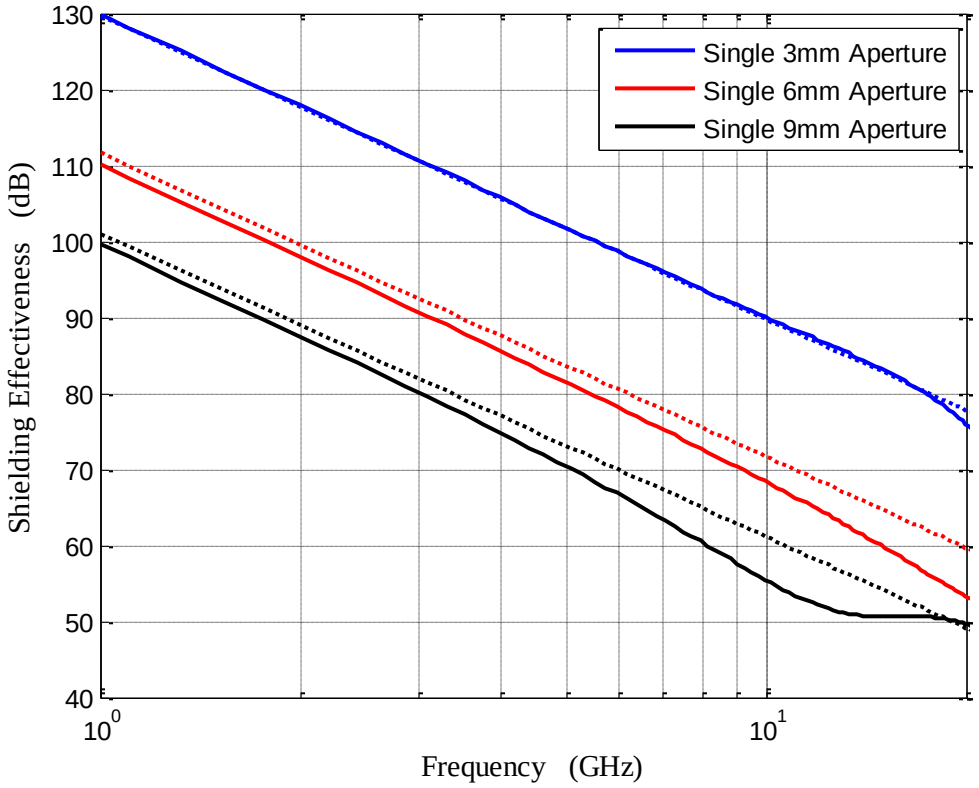

Figure 3.21. Shielding effectiveness results of single apertures for testing L.

aperture spacing for each of these models was done in this way to keep the MC term the same between models. The simulation SE results for each model, along with the corresponding prediction by (2.58), are shown in Figure 3.23, with the difference between each simulation prediction shown in Figure 3.24.

Observing Figure 3.24, it can be seen that over the entire frequency band, the error between the simulation results and (2.58) is less than 2dB, as opposed to the data shown in Figure 3.22, which suggests that the error can be kept to within 3dB,

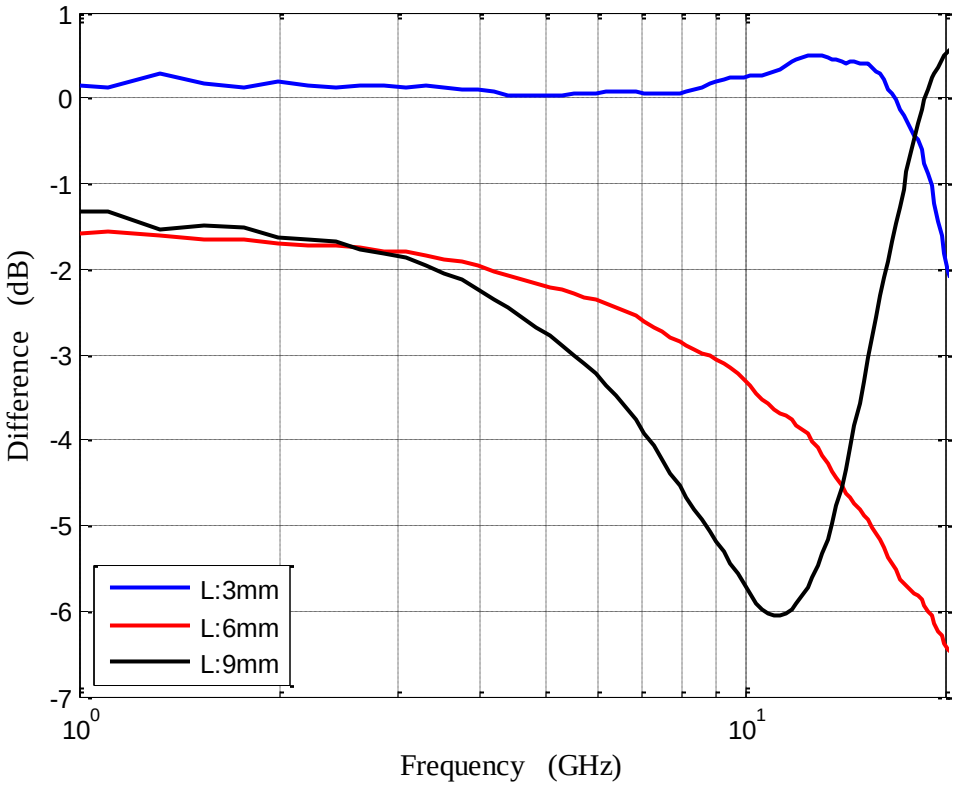

Figure 3.22. Simulation SE results less the prediction from (2.58) for the single apertures for the testing of L.

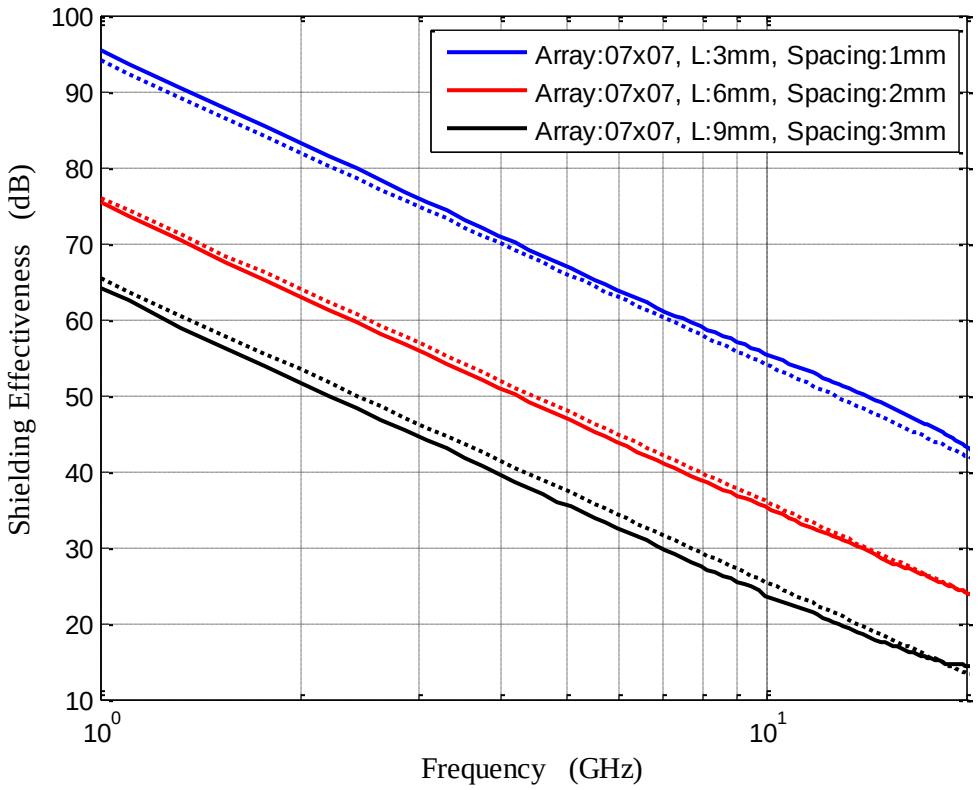

Figure 3.23. Shielding effectiveness results of arrays for testing L.

so long as L is less than λ/6. It is surprising that the decrease in SE in Figure 3.22 when L approaches λ/6 is not present in data shown in Figure 3.24. One possible explanation for this lack of error is the interaction between the apertures in the array. Looking back at Figure 3.20 for the MC study, it can be seen that when the L ≈ λ/6, the SE actually increases by a few dB for the arrays (as suggested by the positive error), while the SE decreases for the single apertures when L ≈ λ/6. As has been noted several times throughout this thesis, the physics of mutual coupling between apertures is difficult to predict and understand, but it seems as though the interaction between apertures in an

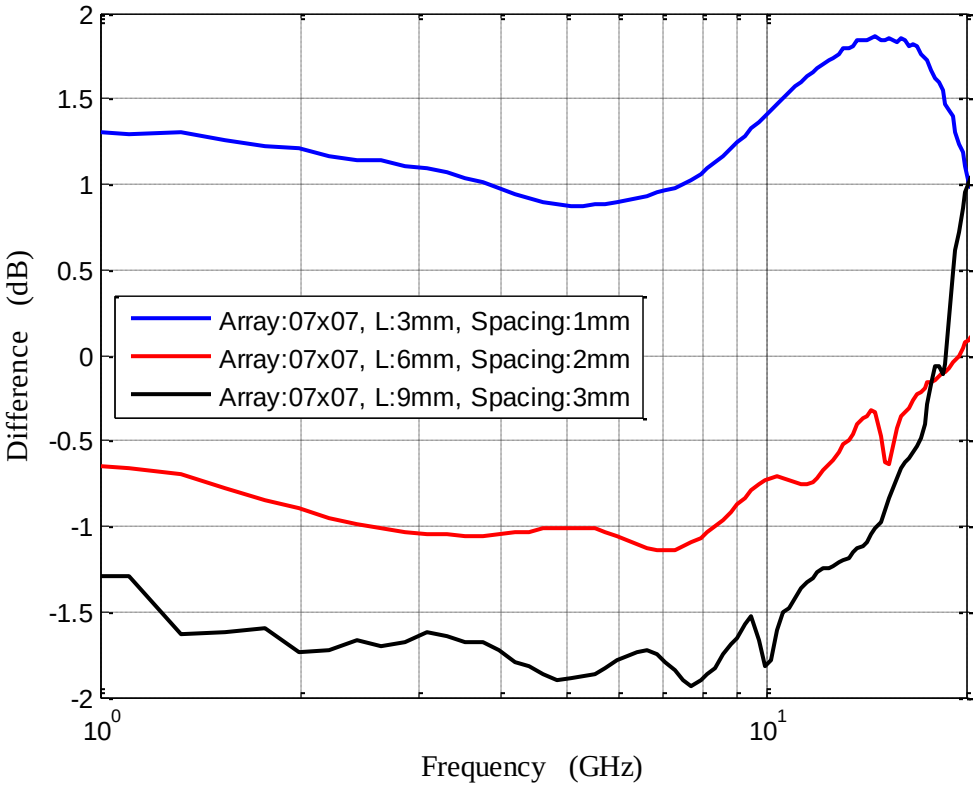

Figure 3.24. Simulation SE results less the prediction from (2.58) for the array models apertures for testing L.

array seems to decrease SE at low frequencies, but improve SE, to some degree, when L becomes greater than λ/6.

The results from the L study have shown that for a single aperture, the error between simulation results and (2.58) is less than 3dB, while the aperture size, L, remains less than λ/6. However, simulations were conducted with multiple apertures in an array, the findings suggested that the error between simulation results and (2.58) is within 2dB,

and that no upper frequency limit could be deduced within the observed frequency band from 1GHz to 20GHz.

3.5 SUMMARY OF RESULTS FOR UPW SIMULATIONS

The purpose of the UPW simulations was to create a simple scenario to investigate before conducting the enclosure simulations, which are of more practical use, but more difficult to understand. These models were all excited by a uniform plane wave at normal incidence to the aperture arrays, which were placed in an infinite sheet of PEC with zero thickness. In doing so, the arrays for all models were excited with uniform amplitude and phase, which is considered to be the worst-case EMI scenario for coupled fields to constructively add up at the observation point, located at 3m normal to the center of the aperture arrays.

For the N simulations, the error between the simulation results and (2.58) was approximately < 2dB over most of the observed frequency band of 1GHz to 20GHz, with the error decreasing between models as the number of apertures, N, increased. The maximum observed error, 2.1dB, occurred when $L \approx \lambda/6$.

For the MC simulations, the error between the simulation results and (2.58) was ≤ 2dB over the entire observed frequency range. The maximum observed error of 2dB occurred when $L \approx \lambda/6$.

For the L simulations, the simulation results for the single aperture models resulted in an error of ≤ 3dB, while $L < \lambda/6$. However, when the L study was conducted with multiple apertures in an array, the observed error was < 2dB over the entire observed frequency range. This finding suggests that while the MC between apertures in an array

causes an increased radiated field intensity at lower frequencies, the effect of MC actually tends to cancel out the increase in radiated field intensity caused by the apertures becoming electrically large, to a certain extent.

Being conservative, the data presented in this section suggests that the prediction for the SE of an aperture array in an infinite PEC sheet of zero thickness, given by (2.58), is accurate to within 3dB, while $L < \lambda/6$.

4 ENCLOSURE SIMULATIONS

The results from the UPW simulations in Section 3 showed that when an aperture array in an infinite sheet of PEC is excited by a UPW at normal incidence, the SE predictions from (2.56) and (2.58) work to within 3dB while $L < \lambda/6$. While these simulations are useful in understanding the physics of the fields scattered by small apertures, the UPW simulations are too unique and unrealistic in the way they are conducted to be of any direct use to the problems this research aims to solve. With a solid understanding of the results from the previous section, this current section shall focus on simulations where the excitation of an aperture array is by an over-moded cavity.

4.1 FUNDAMENTAL DIFFERENCE BETWEEN INFINITE SHEET AND ENCLOSURE SIMULATIONS

Once again, the purpose of the UPW simulations was to simplify the enclosure models, which are of real interest to this research. While the physics of the UPW simulations are well understood, they do not directly translate to the case where the aperture arrays are excited by an over-moded cavity. This subsection shall address the issue of discussing the fundamental differences between the UPW and enclosure models.

4.1.1 Dipole Excitation. The excitation for the infinite sheet simulations, a uniform plane wave, was chosen instead of a finite source so that the apertures in each model from the previous section could be illuminated with uniform amplitude and phase, effectively producing the worst-case far-field radiated intensity. In order to create an incident wave with uniform amplitude and phase over the apertures without placing a discrete source very far away from the array within the computational domain, a total-

field/scattered-field (TF/SF) scheme, such as that described in [10], is utilized by CST to generate a UPW without compromising the available system resources. A UPW excited in such a way is also unique in that the amplitude of the wave does not suffer from any kind of $\frac{1}{r^n}$ decay, like discrete sources of finite spatial distribution would. In other words, such a UPW would theoretically extend to infinity in the directions traverse to the direction of propagation. Described in Section 3, it is this unique characteristic that made calculating the SE so simple for the UPW simulations.

When performing the enclosure simulations, where the enclosure itself is an object of finite dimensions, it is not possible, nor would it be practical or useful, to excite the enclosure with the same UPW as was used in Section 3. For this reason, an electrically short dipole driven by a voltage source was used as the excitation for the enclosure simulations. With the lumped source element 1mm long, and each PEC post being 5mm long (with zero radius), the length of the dipole was 11mm, making the λ/2 resonant frequency of the dipole approximately 13.6GHz. Figure 4.1 shows a side-view of the dipole meshing, where each mesh cell is 0.5mm x 0.5mm x 0.5mm.

Assuming the dipole is aligned with the z-axis and centered about the origin of the coordinate system shown back in Figure 2.2, the far-field radiation from a small dipole is

$$E_\theta = j\eta \frac{2\pi f I_e l \sin\theta}{4\pi c r} e^{-jkr} \tag{4.1}$$

where $\theta = 90^o$ in the direction of the observation point, so the intensity of the field is proportional to the frequency, f, the excitation current, I_e, the dipole length, l, and the distance from the source, r. With r fixed at 3m and l = 0.011m, only f and I_e remain as

dependent variables for determining the field intensity. The first-degree frequency dependence from f in (4.1) cannot be changed, but since the dipole is being excited by a 1V source, I_e is then dependent on the impedance of the dipole, given as

$$I_e = \frac{V_s}{Z_{ant}} = \left(Z_{ant}\right)^{-1} \tag{4.2}$$

where Z_{ant} is predominately capacitive at frequencies below the λ/2 resonance, meaning that Z_{ant} should decrease at a rate proportional to f^{-1} before this first resonance.

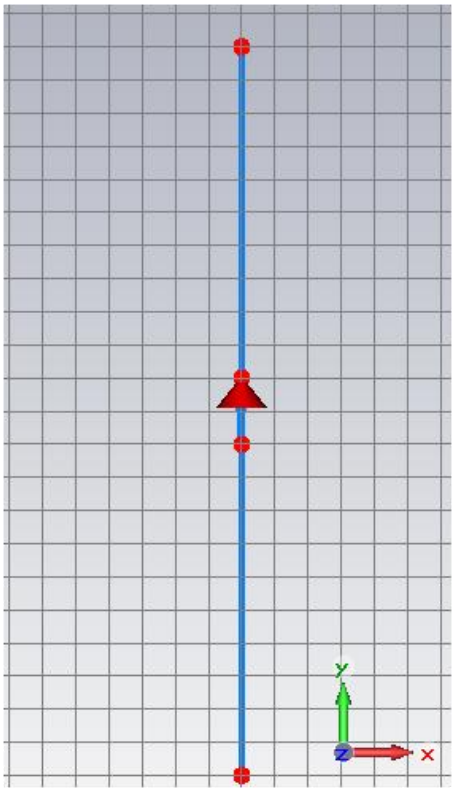

Figure 4.1. Meshing of the dipole source used for exciting the enclosure models.

Rearranging (4.2), it can be shown that when $f << f_{\lambda/2} = 13.6GHz$, I_e is then proportional to f by

$$I_e = \left(\frac{1}{j\omega C_{ant}} \right)^{-1} = 2\pi f C_{ant} \tag{4.3}$$

where C_{ant} is an equivalent antenna capacitance at low frequencies. For a numerical simulation where the dipole is placed in free-space with PML ABCs at the boundaries of the computational domain, Figure 4.2 shows the resulting induced antenna current,

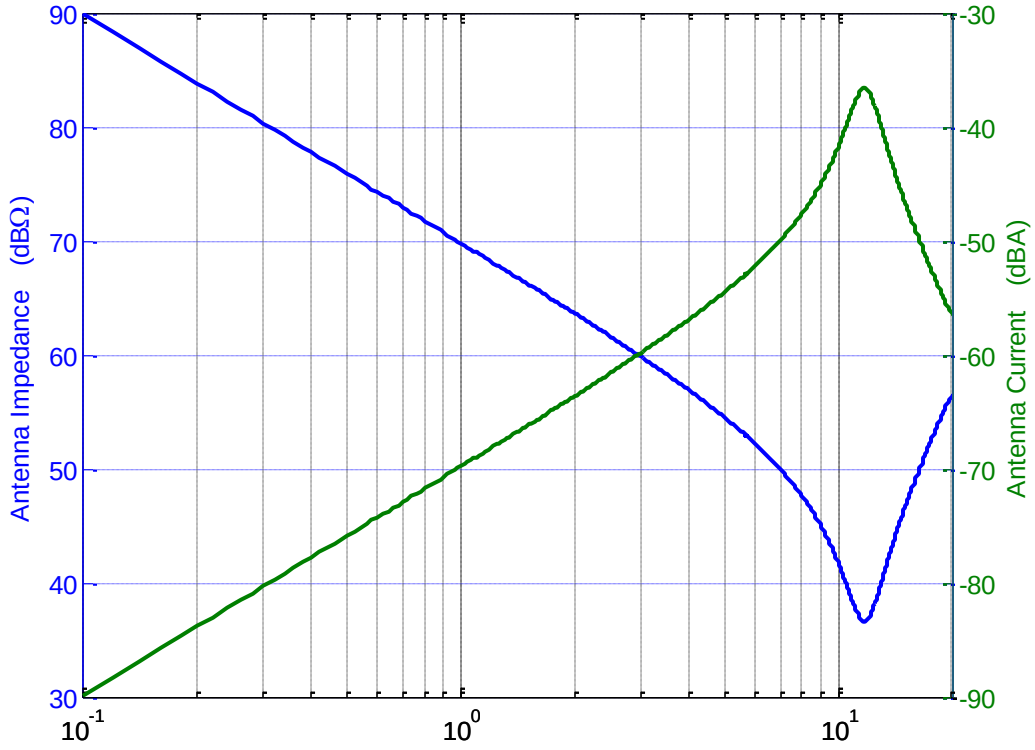

Figure 4.2. Magnitude of the antenna current and impedance for the dipole source used in the enclosure simulations for a source voltage of 1V.

which supports the previous claim that the low frequency impedance of a dipole is predominately capacitive. Knowing that the impressed voltage is 1V, the magnitude of the antenna impedance can be found, as shown in the same plot, with the phase of the antenna impedance given in Figure 4.3. The peak in antenna current, or valley in antenna impedance, marks the $\lambda/2$ resonant frequency of the dipole, which is at 12GHz. The shift from the theoretical frequency of 13.6GHz is likely due to the finite meshing of the antenna.

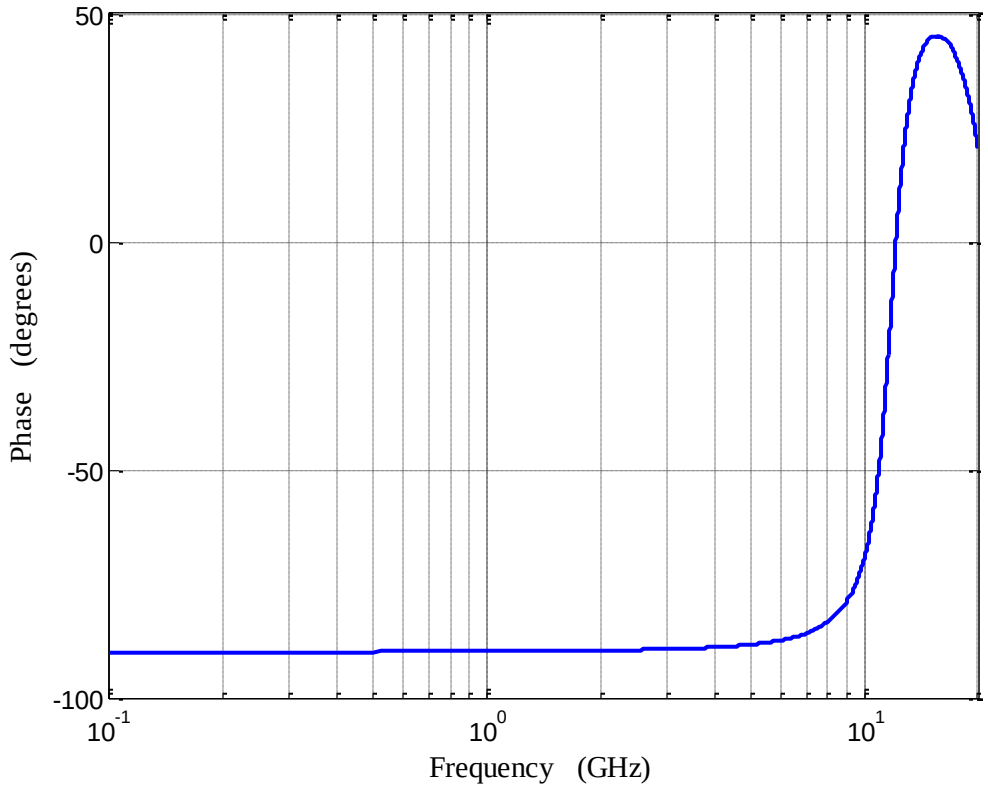

Figure 4.3. Phase of the antenna impedance used for the enclosure simulations.

With the antenna current well-characterized from theory and simulation, this knowledge can then be applied to (4.1) to create an expectation for the far-field radiation from the dipole source. With the native f term in (4.1) and the first-degree f dependence of I_e, the E-field at a point 3m normal to the dipole is expected to increase by +40dB/dec while $f << f_{\lambda/2,sim} = 12GHz$, peaking at the resonant frequency of 12GHz, and then behaving somewhat sporadically after that. Figure 4.4 shows the far-field radiation intensity at 3.05m (3m from the soon to be aperture array) from the

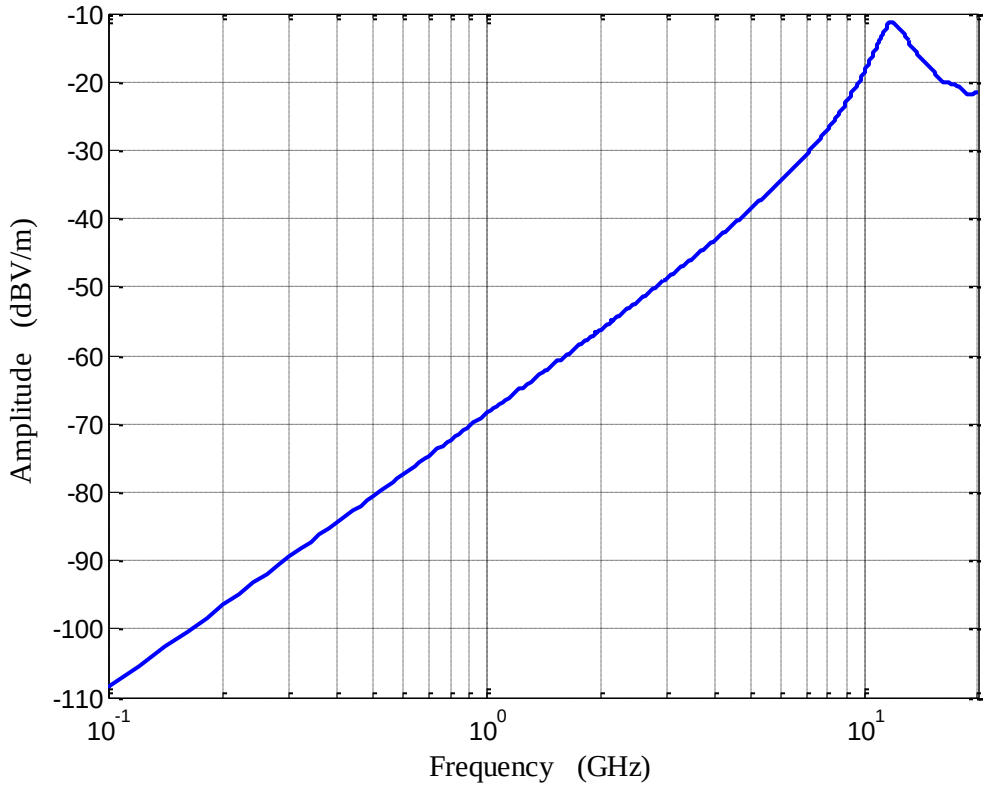

Figure 4.4. Radiated field intensity at a point 3.05m from the dipole source in free-space.

dipole antenna in free-space. As expected, there is a +40dB/dec trend for the observed field strength when the frequency is well below 12GHz. Near 6GHz, deviation from the +40dB/dec slope becomes noticeable, with the peak in field-strength occurring at 12GHz. The data shown in Figure 4.4 will eventually be used in this section to calculate the SE of arrays backed by enclosures, as this data will serve as the "Electric Field Intensity with No Shielding Mechanism" term in the SE definition from (2.30).

4.1.2 Enclosure Q. The enclosure Q is another significant difference between the infinite sheet and enclosure models due to the influence that it has on the radiated fields, as seen in (2.57) and (2.59). In Section 2.5.2, the Q-factor of an enclosure is defined as

$$Q = \frac{\omega W}{P_d} \tag{4.4}$$

where W is the amount of energy stored in the enclosure, and P_d is the amount of energy lost in the enclosure due to either conduction loss, dielectric loss, or radiation loss. The total Q of an enclosure can also be related to the Q caused by each of these three loss factors by

$$Q = \left(\frac{1}{Q_c} + \frac{1}{Q_d} + \frac{1}{Q_r} \right) \tag{4.5}$$

where Q_c is the Q caused by conduction loss in the walls of the enclosure, Q_d is the Q caused by loss in the dielectric of the enclosure, and Q_r is the Q caused by radiation loss from the enclosure. As all metallic objects for the simulations conducted in this study are PEC, the conductivity loss is zero, meaning that the Q_c term in (4.5) does not affect the overall Q of the enclosure.

With no conductor loss, (4.5) can then be reduced to

$$Q = \left(\frac{1}{Q_d} + \frac{1}{Q_r} \right)^{-1} \tag{4.6}$$

The result in (4.6) states that the Q of the enclosure is a function of both dielectric and radiated losses. If no lossy dielectric were to be used to load the enclosure, meaning that the losses from radiation were the only factor influencing the cavity Q, then the Q of the enclosure would be dependent all the factors in (2.57) that contribute to radiation from the apertures. To be complete, the radiation losses would also include the radiation from the equivalent electric polarization current, which has been ignored in this paper, as it does contribute to the far-fields normal to the apertures, but still readily radiates power from each aperture. For this reason, a lossy dielectric is needed to load the enclosure, so as to remove or make the effect of Q_r on the overall Q of the enclosure negligible. In doing so, an obvious limitation would be when Q_r becomes significant to the point of influencing the overall Q in a non-negligible manner.

4.1.3 Resonant Nature of Cavity. The last significant difference between the infinite sheet and enclosure models is the resonant behavior of the enclosure, which was suggested by the influence of the Q-factor in the previous subsection. During the derivation of the aperture excitation in Section 2.5.2, (2.35) showed that the magnetic vector potential, $\overline{A}$, only exists in a significant sense at discrete frequencies, found using

$$k^2 = k_x^2 + k_y^2 + k_z^2$$

$$f_{res} = \frac{c}{2\pi\sqrt{\varepsilon_r}} \sqrt{\left(\frac{m\pi}{a} \right)^2 + \left(\frac{n\pi}{b} \right)^2 + \left(\frac{p\pi}{d} \right)^2} \tag{4.7}$$

where m, n and p must be integers ≥ 0, and a, b and d are the enclosure dimensions. This results shows that rather than having a continuous, well-behaved curve for the simulation SE results, such as those for the infinite sheet models, the simulation results for the enclosure models will have distinct frequencies where the radiated field intensity is significant, corresponding the dips in the SE result. For this reason, the data for the enclosure results will be examined for discrete frequencies, rather than over the continuous band of 1GHz to 20GHz.

4.2 PROPOSED SIMULATION PLAN

An initial batch of simulations were conducted using a simple lossy dielectric inside the enclosure with a constant conductivity of σ = 0.01. By loading the cavity with such a dielectric, Q_d is found by

$$Q_d = \frac{1}{\tan\delta} = \frac{\omega\varepsilon_o\varepsilon_r}{\sigma} = 100\omega\varepsilon_o \tag{4.8}$$

By loading the cavity with a lossy dielectric of σ = 0.01, Q_d becomes a very simple quantity to predict and comprehend. As mentioned in Section 4.1.2, the overall Q of the cavity is defined in (4.6) for PEC walls, where the only dependent variables are Q_d and Q_r. At some point, the power radiated from the apertures will become the dominant loss mechanism in the system, causing the actual Q of the enclosure to stray from Q_d. However, while $P_r << P_d$, where P_r is the power lost to radiation and P_d is power lost in the dielectric, it is an acceptable to assume that $Q \approx Q_d$.

Over the frequency band of 1GHz to 20GHz, the Q of the cavity will be as large as 110, as shown in Figure 4.5. Therefore, the models utilizing the lossy dielectric of σ = 0.01 shall need to consist of few apertures in order to avoid excessive radiated power loss. The advantage of the large Q at high frequencies that is attained using this dielectric is that resonances higher in the spectrum can be observed individually, whereas a lower Q would cause the resonances to blur together.

Table 4.1 shows a list of all simulations that were conducted using the simple lossy dielectric of σ = 0.01. Also included in this list are three simulations where one entire wall of the PEC enclosure is filled with apertures of L = 3mm, 6mm, and 9mm.

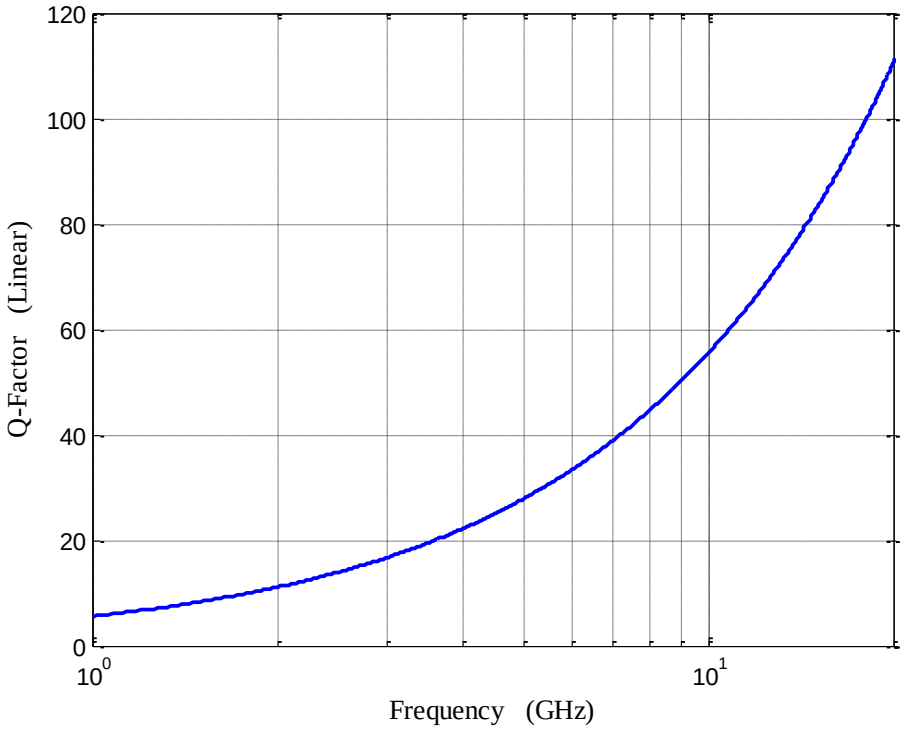

Figure 4.5. Q_d for a lossy dielectric with σ = 0.01.

Table 4.1. Proposed Enclosure Simulation Plan Using a Simple Lossy Dielectric of σ = 0.01S.

Array Size	**Aperture Size**	**Aperture Spacing**
05x05	3mm	1mm
09x09	3mm	1mm
13x13	3mm	1mm
17x17	3mm	1mm
21x21	3mm	1mm
37x27	3mm	1mm
21x15	6mm	1mm
15x11	9mm	1mm

While the simulations with a lossy dielectric of σ = 0.01 are very useful in understanding the physics of the enclosure simulations, these models are not representative of real products that this research is aimed towards, where the loaded Q of such enclosures may only be a maximum of 10. For this reason, a second batch of simulations were run utilizing a lossy dielectric by means of a first-order Debye model, where the value of tanδ is specified to be 0.1 at 20GHz. Figure 4.6 shows ε' for the first-order Debye material, while Figure 4.7 shows ε'' and Figure 4.8 shows Q_d for the same material. Table 4.2 shows the proposed simulations for the first-order Debye models.

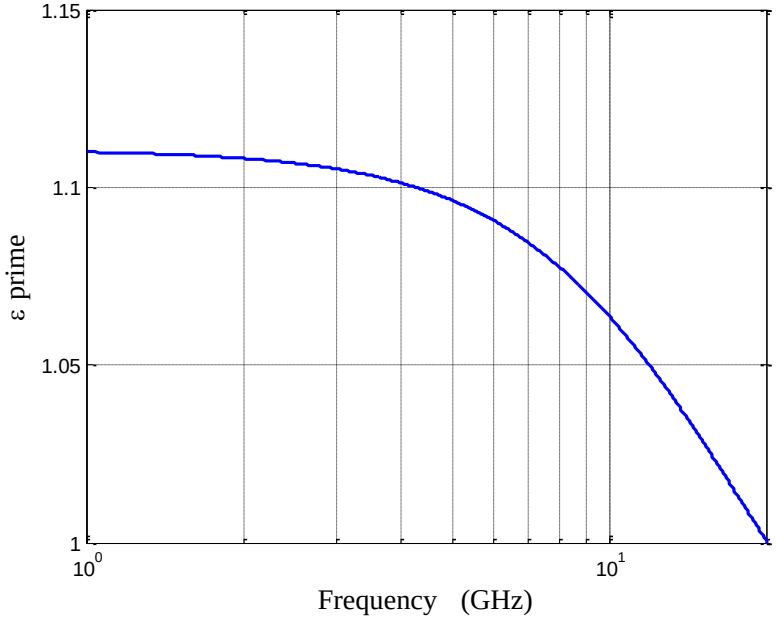

Figure 4.6. Plot of ε' for the first-order Debye dielectric.

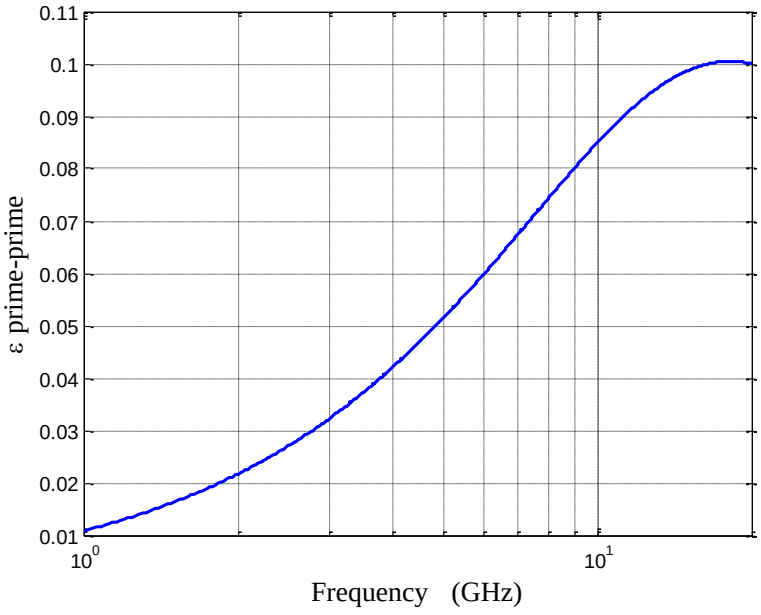

Figure 4.7. Plot of ε'' for the first-order Debye dielectric.

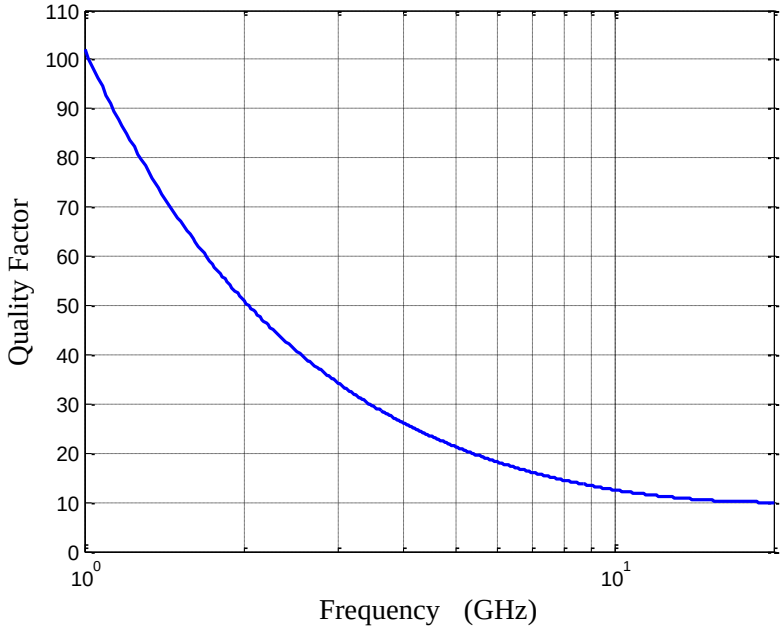

Figure 4.8. Q_d for a first-order Debye dielectric where tanδ = 0.1 at 20GHz.

Table 4.2. Proposed Enclosure Simulation Plan Using a First-Order Debye Dielectric.

Array Size	**Aperture Size**	**Aperture Spacing**
05x05	3mm	1mm
09x09	3mm	1mm
13x13	3mm	1mm
17x17	3mm	1mm
21x21	3mm	1mm
37x27	3mm	1mm

4.3 GENERIC CST MODEL FOR ENCLOSURE SIMULATIONS

Similar to the UPW simulations, each enclosure model studied in this section is a variant of a single generic model. A view of the full three-dimensional computational domain is displayed in Figure 4.9. In this generic model, the enclosure walls have dimensions of 100mm x 115mm x 155mm, and are formed from PEC sheets of zero thickness. The aperture arrays are placed in the wall on the $+\hat{x}$ side of the enclosure, and are centered on this wall, except when noted. PML ABCs are again used in order to prevent reflection of the EM waves within the model at the boundaries of the computational domain, which extend 10mm in the -x-direction, 400mm in the

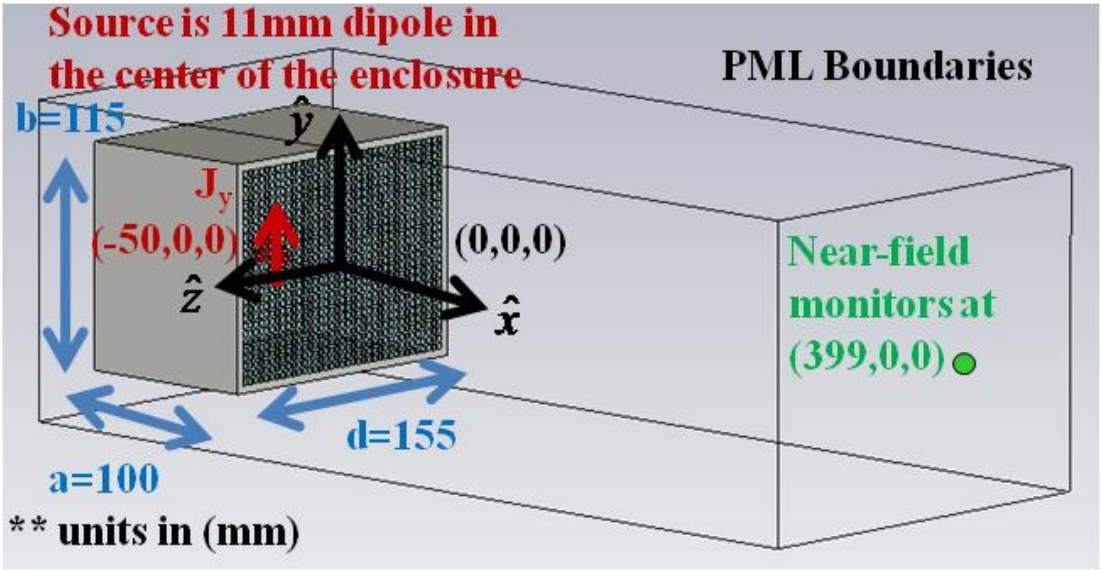

Figure 4.9. Generic CST model used for the enclosure simulations with units of millimetres (mm).

+x-direction, 23mm in the ±y-direction, and 31mm in the ±z-direction, all chosen at the author's discretion. Near-field probes for E_x, E_y, E_z, H_x, H_y, and H_z are placed at (399mm,0,0) to monitor the electric and magnetic fields at the edge of the domain for the same purpose as the UPW simulations. Far-field probes for E_y and H_z are placed at (3000mm,0,0) to monitor the radiated field at 3m normal to the aperture array, and is the source of data from which the simulation SE is found.

Figure 4.10 shows the meshing of the apertures in the y- and z-directional cross-section. While the UPW simulations utilized a mesh of 0.25mm x 0.25mm across the apertures, the enclosure models only use 0.5mm x 0.5mm in order to keep the total number of mesh cells to a reasonable number, which comes to about 44 million. The

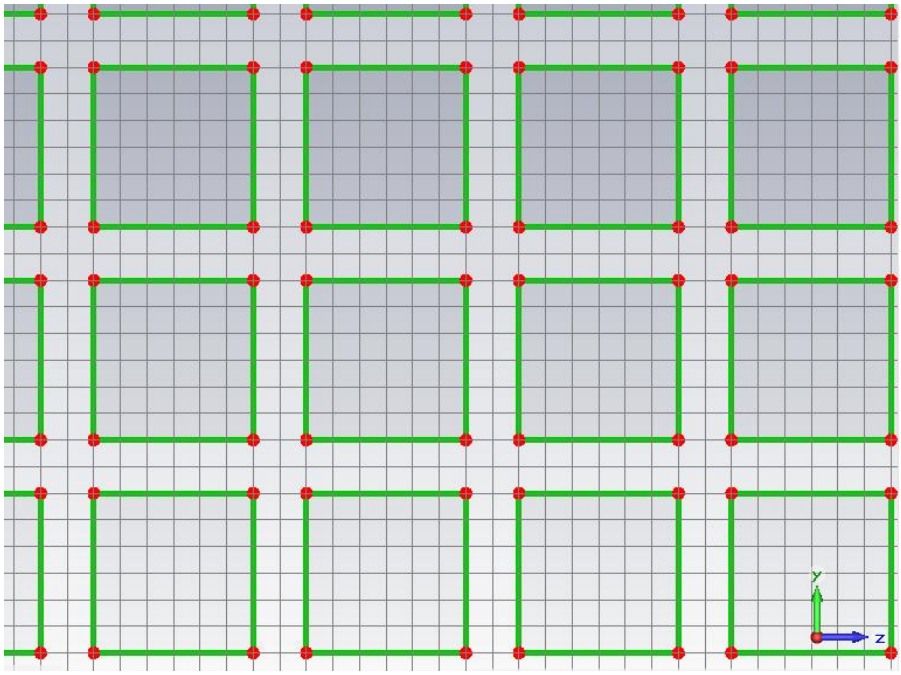

Figure 4.10. Cross-section of aperture meshing in an enclosure model.

same mesh density as the UPW would be desirable, but would also the total number of cells to increase beyond 100 million, which would lead to very long simulation times for each model. Figure 4.11 shows the meshing of the apertures from the side. Here, it can be seen that inside the enclosure, each mesh cell is 0.5mm x 0.5mm x 0.5mm, while the cells outside of the enclosure are automatically chose by the solver.

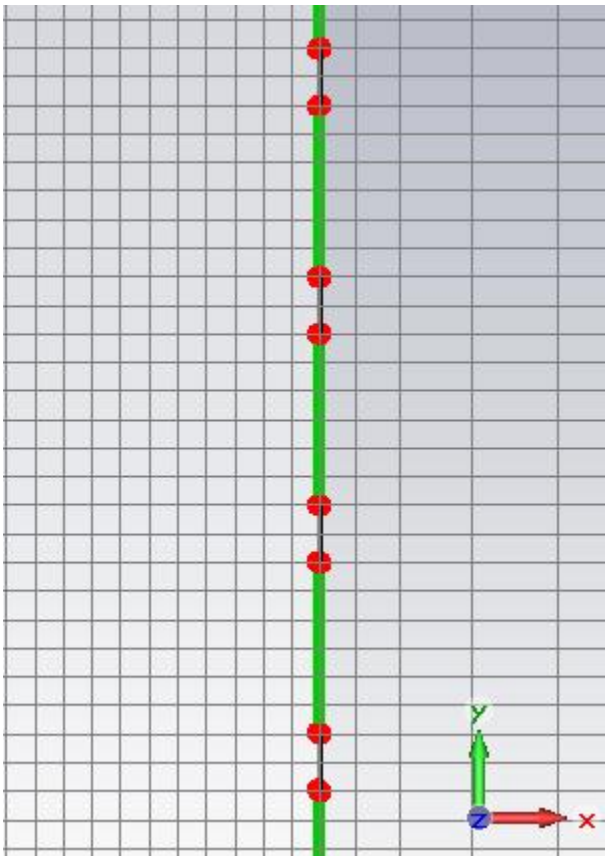

Figure 4.11. Side-view of the aperture meshing for the enclosure models.

4.4 RESULTS FOR ALL ENCLOSURE SIMULATIONS

Back in Section 3.3, the complete results for a single model were analyzed in order to show the reader the steps that were taken to ensure that reasonable data was obtained. As the criteria are the same for ensuring valid data with the enclosure models and the UPW models, there is no need to repeat the same steps. Over the band of 1GHz to 20GHz, the ratio of |E|/|H| was again examined and found to be approximately 120π, and the time-of-arrival for signals at the monitor points was checked and matched well with the theoretical expectations.

4.4.1 Results for Small Arrays. Figure 4.12 shows the results for an array with

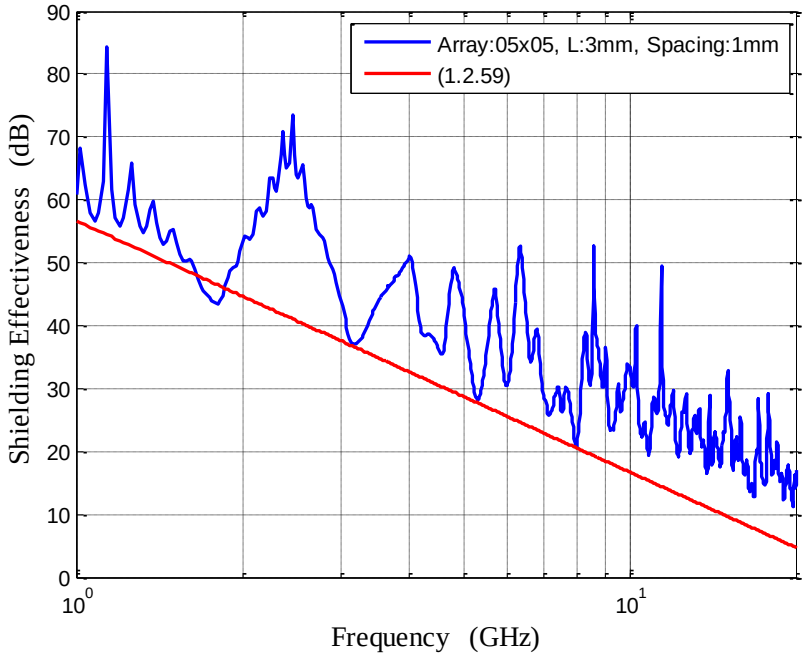

Figure 4.12. Simulation SE result and (1.2.59) for an enclosure model here N = 25, L = 3mm, aperture spacing = 1mm, and a dielectric of σ = 0.01S.

25 apertures (arranged 5x5), L = 3mm, aperture spacing of 1mm, and backed by an over-moded cavity loaded with a lossy dielectric of σ = 0.01S. As noted earlier in (4.7), the SE result has dips at specific frequencies that correspond to the resonant frequencies of the cavity where the intensity of the radiated fields are strongest. Due to the alignment and location of the excitation dipole with the y-axis in the middle of the enclosure, as shown in Figure 4.13, the only modes excited within the enclosure are TE_{m0p}, and m and p must

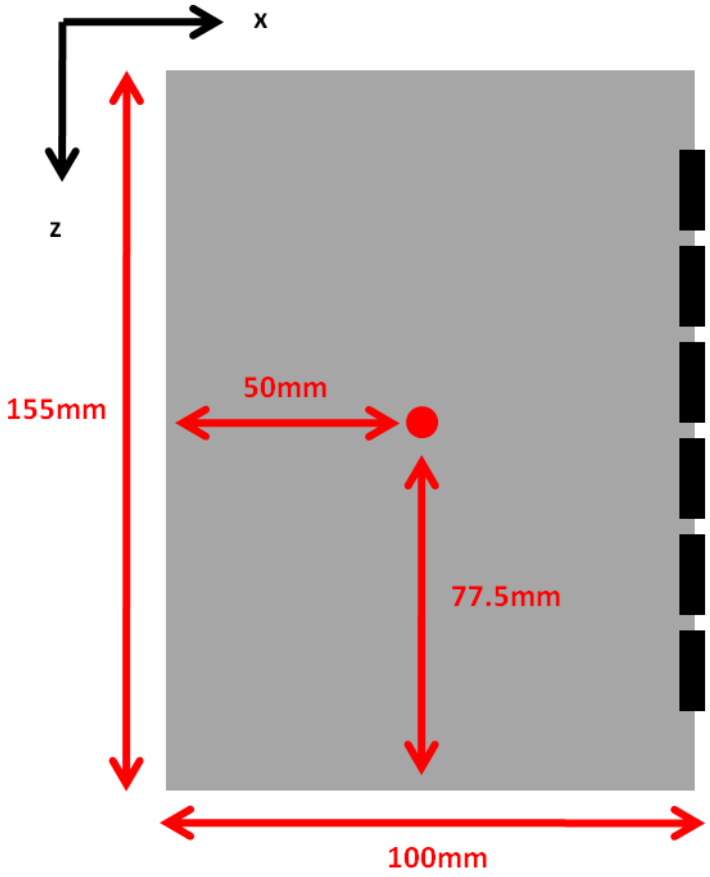

Figure 4.13. Location of the excitation dipole within the enclosure.

be odd integers, as the source lies at a null for all even integers of m and p. Table 4.3 provides a list of resonant frequencies, up to 10GHz and m,n,p ≤ 9, that meet the criteria mentioned. By examining Figure 4.12, one can see that the four most significant dips in SE occur at 1.78GHz (TE_{101}), 3.27GHz (TE_{103}), 5.36GHz (TE_{303}), and 8.04GHz (TE_{503}), all coinciding with the predictions shown in Table 4.3. Other modes listed in Table 4.3 can also be found in Figure 4.12, but with a less severe SE dip.

The results for the 5x5, 9x9, 13x13, 17x17, and 21x21 arrays with L = 3mm, aperture spacing of 1mm, and dielectric of $\sigma = 0.01$ are all shown together in Figure 4.14, where the results are plotted as the difference between the simulation result and (2.59).

Table 4.3. Possible Resonant Frequencies Supported by the Enclosure and Source Geometries.

Freq (GHz)	**m**	**n**	**p**
1.7851	1	0	1
2.4487	1	0	2
3.2678	1	0	3
4.6029	3	0	1
5.0659	1	0	5
5.3553	3	0	3
6.6078	3	0	5
6.9383	1	0	7
7.5622	5	0	1
8.0423	5	0	3
8.1326	3	0	7
8.8379	1	0	9
8.9254	5	0	5
9.8035	3	0	9

The ripples in the result below 3GHz are likely caused by a less than desirable energy decay in the system (about 40dB), and would be remedied by allowing the simulations to run longer. Though the resonant frequency for the TE_{101} mode is accurate, the author does not place a high degree of confidence in the SE level at this frequency shown in Figure 4.12, and SE difference in Figure 4.14 and Table 4.4.

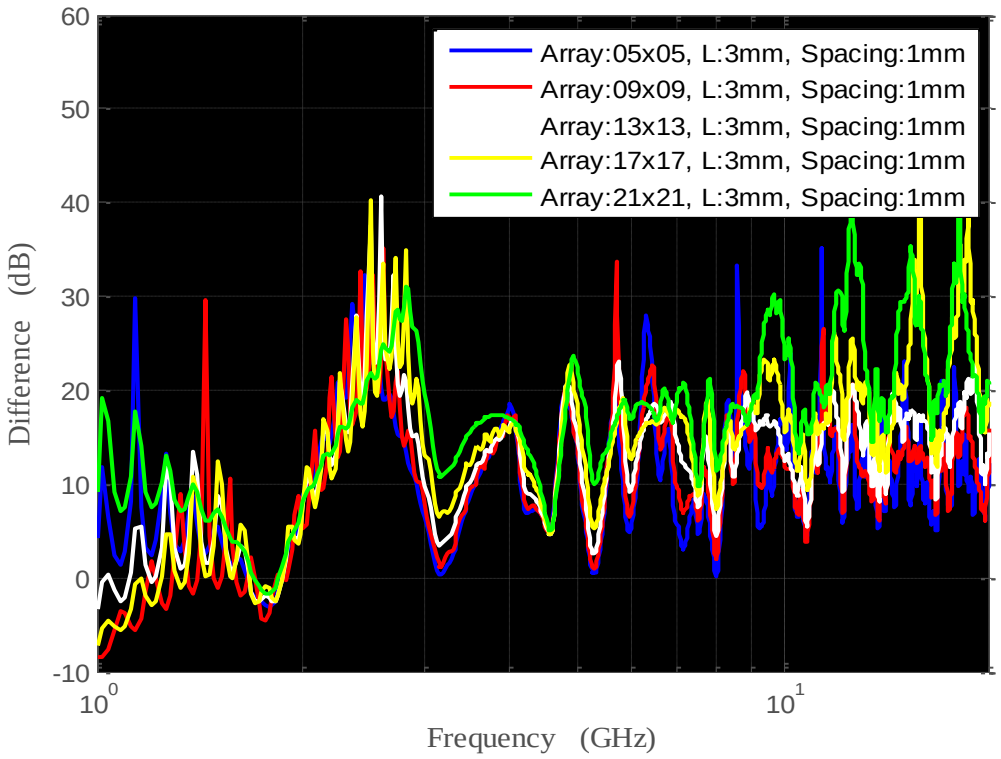

Figure 4.14. Simulation SE results and (2.59) for enclosure models where N = 25, 81, 169, 289, 441, L = 3mm, aperture spacing = 1mm, and a dielectric of $\sigma = 0.01$S.

Table 4.4. Results from Significant Frequencies in Figure 4.14.

		Frequency (GHz)							
		1.78	**3.2**	**4.56**	**5.3**	**7.56**	**7.98**	**10.5**	**10.8**
		TE_{101}	**TE_{103}**	**TE_{301}**	**TE_{303}**	**TE_{501}**	**TE_{503}**	**TE_{701}**	**TE_{703}**
Array Size	**05x05**	-3.1dB	0.3dB	5.1dB	0.5dB	4.6dB	0.1dB	6.4dB	4.1dB
	09x09	-3.8dB	1.6dB	4.7dB	1.0dB	6.1dB	2.0dB	6.8dB	3.7dB
	13x13	-2.1dB	3.6dB	4.6dB	2.5dB	7.5dB	4.3dB	8.7dB	5.5dB
	17x17	-1.2dB	6.5dB	4.7dB	5.2dB	8.8dB	7.4dB	11.3dB	9.4dB
	21x21	-1.7dB	10.78dB	5.1dB	10.0dB	9.7dB	11.3dB	13.3dB	15.3dB

In general, the results in Figure 4.14 and Table 4.4 show that for smaller arrays, the simulation results match well with the approximation from (2.59), predicting the worst-case SE within less than 1dB. As the arrays become larger and occupy more space on the enclosure wall, the apertures begin to undergo a higher degree of non-uniform illumination, and when $p \geq 3$, some apertures are excited 180^o out of phase, causing the error between simulation results and (2.59) to increase. Mathematically, this can be explained by looking back at (2.37b), which defines the tangential H-field to be

$$H_z = \frac{1}{\mu}\frac{\partial A_z}{\partial x} = \frac{k_x}{\mu} B_{mnp} \cos(k_x x)\cos(k_y y)\sin(k_z z)$$

Knowing that $k_y = 0$ from the source geometry, and that the apertures are located on the enclosure wall at x = 0, the tangential H-field reduces to

$$H_z = \frac{k_x}{\mu} B_{mnp} \sin(k_z z) = \frac{k_x}{\mu} B_{mnp} \sin\left(\frac{p\pi z}{d}\right) \tag{4.9}$$

The result in (4.9) shows that the distribution of the tangential H-field over the aperture array varies spatially by a sinusoidal function. This means that unless the apertures are

tightly grouped, the apertures will not be illuminated with uniform amplitude or phase, leading to increased error between simulation results and (2.59). However, as (2.59) is a worst-case prediction, the assumption of uniform illumination over each aperture only leads to an under-estimation of SE.

Figure 4.15 shows the difference between simulation results and (2.59) for the same aperture arrays of N = 25, 81, 169, 289, and 441, L = 3mm, aperture spacing of

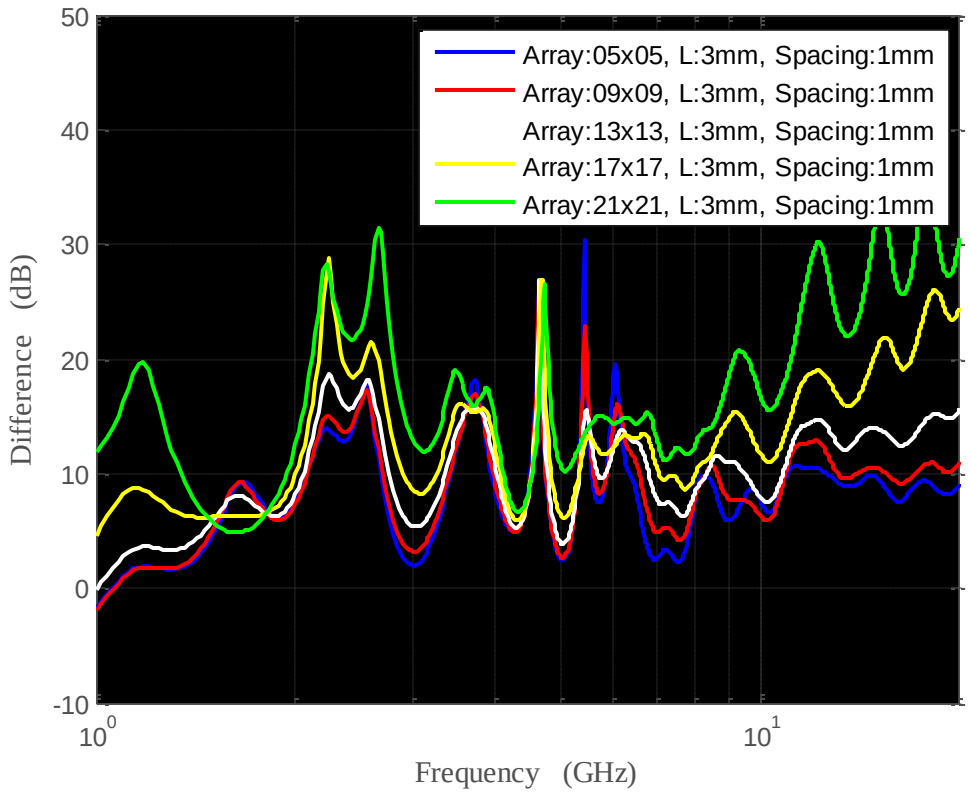

Figure 4.15. Simulation SE results and (2.59) for enclosure models where N = 25, 81, 169, 289, 441, L = 3mm, aperture spacing = 1mm, and a first-order Debye dielectric.

1mm, but this time the enclosure is loaded with the first-order Debye material. Quick examination of Figure 4.6 shows the reader that the Debye material has a relative permittivity of approximately 1.1 at low frequencies, then gradually reducing to 1 at 20GHz, which suggests that the resonant frequencies should all shift lower in the spectrum than the simulations with the simple dielectric of constant conductivity. Close comparison of Figures 4.14 and 4.15 will show that the resonant frequencies do indeed shift lower in frequency for the Debye models.

Table 4.5 shows the error between the simulation results and (2.59) for the Debye models, and good agreement is again achieved between the simulations and theory, where the approximation has predicted the SE to within 2dB for the 5x5 case. For the same reasons as the constant conductivity models, the error between the simulations and (2.59) increases as the array size increases.

As the Q of these enclosures with the Debye material approaches 10 at 20GHz, individual resonant frequencies higher in the spectrum become more difficult to identify. Alternatively, Q can be defined as

$$Q = \frac{f_{res}}{BW_{3dB}} \tag{4.10}$$

where BW_{3dB} is the 3dB bandwidth (BW) of the enclosure about a particular resonant frequency, f_{res}. When the BW of a particular mode is large enough that the BW of neighboring modes overlap, then when, for example, a 20GHz signal excites the cavity and should ideally create a $TE_{13,0,5}$ mode, the neighboring modes of $TE_{5,0,19}$ and $TE_{13,0,7}$ are spawned and cause interference with the $TE_{13,0,5}$ mode, depicted in Figure 4.16. This interference and blurring of modes is what causes the dips in SE from Figure 4.15 to

Table 4.5. Results from Significant Frequencies in Figure 4.15.

		Frequency (GHz)						
		1.78	**3.2**	**4.56**	**5.3**	**7.56**	**7.98**	**10.5**
		TE_{101}	**TE_{103}**	**TE_{301}**	**TE_{303}**	**TE_{501}**	**TE_{503}**	**TE_{701}**
Array Size	**05x05**	6.3dB	2.0dB	5.1dB	2.5dB	2.5dB	2.4dB	6.6dB
	09x09	6.0dB	3.2dB	5.0dB	2.7dB	5.0dB	4.2dB	6.0dB
	13x13	6.3dB	5.4dB	5.3dB	3.9dB	7.5dB	6.3dB	7.7dB
	17x17	6.3dB	8.3dB	5.9dB	6.2dB	9.7dB	8.6dB	11.0dB
	21x21	4.9dB	11.9	6.7dB	10.2dB	11.4dB	11.7dB	15.6dB

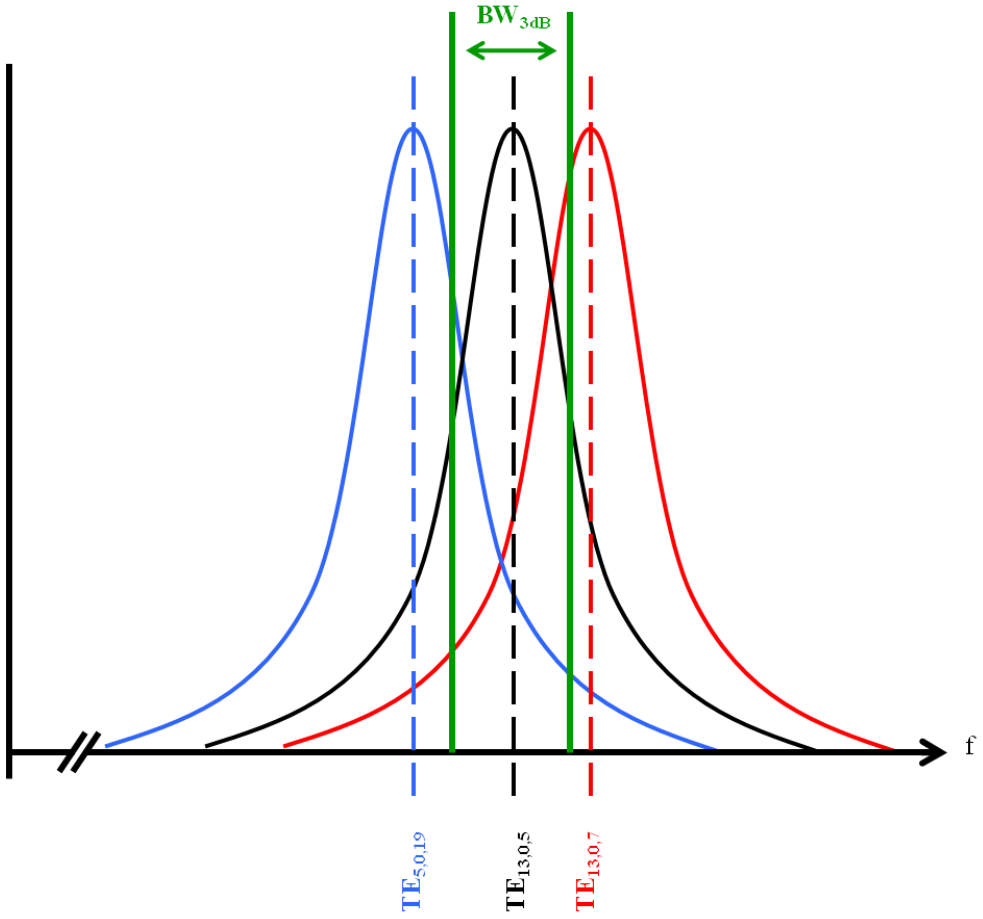

Figure 4.16. Graphical depiction of "mode blurring" at high frequencies for a low-Q cavity.

vanish at higher frequencies when compared to the results in Figure 4.14 for a Q of approximately 110 at 20GHz. Consequently, the "mode blurring" appears to aid in improving the SE of these simulations.

4.4.2 Results for Offset Array. To examine the impact of array location in the enclosure wall, an additional model was created to compare with the 5x5 Array of 3mm apertures. This additional model consisted of the same arrangement of 25 3mm apertures in a 5x5 array with 1mm spacing between apertures, but instead of placing the array in the center of the enclosure wall, the array was placed in a corner of the wall. Both models used the first-order Debye dielectric. The results of the two simulations are shown in Figure 4.17 as the difference between the simulation SE and (2.59).

Figure 4.17 is interesting in that it shows that when the aperture array is not placed near the center of the enclosure wall, the radiated field intensity decreases, owning to the increase in error between the worst-case approximation by (2.59) and the simulation results. Looking again at (4.9), which states that the spatial distribution of the tangential H-field over the wall of the aperture array is sinusoidal, one can see that when $z = d/2$, coinciding with the array being positioned in the center of the wall, the sine function is maximum. On the contrary, when the array is close to one of the walls in the z-direction, where $z \approx 0, d$, the sine function is minimal.

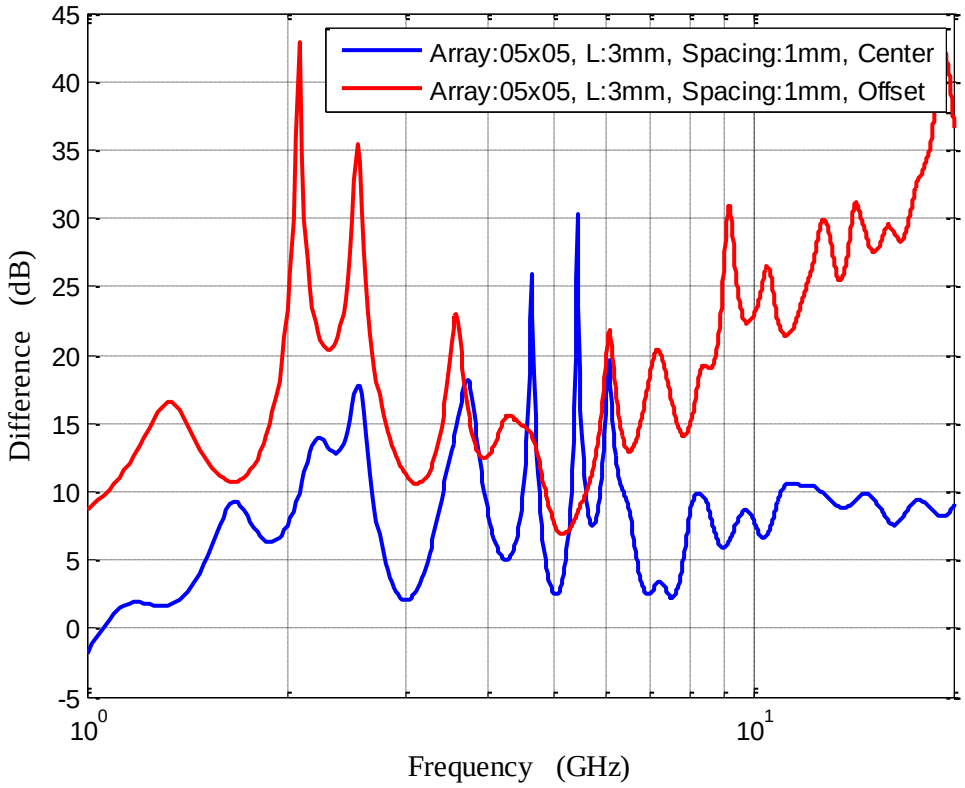

Figure 4.17. Simulation SE results and (2.59) for enclosure models where N = 25, L = 3mm, aperture spacing = 1mm, and a first-order Debye dielectric for the array centered and offset in the enclosure wall.

The closest that the result from the offset array simulation comes to (2.59) occurs at 5.1GHz, which is the TE_{105} mode. Looking at the z-coordinate for the centroid of the array, which is -58mm, or approximately d/10 from the corner of the enclosure at z = -77.5mm, one can see that at when the TE_{105} mode is excited, the offset array falls almost in line with a maximum point from (4.9). This result shows that no matter where the array is positioned, maximum radiated field intensity can potentially occur if the array falls on a maximum point of the sinusoidal field distribution by (4.9). While this scenario

tends to happen more often for an array placed in the center of the enclosure wall, an array can still be maximally excited anywhere on the enclosure wall, just less likely when the array is offset from the exact center.

4.4.3 Results for Large Arrays. The small array simulations were useful in understanding the physics of the enclosure simulations, but may provide misleading or incomplete results for when an enclosure has many hundreds of apertures, perhaps even consuming an entire wall. For this reason, three models were designed and simulated for the scenario when an entire wall of the enclosure is filled with as many apertures as possible for L = 3mm, 6mm, and 9mm. Loaded with the simple dielectric of $\sigma = 0.01S$ and an aperture spacing of 1mm, the result for the 37x27, 3mm array is shown in Figure 4.18, with the results for all three models shown in Figure 4.19, and numbers for the significant frequencies given in Table 4.6.

Figure 4.18 clearly shows that when an entire wall of an enclosure is filled with apertures, the only modes that cause significant amounts of radiation are TE_{m01} modes, which is expected, as these are the only modes where every aperture is illuminated with the same phase. Where the simulation results in 4.18 differ from the expectation by (2.59) is in the slope of SE. In all previous simulations where the dielectric conductivity was $\sigma = 0.01S$, the SE decreased at a rate of -40dB/dec, which agrees with (2.59). However, Figure 4.18 clearly shows that the simulation results decrease by -20dB/dec, which is also seen in Figure 4.19 for the other two simulations. The exact reason for this difference in slope is not yet understood, but a possible cause may be that the power radiated by that

many apertures simply violates the assumption that $P_r << P_d$. This would mean that the cavity Q would have to be determined by

$$Q = \left(\frac{1}{Q_d} + \frac{1}{Q_r} \right)^{-1}$$

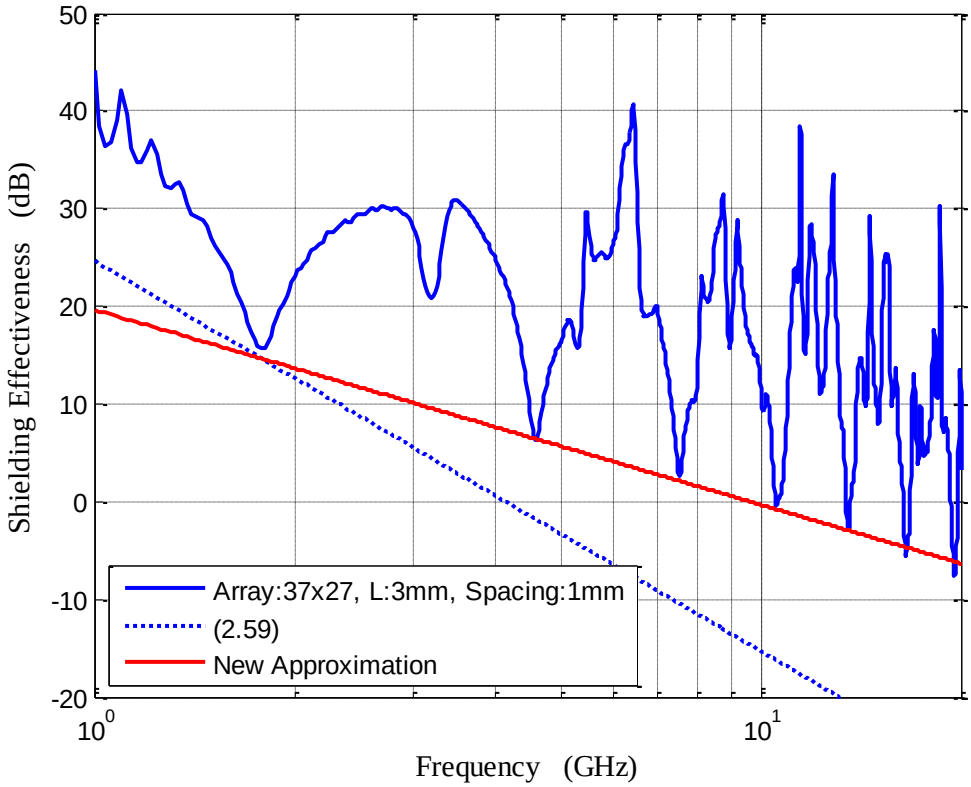

Figure 4.18. Simulation SE results, (2.59), and an experimentally found approximation for an enclosure model where N = 25, L = 3mm, aperture spacing = 1mm, and a dielectric of $\sigma = 0.01$S.

The new assumption, plotted along with the simulation results and (2.59), was found experimentally. By noticing that the simulation results sloped by -20dB/dec, the frequency dependence of (2.59) was changed from $f^{3/2}$ to $f^{1/2}$, and the offset was adjusted to fit the data. Ultimately, this manual fitting of the new approximation led to

$$SE_{dB,Enc,New} = 55 - 20\log_{10}\left(Nf^{1/2}L^3\right) + 10\log_{10}\left(\frac{V}{Q}\right) - MC_{dB} \tag{4.11}$$

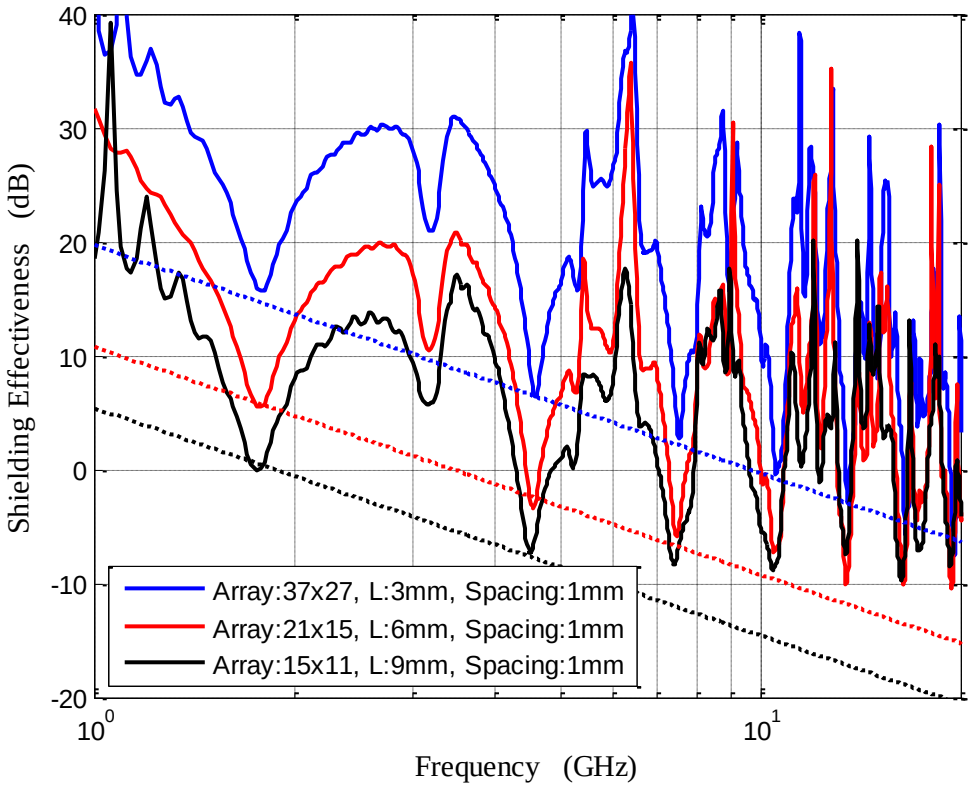

Figure 4.19. Simulation SE results and (1.2.59) for enclosure models where N = 999, 231, 165, L = 3mm, 6mm, 9mm, aperture spacing = 1mm, and a dielectric of constant conductivity σ = 0.01S. The new approximation is shown as the perforated curves.

where by the accurate predictions of SE seen in Figure 4.19 and shown in Table 4.6, the reader can see that (4.11) still varies accordingly by N and L^3. The data in Table 4.6 also supports the claim from Section 3 that the approximations are only reliable to the point where the aperture dimension, L, reaches $\lambda/6$. Beyond 5.6GHz, the error for the 9mm apertures quickly increases beyond 3dB, and similarly for the 6mm apertures beyond 8.3GHz. Beyond 16.7GHz, the error for the 3mm apertures is seen to start increasing, but sufficient data points that high in frequency are not available.

Table 4.6. Results from Significant Frequencies in Figure 4.16.

		Frequency (GHz)						
		1.78	**4.56**	**7.56**	**10.5**	**13.4**	**16.4**	**19.5**
		TE_{101}	**TE_{301}**	**TE_{501}**	**TE_{701}**	**TE_{901}**	**$TE_{11,0,1}$**	**$TE_{13,0,1}$**
Array Size	**37x27, L:3mm**	1.0dB	-0.1dB	0.5dB	0.4dB	0.1dB	-1dB	-1.6dB
	21x15, L:6mm	-0.3dB	-0.9dB	0.9dB	2.4dB	1.8dB	3.4dB	4.5dB
	15x11, L:9mm	-0.6dB	0.5dB	3.6dB	6.1dB	9.6dB	9.1dB	11.7dB

One model with the first-order Debye dielectric was also run for an array with 999 apertures (37x27), L = 3mm, and aperture spacing of 1mm. The result for this simulation is shown in Figure 4.20, along with the approximation from (2.59) and the new approximation from (4.11). Again, the new approximation from (4.11) is shown to work much better with the model where apertures fill an entire wall, with the smallest error

being 2.4dB at 4.4GHz for the TE_{301} mode. These results agree well with the constant σ dielectric models.

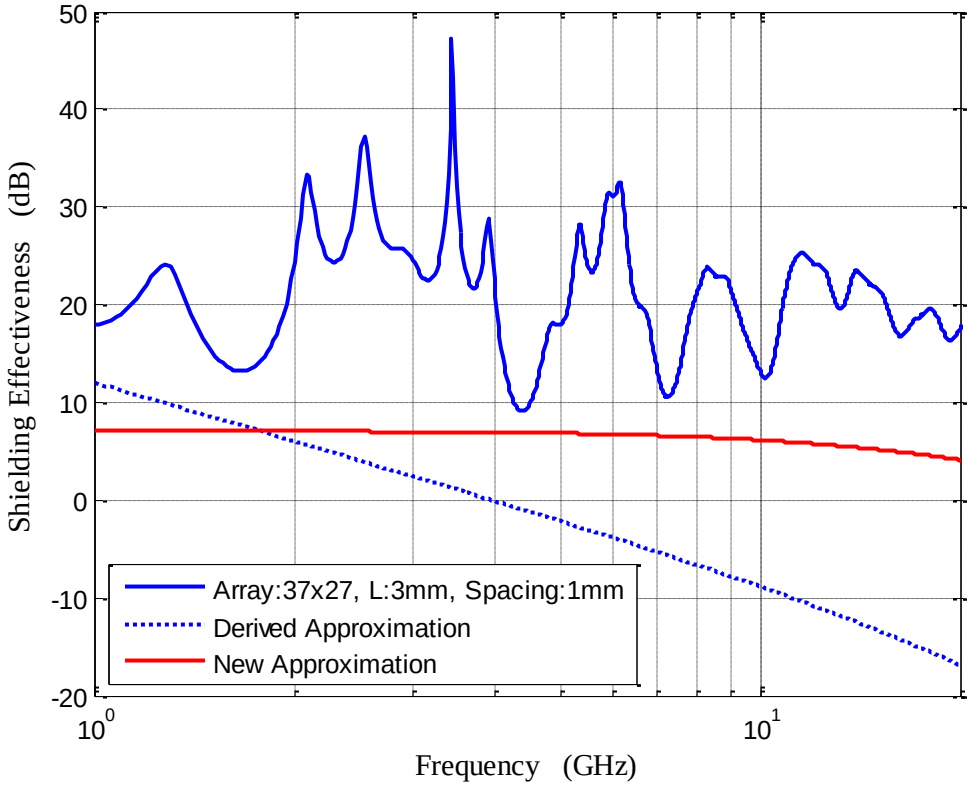

Figure 4.20. Simulation SE result and (1.2.59) for enclosure model where N = 999, L = 3mm, aperture spacing = 1mm, and a first-order Debye dielectric. The new approximation is shown as the perforated curve.

4.4.4 Summary of Enclosure Results. In this section, the results from the enclosure simulations have shown that when small aperture arrays are excited by an over-moded cavity, the worst-case SE can be predicted to within less than 1dB using the

derived prediction of (2.59). Varying the dielectric material loading the enclosure from $\sigma = 0.01S$ to a first-order Debye material, where $\tan\delta = 0.1$ at 20GHz, had little impact on the results, adding confidence to (2.59). As the number of apertures increased from 25 to 441, the error between the SE results and (2.59) increased due to a higher degree of non-uniform illumination, but SE could still be pessimistically predicted to within about 5dB.

Simulations with the small arrays also showed that the location of the aperture array in the enclosure wall affects the radiation intensity. For the particular source geometry used in these simulations, arrays placed in the center of an enclosure wall led to significantly higher levels of radiation intensity over the studied frequency range when compared to an array placed in the corner of a wall. While this was true, (2.59) still serves as a worst-case SE prediction, and pessimistically predicts the SE for an array located at any point on the enclosure wall.

When the array sizes increased to the point of filling an entire wall of the enclosure, (2.59) no longer accurately predicted SE over the band of 1GHz to 20GHz, as the slope of these curves changed by a factor of 20dB. However, through manual manipulation, the new approximation in (4.11) was found, and was able to predict the SE of these large arrays to within 1dB while the aperture dimension, L, was less than $\lambda/6$. While the exact cause of the shift in frequency dependence is not yet known, (4.11) still agreed with the results from Section 3, which stated that SE is a function of N and L^3 as long as L is less than $\lambda/6$.

Despite having data that works well for the two distinct cases of small aperture arrays and arrays that consume an entire enclosure wall, it would be very valuable to find the cause of this difference in frequency dependence. Along with discovering the cause, it

would be even more beneficial to practicing engineers if (2.59) and (4.11) could be combined to predict the point where the frequency dependence changes, ultimately leading to a generic SE prediction.

5 CONCLUSIONS AND FUTURE WORK

The purpose of this thesis was to revisit the work performed by a previous EMC lab student, Min Li (PhD '99), on predicting the worst-case shielding effectiveness (SE) of metallic enclosures with aperture arrays. Section 2 began by discussing Bethe's theory on diffraction by small holes [5], which presented a means of representing each electrically small aperture with equivalent electric and magnetic polarization currents. From here, a generic equation was found for the radiated far electric field intensity at 3m normal to an aperture, which was extended to include the increased field intensity by multiple apertures and the mutual coupling between these apertures. The excitation of these apertures was then solved for an aperture array backed by an over-moded cavity, along with the simpler scenario of an array in an infinite PEC sheet excited by a uniform plane wave (UPW) at normal incidence.

Section 3 focused on the UPW simulations, which were first conducted so that the author could gain a sound understanding of the physics for these simple simulations before moving on to the more complex enclosure simulations. The goal of these simulations was to study the UPW approximation of (2.58), given as

$$SE_{dB,UPW} = 338 - 20\log_{10}\left(Nf^2L^3\right) - MC_{dB} \tag{2.58}$$

In this approximation, the dependent variables include the number of apertures, N, the size of each aperture, L, the frequency dependence, f, and the mutual coupling between apertures, MC. After many simulations, it was found that this worst-case SE prediction for UPW illumination of an aperture array in an infinite PEC sheet at normal incidence was valid to within 3dB while L is less than $\lambda/6$.

Section 4 progressed to simulations where the aperture arrays were excited by an over-moded cavity. From Section 2, the derived SE approximation of (2.59) for over-moded cavity excitation was found to be

$$SE_{dB,Enc} = 240 - 20\log_{10}\left(Nf^{3/2}L^3\right) + 10\log_{10}\left(\frac{V}{Q}\right) - MC_{dB} \tag{2.59}$$

where the additional dependent variables are the enclosure volume, V, and the quality factor of the enclosure, Q. For small aperture arrays, (2.59) was found to be accurate to within 1dB, with the error between the simulation results and (2.59) increasing as the array size increased, and when the arrays were moved closer to the walls. However, this increased error between simulations and (2.59) is due to the worst-case nature of the approximation, as (2.59) is intended to under-estimate SE, or at least predict SE very closely when the apertures are uniformly excited.

When the simulations in Section 4 were extended to test aperture arrays that fill an entire wall of the enclosure, it was found that (2.59) no longer provided a sufficient estimate of SE. Instead, through manual curve-fitting, a new approximation was found for the models with very large arrays, and was found to be

$$SE_{dB,Enc,New} = 55 - 20\log_{10}\left(Nf^{1/2}L^3\right) + 10\log_{10}\left(\frac{V}{Q}\right) - MC_{dB} \tag{4.11}$$

where the only differences between (4.11) and (2.59) are the offset and frequency dependence. Simulations for these large aperture arrays yielded results that were within 1dB of (4.11), provided that L is less than $\lambda/6$.

Ultimately, it was found that the approximations of (2.58), (2.59), and (4.11) can all predict the worst-case SE from aperture arrays of square elements to within 3dB,

while L remains less than $\lambda/6$. Further restrictions apply, including the observation point being restricted to a location 3m normal to the center of the aperture array (UPW models), or 3m normal to the center of the enclosure wall containing the aperture array (enclosure simulations).

While the results presented in this thesis are acceptable and useful, there is indeed room for additional exploration of the topic. Though the UPW simulations are not particularly useful for practical problems, the effect of exciting the apertures with a UPW at non-normal incidence, and examining the scattered fields at different angles could lead to a better understanding of the scattered fields at locations that are not normal to the over-moded enclosures. Also, as mentioned at the end of Section 4, it would be very useful to derive the result in (4.11), followed by combining (4.11) with (2.59) in order to create a more generic SE prediction that is useful for enclosures with aperture arrays of a variety of sizes.

REFERENCES

[1] M. Li, S. Radu, J. Nuebel, J. L. Drewniak, T. H. Hubing, T. P. VanDoren, "Design of Airflow Aperture Arrays in Shielding Enclosures," in *IEEE International Symposium on Electromagnetic Compatibility*, 1998, pp. 1059-1063.

[2] M. Li, J. L. Drewniak, T. H. Hubing, R. E. DuBroff, T. P. VanDoren, "Slot and Aperture Coupling for Airflow Aperture Arrays in Shielding Enclosure Designs," in *IEEE International Symposium on Electromagnetic Compatibility*, 1999, pp. 35-39.

[3] M. Li, J. Nuebel, J. L. Drewniak, R. E. DuBroff, T. H. Hubing, T. P. VanDoren, "EMI from Airflow Aperture Arrays in Shielding Enclosures-Experiments, FDTD, and MoM Modeling," *IEEE Trans. Electromagn. Compat.*, vol. 42, no. 3, pp. 265-275, Aug. 2000.

[4] M. Li, J. L. Drewniak, S. Radu, J. Nuebel, T. H. Hubing, R. E. DuBroff, T. P. VanDoren, "An EMI Estimate for Shielding-Enclosure Evaluation," *IEEE Trans. Electromagn. Compat.*, vol. 43, no. 3, pp. 295-304, Aug. 2001

[5] H. A. Bethe, "Theory of Diffraction by Small Holes," *The Physical Review*, vol. 66, nos. 7 and 8, pp 163-182, Oct. 1944.

[6] S. Cohn, "Determination of Aperture Parameters by Electrolytic-Tank Measurements," *Proceedings of the IRE*, vol. 39, no. 11, pp. 1416-1421, November 1951.

[7] N. A. McDonald, "Simple Approximations for the Longitudinal Magnetic Polarizabilities of Some Small Apertures," *IEEE Trans. Microwave Theory and Techniques*, vol.36, no.7, pp.1141-1144, Jul 1988.

[8] Pozar, D. M. *Microwave Engineering*. New York, NY: Wiley, 1998. Print.

[9] Balanis, Constantine A. *Antenna Theory*. Hoboken, NJ: J. Wiley-Interscience, 2005. Print.

[10] Taflove, A. *Computational Electrodynamics.* Norwood, MA: Artech House, Inc., 2000. Print.

VITA

Nicholas Bennett Mentesana was born in Lee's Summit, MO. In December of 2008, he received his B.S. in Electrical Engineering from the Missouri University of Science and Technology in Rolla, MO, graduating with a perfect 4.0 grade point average. He worked summer internships at Burns and McDonnell in 2007, at Garmin Intl. in 2008, and again at Garmin Intl. in 2009. Nicholas joined the Electromagnetic Compatibility Laboratory at Missouri S&T in April of 2010.

During his undergraduate career, Nicholas was a four-year member of the Missouri S&T soccer team. He was initiated into the Pi Kappa Alpha Fraternity in September of 2006.

Nicholas Bennett Mentesana has been a member of the Institute of Electrical and Electronics Engineers (IEEE) since 2010. He has been a member of Kappa Mu Epsilon since 2005. He was inducted into Eta Kappa Nu Honor Society in 2008.